PHOTONICS

CMDITR Review of Undergraduate Research

Contributions from undergraduate research experiences within the
NSF Center on Materials and Devices for Information Technology Research

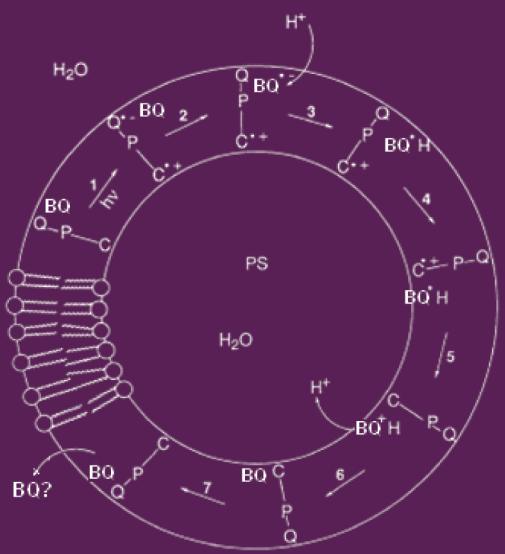

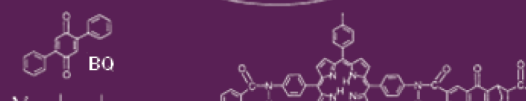

Volume 3, Number 1

This material is based upon work supported by the STC Program of the National Science Foundation No. DMR 0120967, and CHE 0453596 .

All rights reserved. No part of the Review may be reproduced in any form or by any means without written permission.

Any opinions, findings and conclusions or recommendations expressed in this material are those of the authors and do not necessarily reflect the views of the National Science Foundation.

Printed in the United States at the University of Washington, Seattle, WA

Inquires should be addressed to:

Center on Materials and Devices for Information Technology Research
Educational Partnership Programs
University of Washington
Department of Chemistry
Box 351700
Seattle, WA 98195-1700

ehrdo@u.washington.edu
http://stc-mditr.org

Volume 3, Number 1

Welcome to the Second Edition of CMDITR Review of Undergraduate Research

This volume of the Reviews features extended abstracts of students who participated in the National Science foundation (NSF) Center on Materials and Devices in Information Technology and Research (CMDITR) Summer 2006 research Experiences for Undergraduates (REU) program.

The REU experiences often act as a launching point or catalyst for entry by undergraduates into technical fields of study. The REU experience is symbiotic in nature as it supports not only the undergraduate participant who experiences research first-hand prior to committing to graduate study, but also the students mentors, be they faculty members, research scientists, post-doctoral fellows, or graduate students. While working with REU students graduate students and post-doctoral fellows learn teaching and mentoring skills needed to manage labs they will be responsible for in the future. Faculty members and other researchers, who share their expertise with these enthusiastic learners, also benefit as they reflect on the excitement upon which their careers have been built.

The CMDITR REU Summer Program placed undergraduate students from across the United States in CMDITR state-of-the-art research labs at the University of Washington, University of Arizona and Georgia Institute of Technology. The undergraduates worked on interdisciplinary research contributing to advancements in information technology with researchers in the fields of chemistry, physics, optics, materials science and engineering. The REU Program emphasized the teamwork nature of scientific research and was supplemented by a collection of activities including ethics training and workshops in scientific communication.

The role of the Review is to offer a forum for participants involved in the CMDITR REU to share their research with their REU peers, future REU students, CMDITR graduate students and faculty members, and others interested in the work of CMDITR. The Review is also a forum that depicts the breadth and depth of CMDITR research.

To learn more about the CMDITR REU program and opportunities please visit http://stc-mditr.org/REU .

A special thanks to all the REU participants for their work, their mentors for their time and patience, and the REU program coordinators (Maggie Harden, Olanda Bryant, and Kristin Wustholz) for their efforts to make the program successful.

The extended abstracts included in the Review are presented in alphabetical order by the participant's last name.

P. J. Reid, January 16, 2007

TABLE OF CONTENTS

Study of the Binding of Ethidium Bromide to CTAB-DNA in Solution and on Thin Films

Olesya A. Benson, Edmonds Community College

David P. Rangel, Bruce H. Robinson, University of Washington, Department of Chemistry

Introduction

The development and use of organic nonlinear optical (ONLO) chromophores has the potential to revolutionize the field of information and computing technology. ONLO chromophores are optically-active molecules designed to have specific absorption and reemission properties. However, in order to be functional in devices they have to be oriented. The orientation of chromophores is accomplished by applying an external poling field. Polymers assist in alignment and positioning of chromophores thereby maximizing their desirable nonlinear effects.

In previous research of Grote's group, a marine-based DNA biopolymer, purified from salmon roe and milt sacs, a waste product of the Japanese fishing industry, has demonstrated properties as an organizing agent and waveguide for chromophores. It has been shown that DNA can transport electrical current as efficiently as a good semiconductor. DNA appears to be a stable material at high temperatures with no visible degradation of films up to 200°C.[1] Also, many fluorescent dyes are known to intercalate into DNA, which serve as supporting material for the different chromophores. Therefore, electro-optical properties of chromophores aligned in DNA can provide an alternative strategy for ordering ONLO chromophores and can be used in many photonic applications.

The purpose of the design project is to study the optical properties of surfactant-modified DNA solutions and thin films doped with ethidium bromide at different molar ratios, using UV-visible spectroscopy. These thin film materials can be regarded as ONLO materials in optical modulators or interferometers.

Results and Discussion

The design experiment was divided into two parts. In the first part, the surfactant-modified DNA solutions and thin films from these solutions were studied, and in the second part, intercalation of the complex by ethidium bromide at different molar ratios on the thin films and in the solutions was investigated. The coating and intercalation strategy are shown in Figure 1.

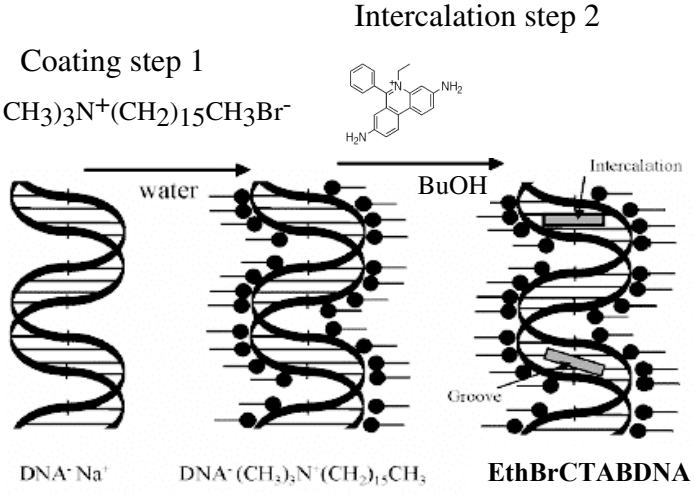

Figure 1. Coating and intercalation strategy.

DNA is soluble only in polar solvents and does not dissolve in nonpolar solvents, in which ONLO materials dissolve. Therefore, DNA was coated with lipid-surfactant cetyltrimethylam-monium bromide (CTAB)[2] to neutralize the phosphate charges on DNA, thereby making the complex nonpolar and soluble in organic solvent. Figure 2 shows that the CTABDNA complex is the product of CTAB and DNA reaction.

$$DNA^{-}Na^{+} + CH_3(CH_2)_{15}N^{+}(CH_3)_3Br^{-} \rightarrow DNA^{-}CH_3(CH_2)_{15}N^{+}(CH_3)_3 + Na^{+}Br^{-}$$

Figure 2. Reaction of DNA and CTAB.

Several tests were performed to analyze complex CTABDNA. FTIR analysis was used to compare transmittance peak heights for DNA and CTABDNA, and then CTAB and CTABDNA. The molar ratio at which DNA and CTAB reacted was determined. For each mole of DNA base pair two moles of CTAB is required, which exactly neutralizes phosphate charges of DNA and CTAB in the complex. That is why the complex becomes nonpolar and easily precipitates from water.

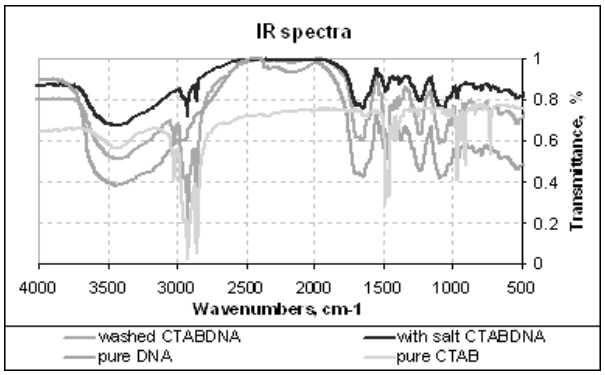

Figure 3. FTIR analysis of the complex CTABDNA.

Circular dichromism was used to measure the helicity of the CTABDNA complex in the solvent. The CTABDNA complex was dissolved in a nonpolar solvent suitable for making thin films. Butanol was the choice because it has a high boiling point and it ensures a smooth, uniform film during the spin coating process. To determine the effect of CTAB on helical structure of CTABDNA the spectra of CTABDNA were compared with the reference spectrum of B-form DNA in an aqueous environment. The modest shift in the spectrum of CTABDNA shows that the secondary structure of DNA is retained in butanol.

UV-visible spectroscopy was used to determine the solubility of the complex in BuOH. Absorption spectrum shows DNA peak at $_{max}$ = 260 nm, therefore CTABDNA was successfully dissolved in BuOH solvent. Because CTABDNA molecule is biological, it might degrade from thin film procedure and high temperature used in baking of thin film. Therefore, the spectrum of original solution from which thin films were made was used as a reference to check the stability of CTABDNA.

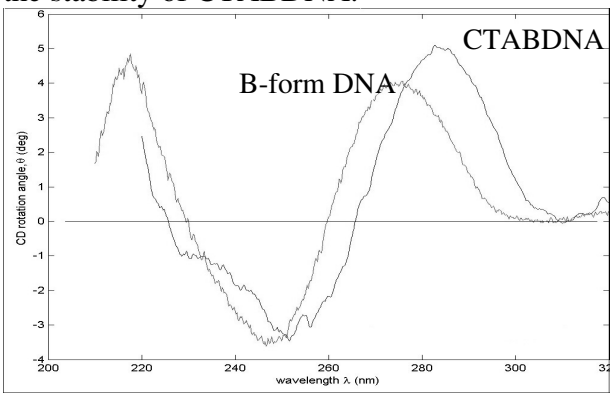

Figure 4. Comparison of CD of DNA in an aqueous environment with CD of the CTABDNA in butanol.

Solution of 1% (w/w) CTABDNA for thin films was constantly kept at 60°C for the complex to be fully dissolved. The thin films were made at different speed, to see how the thickness of the thin films changes depending on the speed. During the experiment it was determined that the absorption spectra of thin film on the glass substrate can not be measured because CTABDNA peak is beyond detection of the instrument. The thin films were redissolved and solutions of redissolved thin films were compared with the original solution CTABDNA. Since changes in the spectra of redissolved thin film solutions were not observed, the electron structure did not change. From the results, on Figure 5 the spectra of redissolved thin films repeat the shape of the original solutions, so the CTABDNA complex is stable to thin film procedure.

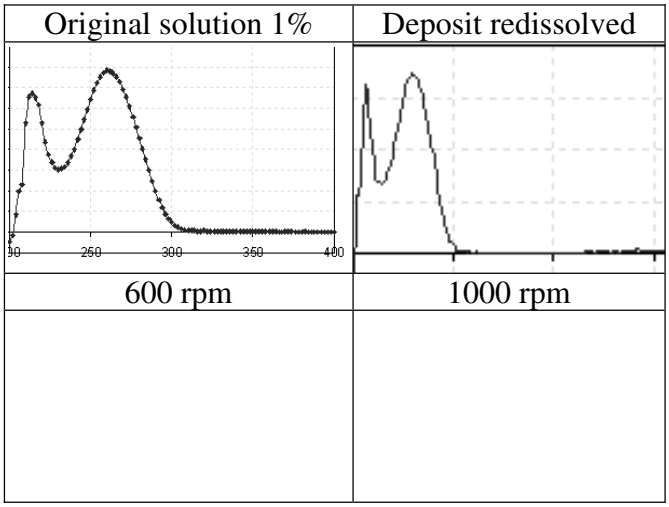

Figure 5. Absorption spectra of original CTABDNA and redissolved solutions.

When results show that CTABDNA is stable and it is possible to make thin films from the complex, the intercalation of the complex using ethidium bromide at different molar ratios was followed Figure 1, step 2. During intercalation, Figure 6, ethidium bromide pushes bases from each other molecule and molecule of ethidium bromide is inserted between adjacent two base pairs. The effect of intercalator, upon binding, is lengthening of the DNA. This happens because the DNA must unwind and allows the chromophore to fit between successive base pairs. When ethidium bromide binds to DNA, a shift in the absorption spectra of the intercalator can be detected by UV/Vis spectroscopy.[3] If DNA retains it secondary structure in the CTABDNA, then the spectra of ethidium should also shift upon binding to the complex. This assumption was used as basis for determining if the ethidium binds to the complex in butanol and on thin films.

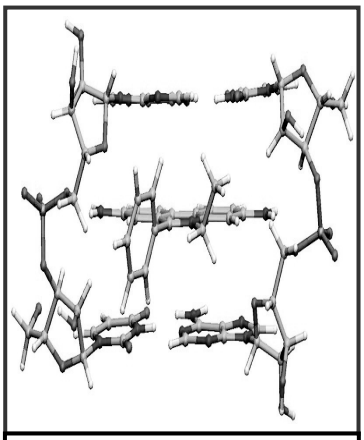

Figure 6. Intercalation of ethidium bromide in DNA.

A range of concentration of CTABDNA complex was dissolved in ethidium bromide/butanol solutions to determine the molar ratio of DNA to ethidium at which the ratio of the bound to unbound ethidium was maximized. For all molar ratios tested no significant change in the spectral line shape was observed as can be seen in Figure 7.

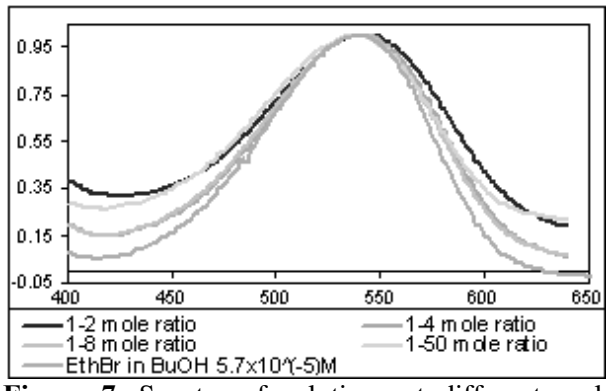

Figure 7. Spectra of solutions at different molar ratios ethidium bromide to CTABDNA complex from which thin films were made.

So, ethidium bromide did not intercalate into CTABDNA solutions. The spectrum of ethidium bromide in butanol with no CTABDNA present is co-plotted for reference.

Decision was made to analyze spectra of thin films and see whether ethidium bromide bound to the complex after the thin films were spun. It was hypothesized that spin coating would eliminate the solvent while simultaneously forcing the ethidium to intercalate**.** Shown in Figure 8 are the spectra of thin films at different molar ratios and speeds. From the absence of any spectral change, it is evident that spinning procedure failed to force ethidium into CTABDNA. The spectra of thin films of 1-2, 1-4, 1-8, 1-50 molar ratios at 600 rpm have negligible absorbance at 536 nm.

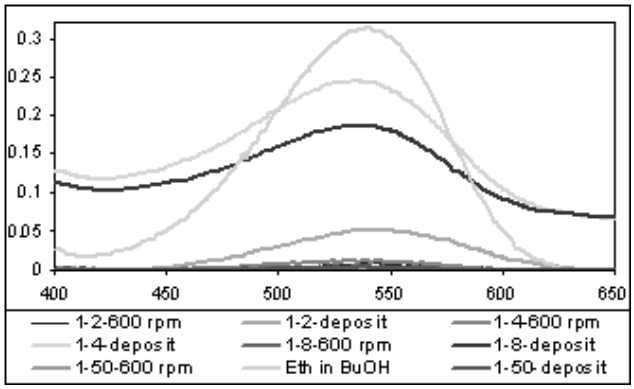

Figure 8. Spectra of thin film at different molar ratios and speeds.

As control the 1-4 molar ratio thin films were redissolved in butanol and the UV/Vis spectra was taken of the solutions. There are no observed changes in the spectra, confirming that no degradation of ethidium occurred during spin coating.

To determine if the thin film protocol changes the molar ratio of CTABDNA to ethidium, the absorption from redissolved CTABDNA and CTABDNA+Ethidium thin films was used to find the percentage CTABDNA and ethidium remaining on the substrate after spinning as compared to the amount of each when deposited and allowed to dry without spinning. Table 1 (next page) summarizes the results of the calculations for 600 and 1000 rpm.

Speed, rpm	CTABDNA thickness, μm	%CTAB DNA	Eth thickness μm	%Eth Br
deposit	1.06	100	0.11	1
600	0.0334	3.2	0.0275	25.6
1000	0.0153	3.0	0.0166	15.5

Table 1. Percent of complex CTABDNA and EthBr and thickness of the thin films at 600 rpm and 1000 rpm.

It is evident that a disproportionate amount of complex is spun off the substrate as compared to ethidium bromide. Therefore, the molar ratio of CTABDNA to ethidium bromide is decreased on the thin film. Hence, to obtain the desired molar ratio on the thin film a 300 fold excess of CTABDNA and four fold excess ethidium bromide must be present in the starting solution. (to keep 100 % of both).

The homogeneity of ethidium bromide on thin films made from the solution of 1 CTABDNA to 4 ethidium bromide molar ratio at different spin coating speeds were measured from the fluorescent images of the thin films. The results are shown in Table 2.

Molar ratio	1-2	1-4	1-8	1-8
Speed, rpm	1000	600	600	1000
Lowest count of photons	4763	18938	27302	28397
Highest count of photons	278366	149513	88412	147547
Ratio	~ 58	~ 8	~ 3	~ 5

Table 2. Fluorescence determinations of homogeneity of the thin films at different molar ratios and spinning rates. Lowest count of photons is the number of photons per unit time from dimmest pixel in the frame; whereas, highest count photons is the number of photons per unit time from brightest pixel in the frame.

These data show that ethidium bromide is spread equally on the thin film only at the 1-8 molar ratio at both 600 and 1000 rpm. Fluorescence studies of thin films with high molar ratios should be continued.

Conclusions

Results of UV/vis spectroscopy indicate that ethidium bromide did not bind to the complex CTABDNA in the BuOH solutions at different molar ratios as well as on the thin film. Future work should focus on increasing the molar ratios of CTABDNA to ethidium bromide. To examine spectra of CTABDNA thin films a quartz substrate should be used.

In the immediate future, we plan to check if ethidium bromide without the complex will bind to the substrate and what % of EthBr would stay on the substrate. Thin films procedure could be improved by making solutions for thin film with higher concentration. 1% (w/w) of CTABDNA and ethdium CTABDNA solutions was used. Concentration might be increased to 5%. Speed and time, at which thin film is made, might be varied.

References

1. Heckman E. M., Yaney P.P., Hagen J.A., Grote J. G. and Hopkins F.H. Processing techniques for DNA: a new biopolymer for photonics applications, Personal communication, 2006

2. Kawabe Y., Wang L., Horinouchi S., Ogata N.. *Adv. Mater.,* **2000**, *12*, 1281-1283

3. Pohl F.M., Jovin T. M., Baehr W., Holbrook J.J.. *Proc. Nat. Acad. Sci*., **1972**, *69*, 3805-3809

Acknowledgments

Funds for this research were provided by the Center on Materials and Devices for Information Technology Research (CMDITR), and the NSF Science and Technology Center No. DMR 0120967.

Olesya would like to thank Dr. Sara Selfe and Professor Bruce H. Robinson for providing this valuable research experience.

Carbon Nanotube Alignment in Polymer Fiber for Electro-Optic Applications

Angela Burns, Edmonds Community College

Greg Winchell, Dr. Ann Mescher, Mechanical Engineering Department University of Washington

Introduction

The objective of this study was to draw polymer fiber with an inner core small enough to align commercially available carbon nanotubes (CNTs) lengthwise along the fiber axis. The cylindrical CNTs are from 1 to 15 microns long, with a diameter in the range of a few nanometers to tens of nanometers (see Figure 1).

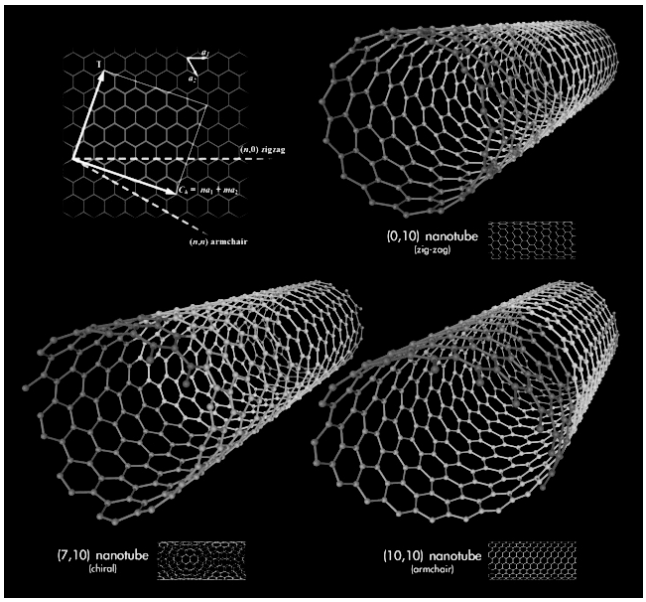

Figure 1. CNTs - Image Created by Michael Ströck on February 1, 2006. Released under the GFDL

Using a two-stage fiber draw process developed in the University of Washington Polymer Optics and Processing Lab, CNTs were incorporated into the core of an acrylic fiber, and then drawn such that the final diameter of the fiber's inner core was approximately one micron. Figure 2 illustrates possible CNT alignment as the core diameter is decreased. The first cylinder represents a 1/16th inch hole drilled in the first stage perform. Here, the CNTs can be in any orientation in the core. The second cylinder represents the fiber core after the first stage draw. The CNTs are more constrained, but not enough to align. The third cylinder represents the fiber core after a second stage draw. The expected core diameter is one micron. Because of the difference in scale between the CNT length and the core diameter of the fiber, the CNTs could potentially orient lengthwise in the core as shown in Figure 2.

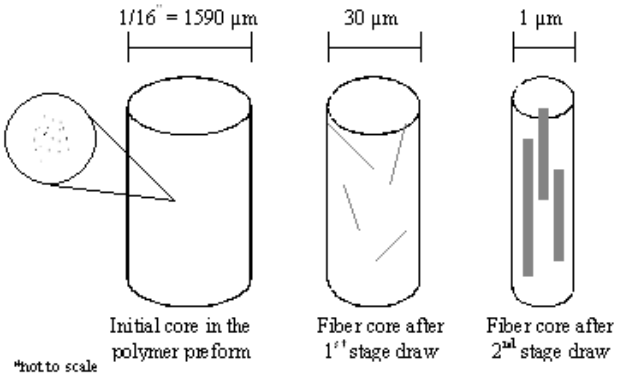

Figure 2. Expected CNT alignment after second stage draw.

Viscous forces exerted on the CNTs during the draw process are also expected to aid in aligning the CNTs lengthwise along the axis.

CNTs have very unique electrical, optical, thermal, and mechanical properties. CNTs are more electrically conductive than aluminum.In the carbon nanotube conductance experiments performed by Stephan Frank et al, it was discovered that CNTs behaved as ballistic conductors.[1] Ballistic conductors expel any electron that enters an opening without electron scattering. Aligned CNTs could be used to form an electrical circuit. The luminescence of CNTs could be applied to single molecule light emitters.[2] With the combined electrical and optical qualities of CNTs in acrylic fiber, both electrons and photons could be sent along the same fiber. This will save space making smaller, more efficient devices. The thermal qualities of CNTs allow them to conduct heat and maintain stability at high temperatures due to their "perfect conjugated system".[3] The mechanical properties of composite polymer fibers could

potentially be improved by incorporating CNTs because of their mechanical strength. They are 1000x stronger than steel while maintaining a high elastic modulus. Composite fibers with CNTs could be integrated into future mechanical devices of varying function, thereby improving the mechanical properties of the composites in which the fibers are used.

Current fiber optic cables are inorganic (made of silica), while these new fiber optic cords are an organic composite comprised of a polymer capillary fiber with a CNT filled core. The acrylic preforms can be made into fibers using a lower processing temperature than what is needed to make silica fibers. This is important because the oil that the CNTs are dispersed in cannot withstand the temperature needed to draw silica fibers.

The properties of single walled carbon nanotubes (SWCNTs) are more impressive than those of multi walled carbon nanotubes (MWCNTs). For example, each additional CNT wall decreases the mechanical strength of the CNT. However, until the process for aligning CNTs in polymer fiber has been perfected, MWCNTs will be used because they are less expensive.

The polymer fibers with CNT-filled cores are produced using a multi-stage draw process. The fiber draw process begins with a commercially available cylindrical preform of acrylic. The outer diameter of the preform is 1" and it is then machined with a 1/16" diameter hole centered on the axis. A commercially available dispersion of CNTs in oil is incorporated into the 1/16" diameter hole of the preform. This 1/16" hole becomes the inner CNT-filled core of the fiber being produced. Using the draw tower facility shown in Figure 3, the preform is drawn into fiber with an outer diameter of approximately 500 microns and an inner core diameter of approximately 30 microns.

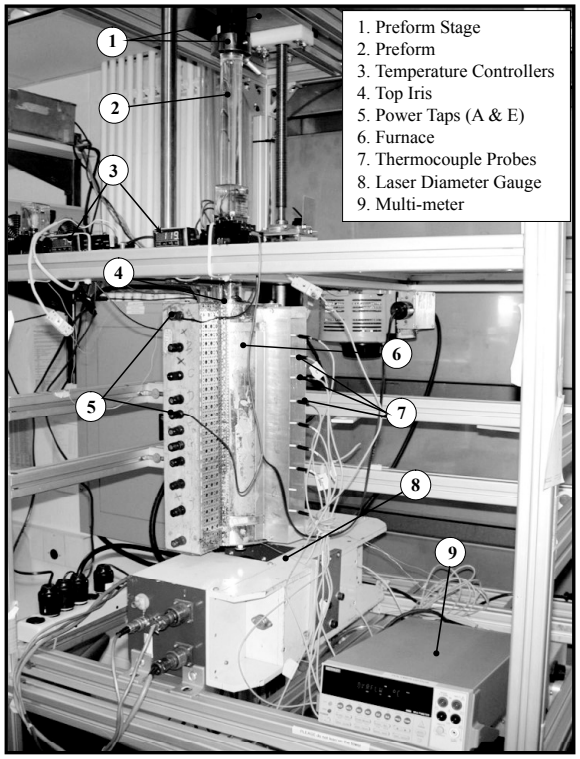

Figure 3. Fiber draw tower.

To begin the process the lower portion of the preform is lowered into a heated furnace. Heat is transferred to the preform in the furnace. Near the peak temperature in the preform it begins to neck down into fiber.

The weight of the preform below the neck down point pulls the lower end of the preform downward. Once the bottom of the preform reaches the floor, the fiber is cut and threaded into the fiber take-up system, which leads the fiber to a collection spool. After the fiber is cut, the feed motor for the preform and the draw motor for the fiber are turned on. Figure 4 (next page) is a schematic of the steady-state drawing process.

In a second stage fiber draw, the product of the first draw is sandwiched between two rectangular acrylic slabs and drawn again. One of the rectangular slabs has a lengthwise groove to hold the fiber. This second stage draw yields a fiber with a much smaller core, on the order of one micron. The second stage fiber draw was expected to decrease the core diameter sufficiently to produce CNT alignment.

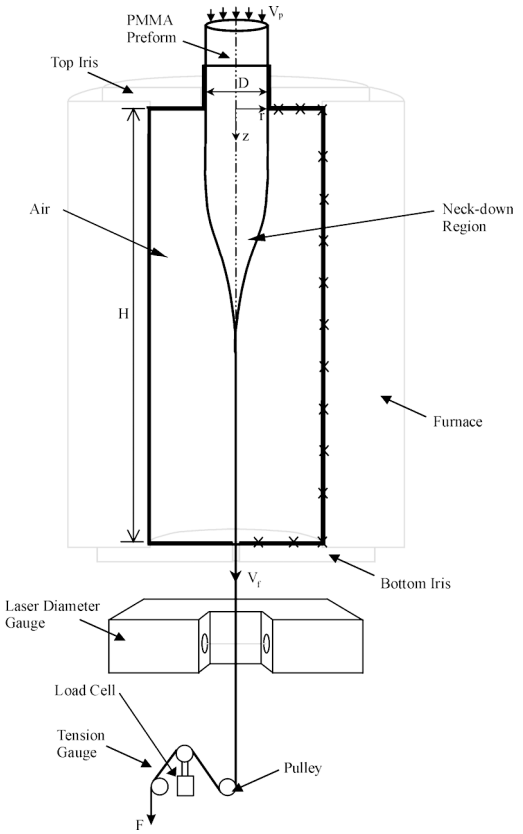

Figure 4. Fiber draw schematic.

One of the key principals of the fiber draw process is conservation of mass. Under steady-state conditions, the mass flow rate (mass per unit time) of material going into the heated furnace must equal the mass flow rate of the material exiting the furnace. Since the density of the material can be treated as constant, the volumetric flow rates are also equivalent at steady-state. This means that the velocity of the fiber coming out must be much faster (measured in cm/s) than the velocity of the preform coming in (measured in microns/s). Three important parameters that can be independently controlled for a fiber draw process are: 1) the velocity of the preform entering the furnace, 2) the cross-sectional area of the preform, and 3) the velocity of the exiting fiber. When the fiber draw process begins, the conditions are transient, but after some period of time, the process reaches steady-state conditions and the volumetric flow rates entering and exiting are equivalent. As shown by the following equations (Figure 5), for a given preform velocity, cross-sectional area, and fiber velocity, there is only one unique fiber cross-sectional area, and hence diameter, that satisfies the volumetric balance under steady-state conditions. Therefore, the exiting fiber diameter is used as an indication for when steady-state conditions have been reached. A second important principal is that the aspect ratio stays relatively constant except with the presence of air or significant surface tension forces.

$\dot{V}_{in}\,(m^3/s) = \dot{V}_{out}\,(m^3/s)$

$\dot{V}\,(m^3/s) = A(m^2)V(m/s)$

$\dot{V}_{in}(m^3/s)$ = Volumetric flow rate of preform entering draw tower

$\dot{V}_{out}(m^3/s)$ = Volumetric flow rate of fiber exiting draw tower

$A_{in}V_{in} = A_{out}V_{out}$

V_{in} = Velocity of preform (m/s) entering draw tower *known*

V_{out} = Velocity of fiber (m/s) exiting draw tower *known*

A_{in} = Cross sectional area of preform (m^2) entering draw tower *known*

A_{out} = Cross sectional area of fiber (m^2) exiting draw tower
determined by conservation of mass at steady-state conditions

Figure 5. Steady state equations

The aspect ratio is defined as the inner hole diameter divided by the outer diameter, $A = d_{inner} / d_{outer}$. For example, a 1" diameter preform with a 1/16" hole will produce a fiber with an inner core whose diameter is $1/16^{th}$ the outer diameter of the fiber. This makes the diameter of the inner core predictable.

Results and Discussion

The initial method for aligning CNTs in fiber was a good idea conceptually, however it had practical problems. Several challenges arose with filling the CNTs into the preform and with imaging the fibers. The viscous CNT dispersion was difficult to load into the preform. Air was trapped within the core making it difficult to completely fill the core with CNTs. The dispersion had the appearance of black tar. It coated the walls of the core so that the air bubbles were not visible. When the preform was heated in order to draw it, the air bubbles expanded, distorting the fiber core as shown in Figure 6. There were some portions of fiber where there were higher concentrations of CNTs in one area than in another, as shown in Figure 7.

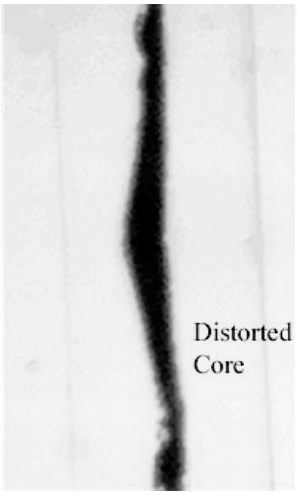

Figure 6. Magnified first stage fiber with distorted core, 40x magnification.

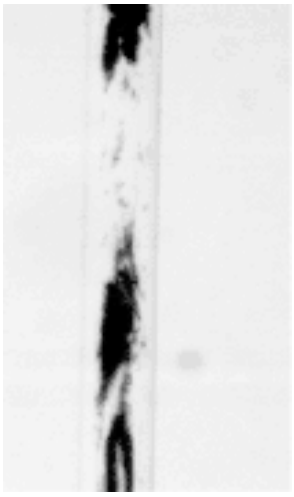

Figure 7. Magnified first stage fiber with regions of lower and higher concentrations of CNTs, 100x magnification.

The fiber produced from the second stage was very difficult to image. There were too many lines in the image and the CNT core could not be easily identified as shown in Figure 8.

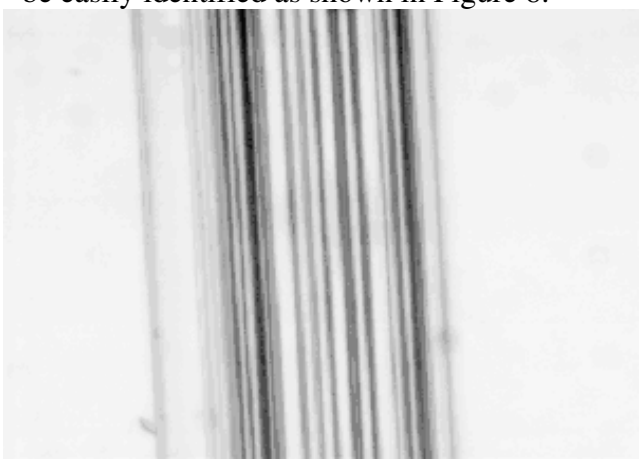

Figure 8. Magnified second stage fiber 100x

In the second stage preform, there are a total of three grooves. The center groove is used to hold the fiber from the first stage draw. Two larger grooves on either side of the center groove serve to catch MMA monomer, which is used to bond the two rectangular slabs of the second stage preform together. These three grooves and the edges of the rectangular preform create many changes in refractive index. This causes the many lines when the fiber is imaged.

Conclusions

In order to avoid these problems, a new plan was developed. The CNT dispersion was injected directly into the middle groove of a second stage preform. After the CNT dispersion was injected into the center groove, a second rectangular slab was bonded to the first using MMA monomer. This preform was then drawn into fiber. The new approach shows promise. It is much easier to fill the core with CNTs because they are injected directly into the groove of the preform as shown in Figure 9.

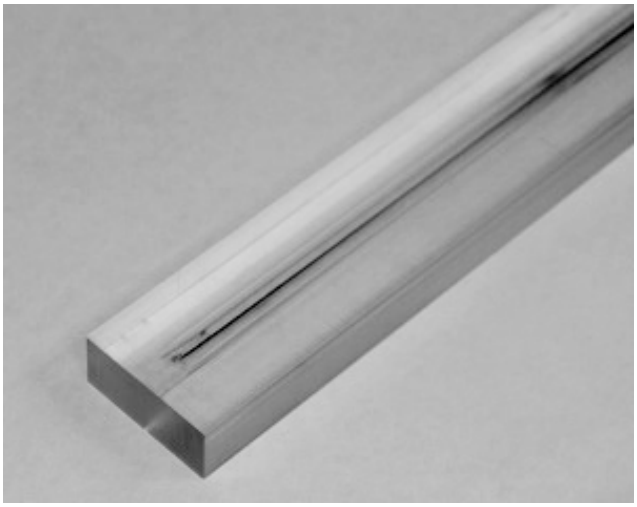

Figure 9. Rectangular slab with CNTs in center groove.

However, for the current 60° groove angle, the free surface of the CNT-liquid dispersion is not flat. This is a problem because when a second rectangular slab is placed on top, air is still trapped in the groove. Figure 10 is an image of the resulting fiber, at 200x magnification.

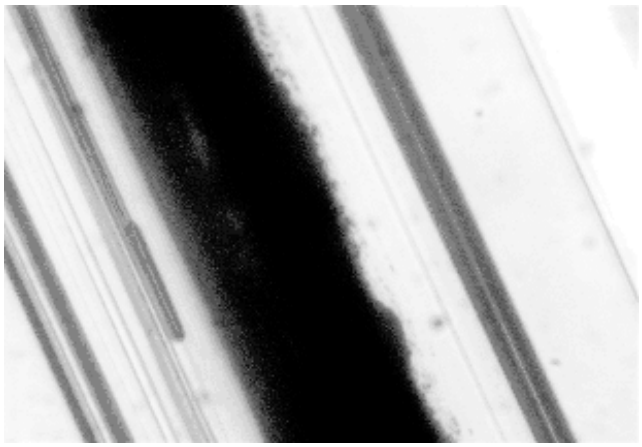

Figure 10. CNT fiber using new approach, 200x magnification.

New test grooves are being machined at 30°, 45°, and 90° angles to determine whether or not the surface of the CNT liquid dispersion can be flattened. If the surface of the liquid can be flattened and the CNT dispersion completely fills the groove, then air will be eliminated from the core. This will prevent expansion and distortion of the core as the fiber is drawn.

More research is required for this project including x-ray diffraction measurement of the fiber, and also the use of SWCNTs rather than MWCNTs. Furthermore, the electrical and optical properties of the fiber should be quantified using different concentrations of CNT dispersions.

X-Ray diffraction (XRD) is being used to determine the orientation of the CNTs. If they have aligned, the readout will have semi-sharp peaks. An amorphous material (unstructured/ formless) will not generate peaks. After a fiber draw method is developed which eliminates air entrapment, the fiber core size should be further decreased to better align the CNTs.

In the future, SWCNTs will replace the MWCNTs currently being used because SWCNT properties are more impressive. Electrical, thermal, optical, and mechanical properties of the fibers will be quantified. Different concentrations of CNT dispersions will be tested since this is expected to have an effect on the fiber properties.

References

1. Stefan Frank, Philippe Poncharal, Z.L. Wang, Walt A. de Heer. *Science,* **1998,** *280,* 1744-1746.

2. Ann Swan, Optical Properties of Carbon Nanotubes, http://nanoscience.bu.edu/nanophotonics05-files/papers/Swan.pdf, (accessed **July 2006)**.

3. Applied Nanotechnologies Inc, Basic Properties of Carbon Nanotubes, http://www.applied-nanotech.com/cntproperties.htm#Mechanical%20Properties, (accessed **July 2006)**.

Acknowledgments

The authors would like to thank the NSF Science and Technology Center No. DMR 0120967 for their generous funding in collaboration with REU CMDITR (the Center on Materials and Devices for Information Technology Research) as well as Kristin Wustholz, Sara Selfe and Dr. Phil Reid.

The work and intellectual input from Dr. Ann Mescher, Greg Winchell, Hien Pham, Russ Noe and Kevin Soderlund was vital to the success of this project.

Personal Statement

I am currently pursuing my Bachelors degree in Zoology. I plan to go to Veterinary school and eventually open my own practice.

Partition Coefficient of 2,5-Diphenyl-1,4-Benzoquinone Within a Lipid Bilayer

Savannah V. Burnside, University of Arizona

Anthony Marshall, S. Scott Saavedr, Department of Chemistry, University of Arizona

Introduction

Commercial solar energy production requires ultra-pure silicon which is costly to produce. The pure silicon is used for the production of solar panels which convert solar energy to electrical power. In nature, photosynthesis is carried out by many biological systems such as bacteria and plants. Sunlight is absorbed by antenna molecules and converted to chemical energy. Within bacteria, chemical energy is created through charge separation in or across a lipid membrane. In this research, an artificial photosynthetic reaction center and a proton transporter are being used to mimic charge separation in bacterial photosynthesis. The long term goal is to create alternatives to solar technology.

The main focus of this project is the proton transporter, 2,5-diphenyl-1,4-benzoquinone (BQ), which is used to shuttle protons across a lipid bilayer, composed of L- -Phosphatidylcholine (EggPC). Previous research conducted by collaborating research teams, Saavedra and Armstrong et al. [1] from the University of Arizona and Gust, Moore and Moore et al. [2,3] from the Arizona State University, have shown that the BQ is soluble in a lipid membrane and functions as a proton transporter. However, to perform this function the BQ must remain dissolved in the lipid membrane rather than the surrounding aqueous phase.

The goal of this project is to determine the partition coefficient of BQ between the lipid bilayer and water.

Background

Research conducted by Gust, Moore and Moore from the Arizona State University found that BQ functioned as a proton transporter within the bilayer of a lipid vesicle. Figure 1 shows a schematic of a lipid vesicle containing artificial photosynthetic reaction centers (C-P-Q) and BQ.

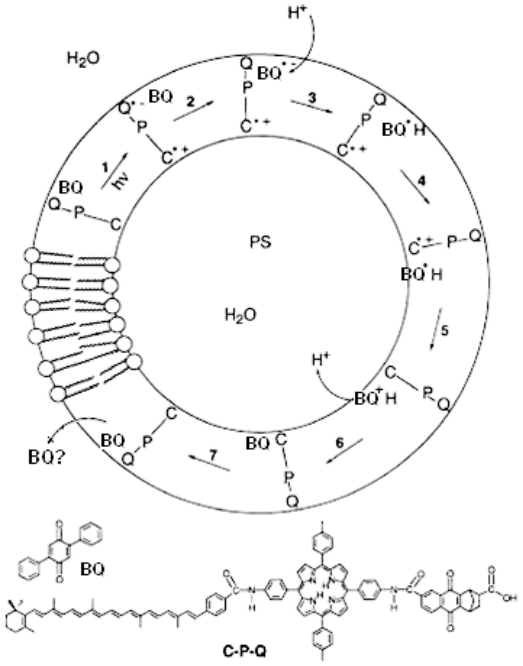

Figure 1: Schematic of a lipid bilayer vesicle that contains the artificial reaction centers (C-P-Q) and proton shuttles (BQ). The BQ is contained within the lipid bilayer and diffuses from the outer edge to the inner lipid layer. Light is absorbed by the artificial reaction center, C-P-Q, a synthetic tetraarylporphyrin (P), a quinone group (Q) and a carotenoid polyene (C), which causes a charge separation yielding C+-P-Q-. The $Q^{\cdot-}$ reduces BQ, which simultaneously binds to a H+ from the external buffer, then diffuses across the lipid bilayer where simultaneously H+ dissociates and C+ is reduced, regenerating BQ. H+ is released into the interior of the vesicle. BQ diffuses back to the outer lipid layer.

The partition coefficient (K), is given by equation 1,

$$\text{Partition Coefficient} = \frac{\left[BQ_{\text{vesicle,MAX}}\right]}{\left[BQ_{\text{aqueous,MAX}}\right]}$$

where $BQ_{\text{vesicle,MAX}}$ is the concentration of BQ within the lipid vesicle and $BQ_{\text{aqueous,MAX}}$ is the

concentration of BQ outside the vesicle in the surrounding aqueous solution.

The partition coefficient of BQ is expected to be >1000 due to its hydrophobic structure. With the majority of the BQ remaining in the vesicles, as predicted, there will be a small amount of BQ to detect in the outside aqueous solution.

The partition coefficient is determined by measuring the concentrations of BQ in the surrounding aqueous and in the vesicle. Using an extrusion technique, lipid vesicles were made containing BQ in the lipid bilayers of the vesicles. Dialysis was used to separate BQ in the aqueous solution from BQ in the vesicles. Liquid-liquid extraction and UV-Visible spectroscopy were used to measure BQ in each phase.

Experimental Section:

Materials. All materials were obtained commercially and were not further purified. The BQ was obtained from Alfa Aesar (Ward Hill, MA). Toluene, ethanol, chloroform and acetone were purchased from EMD Chemicals Inc. (Gibbstown, NJ). L- -phosphatidylcholine (EggPC, Chicken) was purchased from Avanti Polar Lipids, Inc. (Alabaster, AL). 1,2-Dioleoyl-sn-glycero-3-phosphoethanolamine-n-lissamine rhodamine B sulfonyl (Rhodamine-DOPE Dye) was purchased from Avanti-Polar Lipids Inc. (Alabaster, AL). All solutions were prepared with deionized water (DI water, 18 Mohm cm) using a Millipore–Q system. All glass vials, cuvettes and test tubes were cleaned in piranha solution (3:7 volume ratio of hydrogen peroxide:concentrated sulfuric acid), then dried in a stream of N_2.

First a calibration curve for BQ in toluene was constructed. The absorbance of a series of dilutions was obtained using a Ultraviolet-Visible Spectrometer (UV-VIS), Model 430/440 Spectrophotometer, Spectral Instruments, Inc and plotted versus the concentrations.

Lipid vesicles containing BQ were prepared by vacuum drying and rehydrating with DI water. The mole to mole ratio of 5:100 for BQ to lipid was maintained. After four hours, the lipids and BQ were rehydrated with DI water to yield a lipid concentration of 0.5 mg/mL. The solution was then vortexed until all visible solids were dissolved. The sample was then sonicated, Sonicator W-380, Heat Systems – Ultrasonics, Inc. (Farmingdale, NY), for 3 minutes at 40% output at 25° C. The solution was then put through a freeze dry process where vials containing the solution were submerged in an isopropyl alcohol and dry ice bath. The visible liquid was frozen, then placed in a 30° C water bath to thaw. Ten freeze-thaw cycles were performed.

An extrusion technique was used to obtain the desired unilamellar vesicles containing BQ, illustrated in Figure 2. The vesicle and BQ solution was extruded twice through a series of 0.6 μm, 0.4 μm, 0.2 μm and once through 0.1 μm micropore filters, Track-etched membrane, Whatman-Nuclepore (Pleasanton, CA), under argon.

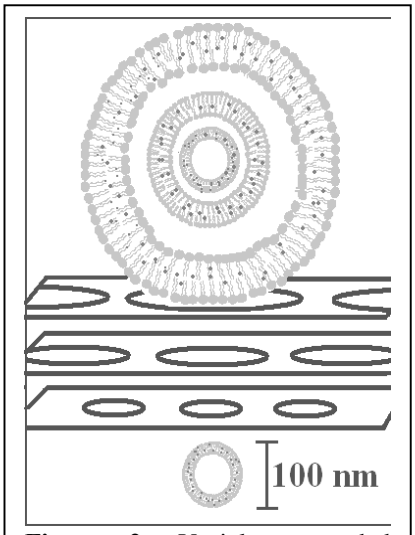

Figure 2: Vesicles extruded through a series of decreasing diameter microfilters to yield ~100nm vesicles.

Blank vesicles which did not contain BQ, only EggPC with Rhodamine-DOPE were made. A 1:50 mole ratio was used for EggPC to Rhodamine-DOPE. The dyed lipids were prepared by vacuum drying for four hours. The lipids were rehydrated with DI water to yield a concentration of 0.5 mg/mL of EggPC in DI water. The lipid solution was then put through the similar 10 cycle, freeze-thaw process performed on the lipid vesicles containing BQ. A 0.5 mL aliquot of the original solution was removed and diluted with 0.5 mL of DI water and sonicated for 30 mins; this solution was not extruded. The remaining lipid solution of Rhodamine-DOPE labeled vesicles was extruded twice through a series of 0.6 μm, 0.4 μm, 0.2 μm and once through 0.1 μm micropore filters, Track-etched membrane, Whatman-Nuclepore (Pleasanton, CA), under argon.

UV-VIS spectra were measured on the two lipid solutions containing Rhodamine-DOPE. The cuvette was cleaned with ethanol, rinsed several times with DI water and dried under a

stream of N_2 between each measurement of the dyed vesicle solutions. A DI water blank was used for spectral subtraction.

The distribution of vesicles sizes within the aqueous solution was measured with light scattering. QELS Start program was used for analysis of the light scattering data. Glass test tubes which had been cleaned in piranha solution were filled with a 0.1% concentration of the solution. The concentration was adjusted based on the recommended operating rate of the laser, Melles Griot (Carlsbad, CA), which is between 40 and 80 Hz. If the operating rate was $\leq$ 40 Hz, the concentration would need to be increased. If the operating rate was $\geq$ 80 Hz, the solution would need to be diluted.

The concentration of the BQ in the aqueous solution was determined by use of a dialysis technique. Molecular porous membrane tubing (dialysis tubing, Spectra/Por) was used to separate the vesicles from a larger volume of DI water. The extruded vesicles were placed in a dialysis tube with a MWCO of 6,000-8,000 and submerged in a known volume of DI water. The dialysis system remained on a stir plate for 38 hours before the dialysis tube was removed. BQ was equilibrated between the vesicles and the surrounding aqueous solution.

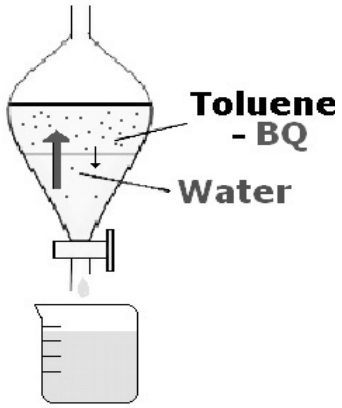

Figure 3: Illustration of liquid- liquid extraction of BQ from aqueous solution with toluene.

A liquid-liquid extraction technique was used to extract BQ from the surrounding aqueous solution. A 1:100 volume ratio of toluene to aqueous solution was used in the extraction of BQ. The aqueous solution was added to a glass separatory funnel and then toluene was added. The funnel was shaken by hand to allow a mixing of the solutions. The solution was shaken 3 times for 20 second intervals, then suspended and allowed to separate for an hour before the upper toluene phase was extracted. A second extraction was repeated to remove any remaining BQ, again the solution separated for an hour before the upper toluene phase was extracted. At least 1 mL of toluene solution was removed during each of the extractions for UV-VIS measurements.

UV-VIS spectra were taken of the toluene extracted solutions. The cuvette was cleaned with toluene between each the measurement of each extracted solution. The toluene blank was used for spectral subtraction.

Results and Discussion

The calibration curve was obtained by dissolving BQ in toluene and making a series of dilutions. In Graph 1 a defined peak for BQ in toluene was found to have a maximum absorption (λ_{max}) at 341 nm. A linear plot, shown in Graph 2, of the absorbance (abs) at λ_{max} versus concentration shows the molar absorptivity, , to be 10600 $M^{-1}cm^{-1}$. The molar absorptivity was used in calculating the concentration of BQ in the liquid-liquid extraction and vesicle preparation procedures.

The UV-VIS spectra taken of the Rhodamine-DOPE vesicle solutions showed a decrease in abs after extrusion. The decrease in the extruded absorbance relative to unextruded absorbance, seen in Graph 3, was assumed to be directly proportional to the loss of lipids, including EggPC, during extrusion. The percent lipid retention is given by equation 2,

$$\%\ \text{lipid retention ratio} = \frac{\text{extruded abs}}{\text{unextruded abs}} \times 100$$

$$= \frac{0.65}{1.19} \times 100 = 54.6 \approx 55\%$$

where extruded abs is the absorbance of the rhodamine labeled vesicles after the extrusion process. The unextruded abs is the absorbance of the solution which was not extruded. Based on the results of the spectra about 55% of the lipids remained after extrusion and about 45% was loss.

A UV-VIS spectra obtained of the toluene extraction from the dialysis solution did not yield a detectable abs at 341nm. Based on the calculations using the molar absorptivity, , and the initial concentration of BQ, 3.29e-5 M used for dialysis, an absorbance of ~0.35 should have been visible at 341 nm, as shown in Graph 1.

The partition coefficient given by equation 1, is a calculation of the concentration of BQ in the surrounding aqueous and lipid vesicles. Since there was no visible absorbance of BQ in the surrounding solution, the minimum detection limit, mdl AU, of the UV-VIS instrument was used to determine the minimum detectable concentration M, mdc, of BQ, shown by equation 3.

$$\frac{\text{mdl AU}}{\varepsilon\,\text{M}^{-1}\bullet\text{cm}^{-1}} = \text{mdc}\,\underline{\text{M}}$$

$$\frac{0.002\,\text{AU}+0.005\,\text{AU}}{10600\,\text{M}^{-1}\bullet\text{cm}^{-1}} = 6.607e\text{-}7\,\underline{\text{M}}$$

The detection limit, mdl, of the instrument was listed as 0.002 $\pm$ 0.005 AU in the users manual. The minimum concentration detectable by the UV-VIS is 6.607e-7 M, which is the concentration of BQ in toluene. The moles of BQ given by equation 4,

$$\text{m dc}\,\underline{\text{M}}\times\text{vol}_{\text{TOL}}\text{mL}\times\frac{1\text{L}}{1000\text{mL}}$$

$$=\text{moles of BQ}=\text{BQ}_{\text{aq}}$$

$$6.607e\text{-}7\underline{\text{M}}\times 3\text{mL}\times\frac{1\text{L}}{1000\text{ mL}}$$

$$=1.98e-9\text{ moles of BQ}$$

where BQ_{aq} is the maximum moles of BQ that has diffused into the aqueous and vol_{TOL} is the volume of toluene used to extract the BQ. The concentration of the BQ in the aqueous, $[BQ_{aqueous,MAX}]$ is given by equation 5,

where $vol_{aqueous}$ = 300 mL + 7.75 mL, the sum of the volume of DI water used in the aqueous surrounding the aqueous and the 7.75 mL of DI water used in the vesicle production.

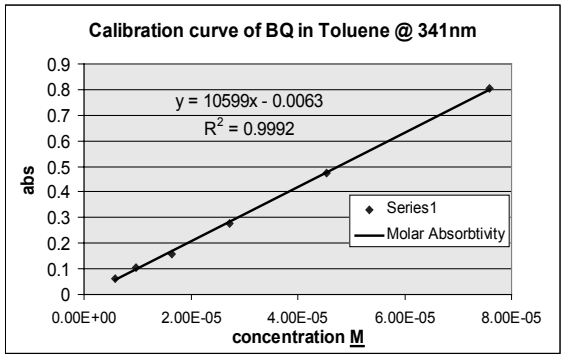

Graph 2: A plot of the concentration versus absorbance at 341nm of a series of concentrations of BQ in toluene.

By determining the maximum concentration of BQ in the aqueous solution, the minimum concentration of BQ in the vesicles can be calculated. An estimate of the minimum concentration of BQ in the vesicles is given by equation 6,

$$[\text{BQ}_{\text{vesicle,MAX}}]\,\underline{\text{M}}=\frac{\text{BQ}_{\text{max}}\,\text{moles}\;-\;\text{BQ}_{\text{aq}}\,\text{moles}}{\text{vol}_{\text{ves}}\,\text{mL}}$$

where $[BQ_{vesicle,MAX}]$ is determined by the initial

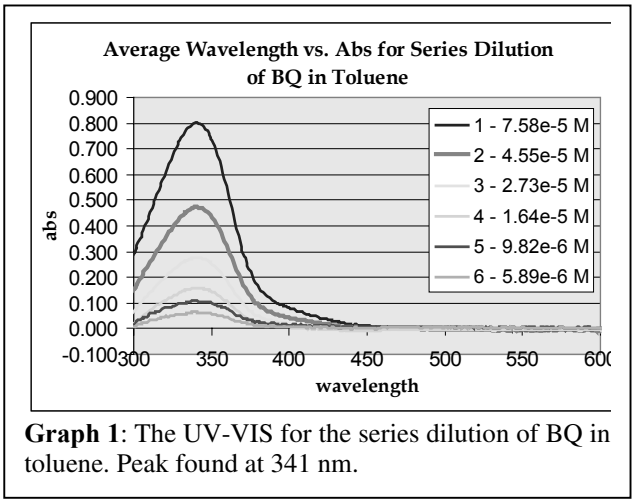

Graph 1: The UV-VIS for the series dilution of BQ in toluene. Peak found at 341 nm.

moles of BQ, BQ_{max}, minus the moles of BQ, that diffused into the aqueous solution, BQ_{aq}, given by equation 4, and divided by the volume of the lipid bilayer, vol_{ves}.

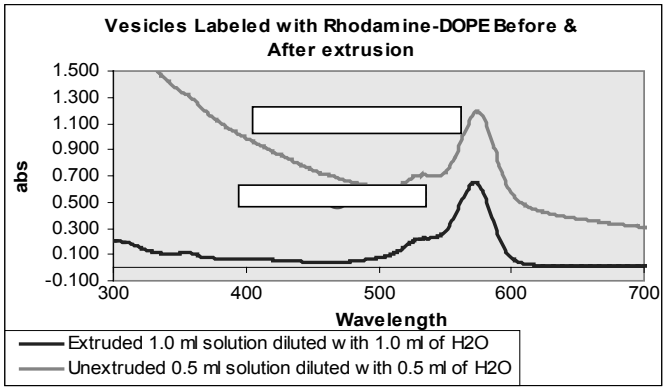

Graph 3: UV-VIS of rhodamine labeled lipids before and after extrusion

The volume of the lipid bilayer was determined by the volume of a lipid and the number of lipids retained after extrusion. The number of lipids retained after extrusion was determined by equation 7,

$$\text{number of lipids} = \frac{\text{vol}_{\text{lipid,I}}\,\mu\text{L} \times \%\text{ lipid retention} \times \text{conc}_{\text{lipid,I}}\,\text{mg/mL} \times N_A}{1e6 \times \text{MW}_{\text{lipid}}\,\text{g/mole}}$$

$$= \frac{388\ \mu\text{L} \times 0.55 \times 10\ \text{mg/mL} \times 6.023e23}{1e6 \times 760.08\ \text{g/mole}} = 1.69e18\ \text{lipids}$$

where $\text{vol}_{\text{lipid,I}}$ is the initial volume of lipid used, % lipid retention from equation 2, $\text{conc}_{\text{lipid,I}}$ is the initial concentration of the lipid used for extrusion and N_A is Avagadro's number. MWlipid is the molecular weight of EggPC.

Previous research conducted by Lee et al. [4] found the lipid surface area, SA_{lipid}, to be 60 Å^2 and the bilayer thickness, BT_{lipid}, to be 50 Å. The total volume of the lipids, $\text{vol}_{\text{lipid,F}}$ is given by equation 8.

$$\text{vol}_{\text{lipid,F}}\,\text{L} = \frac{SA_{lipid}\,\text{Å}^2 \times (BT_{lipid}\,\text{Å} \div 2) \times \text{number of lipids}}{(1e\text{-}8)\text{^}3} \qquad (equation\ 8)$$

$$= \frac{60\,\text{Å}^2 \times (50\,\text{Å} \div 2) \times 1.69e18\ \text{lipids}}{(1e\text{-}8)\text{^}3} = 2.54e\text{-}6\ \text{L}$$

The final volume of the vesicles was used to determine the concentration of BQ in the vesicles, $[BQ_{vesicles,MAX}]$ using equation 6.

$$\frac{2.55e\text{-}7\,\text{moles} - 1.98e\text{-}9\,\text{moles}}{2.54e\text{-}6\,\text{L}} = 9.99e\text{-}2\,\underline{\text{M}}$$

Equation 5 and equation 6 were used in calculating the partition coefficient of BQ between the lipid bilayer and water.

$$= \frac{9.99e\text{-}2\,\underline{\text{M}}}{6.44\text{e-}9\ \underline{\text{M}}} = 1.55e7$$

Due to the larger partition coefficient it appears that majority of the BQ is remaining in the lipid bilayer and not diffusing to the outside aqueous. The partition coefficient of BQ within the lipid bilayer remains large regardless of the amount of BQ retained. Assuming a 55% retention of vesicles and 75% retention of BQ, the partition coefficient is 1.16e7. Even with a 10% retention of BQ the partition only drops an order of magnitude, 1.44e6. This shows that BQ remains primarily in the lipid bilayer and can be used as a proton transporter, which will eventually lead to the production of a proton gradient. This gradient is crucial to the eventual production of mechanical work.

Future:

Alternatives to the insertion of BQ into the lipid bilayer need to be investigated, in an attempt to quantify the concentration of BQ in the vesicles after the extrusion process. Due to the absence of a peak, which should have been obtained with a spectra of the extracted toluene solution, the loss of BQ during extrusion of the lipid vesicles should be examined. Future research needs to be completed on the use of lipids other than the current EggPC lipid bilayer. Other lipids may provide a more stable environment for the proton transporter. They may hold a higher concentration of BQ than the current 5% mole to mole ratio for BQ in EggPC, without disruption to the lipid membrane. Also other characteristics of BQ such as the reduction potential of BQ within the lipid bilayer need to be examined. The shuttling of protons across the lipid bilayer by BQ is affected by the ability of the reaction center to create a charge separation. If the reduction potential of BQ is not between the potentials associated with the reducing agent, quinone group (Q), and the oxidizing agent, carotenoid polyene (C), then BQ will not be able to shuttle protons across the lipid bilayer.

References:

1. McBee, Todd W.; Wang, Liying; Ge, Chenhao; Beam, Brooke M.; Moore, Ana L.; Gust, Devens; Moore, Thomas A.; Armstrong, Neal R.; Saavedra, S. Scott; "Characterization of Proton Transport across a Waveguide-Supported Lipid Bilayer". *J. Am. Chem. Soc.* 2006, *128*, 2184-2185

2. Steinberg-Yfrach, Gail; Liddell, Paul A.; Hung, Su-Chun; Moore, Ana L.; Gust, Devens; Moore, Thomas; "Conversion of light energy to proton potential in liposomes by artificial photosynthetic reaction centres". *Nature* 1997, *385*, 239-241.

3. Gust, Devens; Moore, Thomas; Moore, Ana L.; "Mimicking Photosynthetic Solar Energy Transduction". *Accounts of Chemical Research* 2001, *34*, 40-48.

4. Lee, Dong-Chan; Chang, Bong-Jun; Yu, Luping; Frey, Shelli L.; Lee, Ka Yee C.; Patchipulusu, Sirisha; Hall, Connie; "Polymer Cushions Functionalized with Lipid Molecules". *American Chemical Society* 2004, *20*, 11297-11300

Acknowledgements:

This work was made possible by the NSF sponsored Science and Technology Center (STC) on Materials and Devices for Information Technology Research (MDITR), No. DMR-0120967 and the Ronald E. McNair Achievement Program. I would also like to thank the Saavedra Group: James Joubert, Han Zhang, Kristina Orosz, Chenhao Ge, Varuni Subramaniam, and Yaning Ma for their advice and time in teaching me how to operate the different instruments I utilized during my internship.

Personal Statement:

I plan to finish my undergraduate education at the University of Arizona in Materials Science and Engineering and my future plan is to obtain a Ph.D in Bio-medical Engineering.

Holographic Image Recording in Azo Dye Doped Polymer Films

Brice Cannon

Norfolk State University Department of Engineering, Norfolk State University, Norfolk, Virginia

Dr. Jayan Thomas and Dr. Nasser Peyghambarian,

College of Optical Sciences,The University of Arizona, Tucson, Arizona

Introduction

The objective of our research was to develop a holographic rewritable medium using azo dye doped polymers. Holography is an advanced form of imaging used to capture an interference pattern in a material. One of the most important aspects of modern optics is the capability to store and process optical information in a high density material. Holographic rewritable storage media can store up to 100 times more information per micron than a DVD.

Trans-cis photoisomerization is one of the mechanisms that can be used to record a holographic image. Photoisomerization is a process in which the molecular structure changes occur by photoexcitation. It can be reversible or irreversible. Photoisomerization in azo dye doped materials take place by *trans* to *cis* conversion. Trans form is when two functional groups are present on the opposite sides of the double bond and cis is when they are attached on the same side.

Materials and Methods

Several azo dye incorporated polymer based films were prepared for writing holograms. The films contained various concentrations of dye and different thicknesses. The concentrations ranged from 0.5% - 2% and the thicknesses ranged from 10 microns to 105 microns. The thickness was controlled using glass bead spacers.

The azo dye that was investigated in this research was disperse red 1. This azo dye has many promising capabilities to allow rewritable holographic data storage. The technique of holography can be used to receive, process, and store data. The polymers that were used as an inert medium for the azo dye were PATPD and polystyrene.

The linear absorption spectrum of the sample was a preliminary characterization tool to identify any new chemical or physical interactions that may arise after mixing the different components together. It can also give an insight into the formation of dye aggregates and charge transfer complexes, which occur in the composite. The absorption spectrum facilitates the identification of the species in the composite by a proper correlation between the composite spectra. These studies also provide important information regarding the best excitation wavelengths.

The linear absorption spectrum can be measured using a UV-Vis absorption spectrophotometer. In our research it was used to determine the optical density and wavelength of light that can be used for writing and reading the holograms in the devices developed.

The differential scanning calorimeter, or DSC, was used to measure the glass transition temperature of the composite**.** The glass transition temperature of the composite was an important characteristic since it is the temperature at which the polymer becomes more flexible. Hence, ease of orientation of the dyes in the polymer can be inferred from the glass transition temperature. Small molecules called plasticizers were used to adjust the glass transition temperature. The plasticizer used was Ethyl carbazole (ECZ).

Figure 1 shows the experimental setup used to read and write the holograms. Four-wave mixing was used to write and read the holograms. This technique uses two s-polarized beams at 532nm for

recording and an s-polarized beam at 632nm wavelength to probe the grating. The probe beam counter-propagating to one of the writing beams was diffracted from the grating.

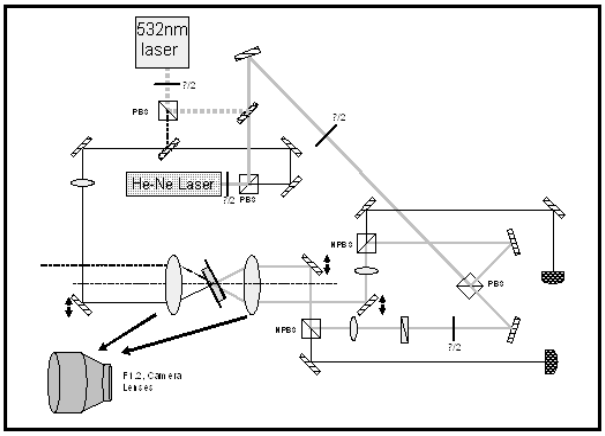

Figure 1. The holographic recording optical setup used to record the holograms. Two s-polarized lasers were used to read and write the holograms. Green writing beams and red probe beam were used.

The grating persistence was examined using a probe beam to monitor the diffraction efficiency at different time intervals after the writing beam had been turned off. The thermal reversibility of the holograms written can be checked by heating the sample to a higher temperature.

Results and Discussion

The recorded holographic image has to be intense enough to allow a probe beam to read the hologram. A high intensity probe beam can be used to read the holograms with low efficiency.

Absorption Coefficient was calculated from optical density (O.D) using the formula

$$\text{Absorption Coefficient} = 2.3(\text{O.D})/t \qquad (1)$$

where t is the thickness (in cm) of the film. Optical density from one of the samples is shown in Figure 2. The optical density peaks at a wavelength of about 480nm. Any wavelength near this value can be used for photoexcitation.

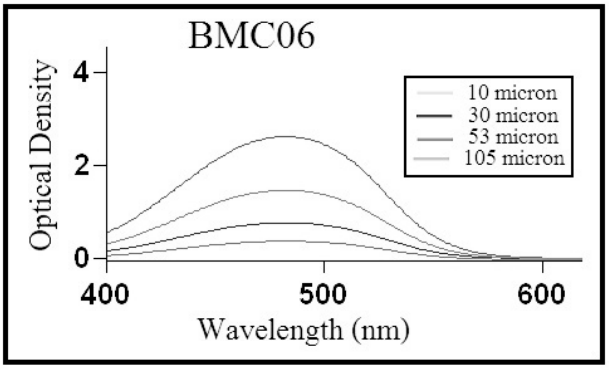

Figure 2. Optical density of the films prepared. The optical density reaches a peak around 480 nm therefore; a good photoexcitation wavelength would be 532 nm.

The diffracted signals of the devices were recorded using an s-polarized green laser (532 nm) and read using a red laser (630 nm). The green recording laser was used because it was close to the peak absorption wavelength and allowed trans-cis photoisomerization to occur.

Internal diffraction efficiency was calculated from the formula

$$\eta_{int} = I_d/I_t \qquad (2)$$

where I_d and I_t are the intensities of diffracted and transmitted beams respectively. The external diffraction efficiency was obtained by considering material losses such as absorption and reflection and is always less than the internal efficiency.

Sample Information

Sample Name	Thickness (micron)	Abs. Coefficient (532 nm) (1/cm)	Writing/ Reading beam	Efficiency %
BMC02	30	1269.79	Green/Red	.032
BMC03	30	1747.36	Green/Red	.063
BMC05	30	650.53	Green/Red	.012
BMC06	30	293.89	Green/Red	.022
BMC07	30	667.64	Green/Red	.012
BMC08	30	979.03	Green/Red	.030

Table 3. Properties of the holographic devices developed

The diffraction efficiencies obtained were low for the azo dye doped polymer films developed. The 30 micron BMC03 with 98 wt% polystyrene and 2 wt% disperse red had the highest diffraction efficiency of 0.063% and highest absorption coefficient of 1747cm^{-1} as seen in Table 3. These values are lower than some of the other organic

holographic devices. The efficiency can be increased by further optimizing the materials.

Persistence is the rate at which the diffraction signal dissipate over a given time period. High persistence will allow a holographic image to remain visible for longer time after the writing beam has been turned off. When the writing beam was turned off around 7 minutes BMC 03 displayed the highest persistence as shown in Figure 4.

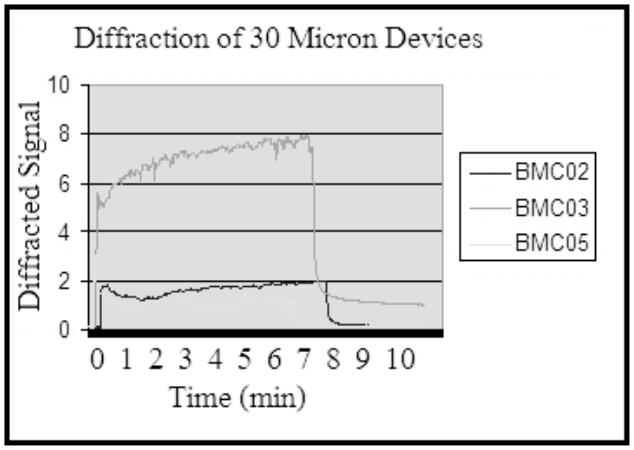

Figure 4. The diffracted signal as a function of time. The BMC03 shows the highest persistence when the writing beam is turned off after 7 minutes.

When the writing beams were turned on, the diffraction of the signal increased and reached a constant value. However, when it was turned off there was an immediate drop in the diffracted signal.

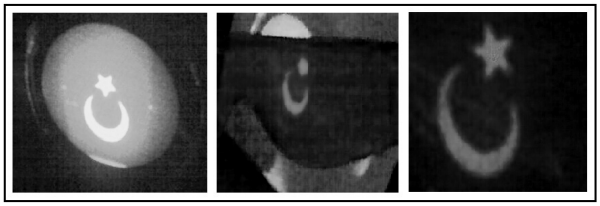

Figure 5. The green image is the transmitted hologram. The red holographic image was reconstructed from the diffracted beam

Figure 5 shows a reconstructed image written in a photorefractive polymer. The azo dye doped polymers developed did not have a high enough diffraction efficiency to produce a reconstructed holographic image from the diffracted beam.

Conclusions

The diffraction efficiencies of the devices developed were too low for practical applications. With further investigations and optimization of the materials, the diffraction efficiency will be able to reach 5% -10%. This diffraction efficiency would be high enough to produce rewritable holograms (similar to that of Figure 5) using azo dye doped polymer films.

References

1. Yavrian, A.; Asatryan, K.; Galstian, T.; Piché, M.; Optics Communications 2005, Vol. 251, 286-291.

2. Pham, Phuc Vinh; Manivannan, Gurusamy; Lessard, Roger A.; SPIE, Vol. 2405, 133-141.

3. Fleck, B.; Dowling, D. A.; Wenke, L.; Journal of Moder Optics 1996, Vol.43, 1485-1493

4. Bian, Shaoping; Zhang, Weiya; Kuzyk, Mark G.; Optics Letters 2003, Vol. 28, No.11, 929-931

Acknowledgments

Funds for this research were provided by the NSF Science and Technology Center on Materials and Devices for Information Technology Research (CMDITR), No. DMR 0120967. I would like to thank Dr. Maclin, Dr. Jones, Dr. Jayan Thomas, and Dr. Nasser Peyghambarian, and other professors who have given the opportunity to succeed as a student and as a student researcher. A special thanks to *Muhsin Eralp*, Semra Bekele, and Savas Tay.

I plan to graduate from Norfolk State University with an Optical Engineering B.S. degree and then pursue a PhD in Optical Physics. I then hope to become a professor at a research university to help students to develop their researching abilities.

Studies of Recombinant Silaffin Attachment to Surfaces for Photonic Crystal Applications

Lindsey L. Carter, Florida Agricultural and Mechanical University, Department of Chemistry

Nicole Poulsen, Simon Jones, Nils Kröger, Seth Marder, Georgia Institute of Technology, Department of Chemistry/Biochemistry

Introduction

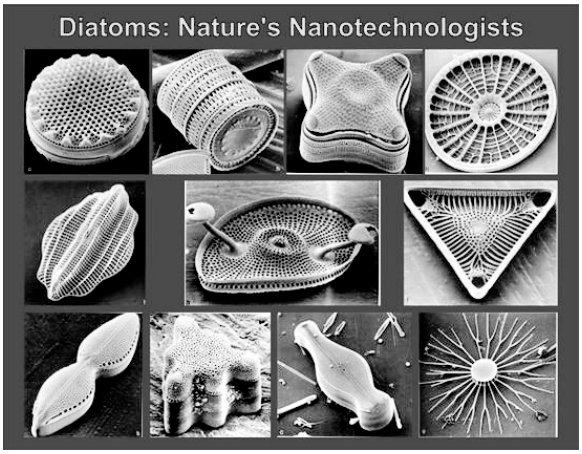

Figure 1. Diatom structures

Diatoms are unicellular eukaryotic algae that have nanostructured silica cell walls (Fig. 1). The biosilica nanopatterns are precisely reproduced in a species-specific manner in each generation; therefore there is a strict genetic control of this biomineralization process.[1] A family of highly modified phosphoproteins, the silaffins have been isolated from diatom biosilica and shown to influence *in vitro* silica formation[1]. As native silaffins from the diatom are highly modified and difficult to purify directly from the diatom in large quantities, the C-terminal region of Sil1 from *Cylindrotheca fusiformis* has been expressed in *E. coli* cells (termed rSilC). Purified rSilC still has *in vitro* silica formation activity, similar to the highly modified native protein, even though it has no post-translational modifications. Furthermore, rSilC is also able to precipitate rutile-phase titania in solution.

rSilC is highly interesting because it has the potential to *specifically* deposit titania on polymer surfaces, which could be used to make photonic crystals. Laser holography or 3D two-photon microfabrication of organic polymers can give well-defined photonic crystal templates, but these processes use materials with relatively small refractive indices. Depositing titania, which has a refractive index of 2.9, on the surfaces of these structures can potentially enable a larger refractive index contrast to be achieved.[2] Having a greater refractive index will potentially allow the structures to be used in a variety of photonic crystal applications.

The mechanism we have employed to attach rSilC to the surface of functionalized glass utilizes the affinity that Ni^{2+}-nitrilotriacetic acid (Ni-NTA) has towards the hexa-histidine tag of the protein, which is also used for the protein purification process. An amino-functionalized Ni-NTA was attached to various surfaces through organic synthetic techniques. The attachment strategies of rSilC to the surfaces are as follows: Glass → Organic Layers → NTA → Ni^{2+} → Protein. We have investigated the use of a "layer-by-layer" assembly to give a hyperbranched, functional surface for protein attachment. By using a dendritic approach, we expect to increase the amount of Ni-NTA sites on the surface relative to the amount that would cover the surface if no layering takes place. This method should potentially allow more protein to coat the surface.

Methods

(I) Protein purification

Recombinant silaffin (rSilC) has been genetically engineered to contain a C-terminal His_6-tag which allows for purification of the protein using a Ni-NTA agarose column. NTA, a tetradentate metal-ion chelating adsorbent, occupies four of the six ligand binding sites in the coordination sphere of the nickel ion. This results in two sites free to interact with the nitrogens of the imidazole ring of histidines.[3] Expression of rSilC is induced in *E. coli* by the addition of isopropyl-β-D-thiogalacto-pyranoside (Fig. 2). To obtain a pure fraction of rSilC, the *E. coli* cells are lysed and the cell lysate is incubated with the Ni-NTA agarose. The Ni-NTA agarose is then washed extensively to remove proteins that might have bound to the resin with low affinity with a low concentration imidazole solution. A higher concentration of imidazole was used to elute the protein from the column. rSilC is a highly positively charged protein at pH 7, therefore a second round of purification using a cation exchange column (High S) was performed.

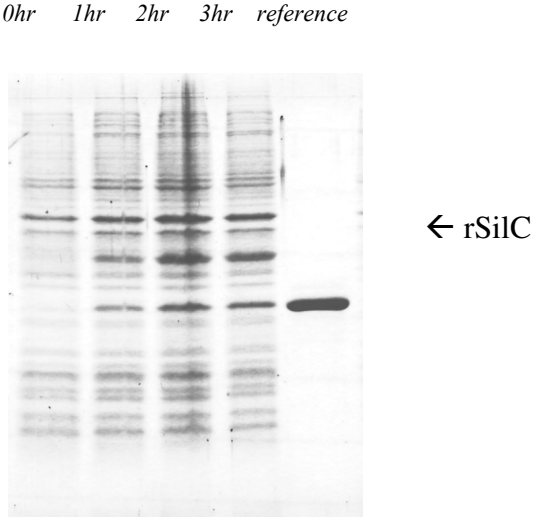

Figure 2. SDS-PAGE of protein amount after induction with isopropyl-thio-galactopyranoside prior to affinity chromatography

(II) rSilC attachment to glass slides

(a) Cleaning of glass slides. The glass slides were cleaned using a 1:1 MeOH/HCl (conc.) solution for 30 minutes, rinsed with deionized water, and dried with a stream of nitrogen. The slides were then submerged in concentrated H_2SO_4 followed by the same rinsing and drying method as described.[4]

(b) Silanization. The surfaces were refluxed in 5% v/v 3-aminopropyl trimethoxysilane in anhydrous toluene for approximately 15 hours at 120°C. This method introduced primary amine groups on the surface that will react in creating layer-by-layer functionalization on the surface.

(c) Surface functionalization. The glass slides were submerged in 20% v/v SR399 (a pentafunctional acrylate, Fig. 3) in absolute ethanol for 1 hour.

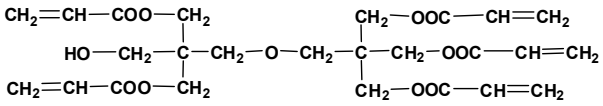

Figure 3. Pentafunctional acrylate

Statistically, one of the five acrylate groups is expected to react with a free amine group on the surface by Michael addition, leaving four acrylate groups available for further reactions. The slides are then submerged in a 20% v/v tris(aminoethyl)amine (Fig. 4) solution in absolute ethanol for 1 hour.

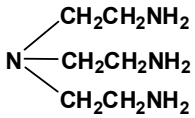

Figure 4. Trifunctional amine

These steps were repeated until layers 1-5 were achieved. The final step in the layering process involved terminating the surfaces with acrylate groups to react with the amino-functionalized NTA. The surface was reacted with 0.1 M NTA (dissolved in deionized water and adjusted to pH 10 by adding NaOH) for 1 hour, followed by incubation in 0.1M ethanolamine dissolved in 20% ethanol/deionized water to cap the unreacted acrylate groups. The last step was treating the slide with 0.9M $NiSO_4$ (dissolved in deionized water and buffered by Tris-HCl at pH 7.5) for 1 hour. At this point, the surface should have the same binding capabilities as the Ni-NTA agarose matrix that was used to purify the protein from *E. coli* (Fig. 5).

(d) Protein attachment. The functionalized slides were incubated with 5mg/ml of rSilC in 50mM Tris-HCl at pH 8 and 1M NaCl (binding buffer). The 1M NaCl is included to counteract electrostatic interactions that may take place between rSilC and the surface.

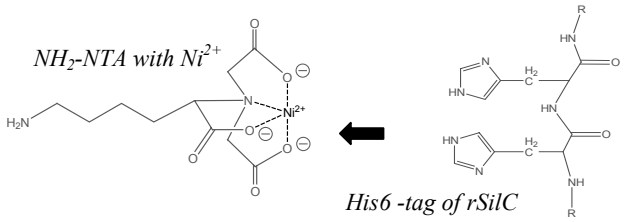

(III) Assessment of surface functionalization and protein attachment

Contact angle measurements were taken with a contact angle analyzing microscope using300 µm droplets of deionized water at room temperature (Fig. 6). Large contact angles show that the surface has hydrophobic functional groups (e.g. acrylates) whereas small contact angles show that the surface has hydrophilic groups (e.g. amines).

rSilC was labeled using fluorescein isothiocyanate (FITC) and tetramethyl rhodamine isothiocyanate (TRITC), respectively, to follow binding of rSilC to the surface using fluorescence microscopy. The isothiocyanate groups of the dyes react with the amine-containing residues of the protein (e.g. lysine).

The following surfaces were prepared serving for control experiments to assess rSilC attachment via the His_6-tag: 1) acrylate-terminated, 2) NTA-functionalized 3) ethanolamine capped. After incubation of the surfaces with fluorescently labeled rSilC, and subsequent washing with binding buffer (3x washing), photos of the surfaces were taken, the samples were rinsed with 4M NaCl (5x rinsing) and 1M imidazole (5x rinsing), respectively, taking photos after each separate washing step.

Results and Discussion

The contact angles of the surfaces were measured to determine if the slides were indeed clean or successfully functionalized after each step. We expected the contact angle of the cleaned glass to be close to zero because the surface should be covered with hydroxyl groups, making it hydrophilic. The contact

angle of the silanized glass was expected to be around 55° (S. Jones, personal communication), which was in good agreement with the obtained result (Fig. 6). The acrylate terminated surfaces were expected to have higher contact angles (more hydrophobic), while the amine terminated surfaces were expected to have lower contact angles (more hydrophilic) than the silanized surface. Based on our angle measurements, the glass was functionalized as we expected (Fig. 6).

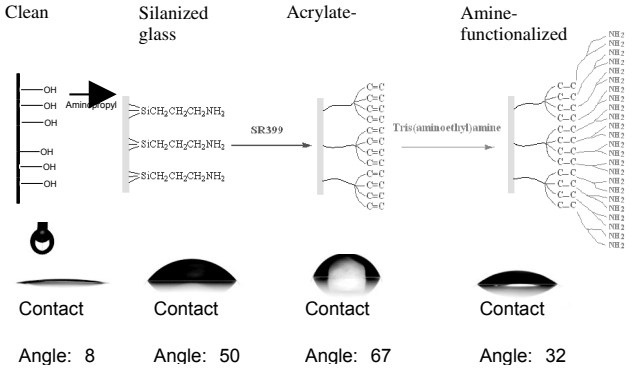

Figure 6. Contact angle comparison of layers.

Attaching rSilC to the functionalized surface by its hexa-histidine tag proved to be more difficult than anticipated. There appeared to be electrostatic interactions between the protein and the surface (Fig.7-A1, A2, C1, C2) as the

fluorescence intensity decreased once the slide had been washed with 4M NaCl. Possible covalent bonding between the terminal acrylate groups and amino acid residues of rSilC could explain the bright fluorescence of Figures 7-D1, D2, F1 and F2. Furthermore, it is inconclusive whether or not capping the acrylate sites with ethanolamine prevents additional protein binding (Fig. 7-B1, B2). Acrylate-terminated and NTA-functionalized surfaces seem to bind protein by interactions other than the hexa-histidine-Ni-NTA interaction (Fig. 7- D3, F3), because the fluorescence intensity does not change after washing with 1M imidazole. However, when the slides A, B, and C were rinsed with 1M imidazole, we observed that the fluorescence does slightly decrease in Figures 7-A3, B3, C3. This suggested that rSilC is binding to the Ni-NTA complexes by the hexa-histidine tag.

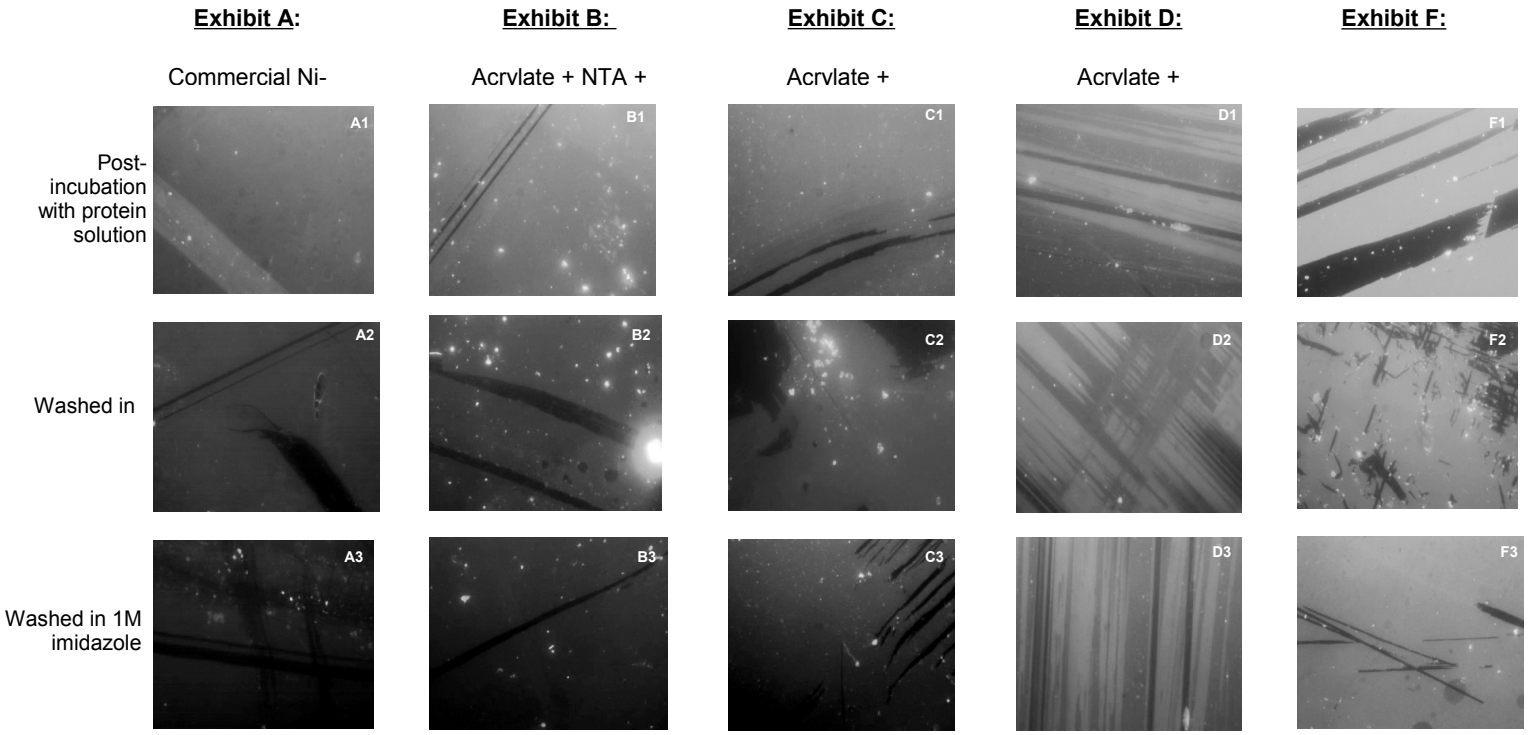

Figure 7. Comparison of the fluorescence of rSilC labeled with FITC on various layers. All pictures were taken at the same exposure time to compare the fluorescence intensities

Conclusions

The results from these studies suggest that rSilC attaches to the surface of functionalized glass in a variety of modes, in addition to the desired hexa-histidine-Ni-NTA interaction. As the fluorescent intensity decreases when the slide is washed with 1M NaCl, this indicates that electrostatic interactions take place on the surfaces. The fluorescent background

seen after washing with 1M imidazole may be due to other interactions. However, further studies are necessary to assess exactly how the protein is attaching to the various surface.

In analyzing protein attachment, one major concern arises with the fluorescent dyes that were used. FITC bleaches quickly when exposed to UV irradiation through a FITC filter (450-490 nm), which could lead to inaccurate results of how intensely the surface fluoresced after each washing treatment. Experimental evidence suggests that TRITC itself has a strong affinity for the glass surface. presumably due to its amino groups. Furthermore, the fluorescence coverage was not completely uniform over the surface, which may result in discrepancies when comparing photos after each step, because it is not certain that identical areas on the surface were being photographed.

REFERENCES:

1. M. Sumper and N. Kröger, *J. Mater. Chem*., 2004, **14**, 2059-2065.
2. *CRC Handbook of Chemistry and Physics*, 63rd edition, 1982, CRC Press, Florida.
3. *The QIAexpressionist: A handbook for high-level expression and purification of 6xHis-tagged proteins.* California: Qiagen, 2003.
4. Cras, J.J. et. al. *Biosensors & Bioelectronics,* 1999, **14**, 683-688.

Synthesis and Characterization of Efficient Two Photon Radical/Acid Generators

Charneal L. Dixon, Albany State University

Seth Marder, Takashi Okada, Georgia Institute of Technology

Introduction

The emergence of photonics as a multidisciplinary scientific field has received a considerable amount of attention from the scientific community in recent years. The development of two photon absorbing materials has been of particular interest to material chemists and optical physicists due to the recognized potential applications in three dimensional (3D) imaging, 3D microfabrication,

3D optical data storage and various biomedical applications.[i,ii,iii,4,5,6]

Two photon absorption (TPA) can be defined as the simultaneous absorption of two photons through virtual states in a medium to achieve an excited state that corresponds to the sum of the energy of the incident photons.[iv] (Figure 1) This process depends on both a spatial and temporal overlap of the incident photons and takes on a quadratic (non-linear) dependency on the incident intensity. As an advantage, two photon absorption is confined at the focus, where the intensity is highest, to a volume of order of ^{3} (where is the laser wavelength); any ensuing processes, such as fluorescence or photo-induced chemical reactions, are localized in this small volume.[v]

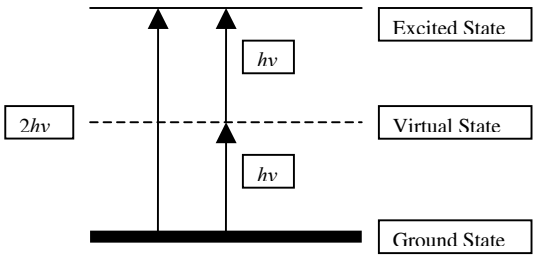

Figure 1. Energy Level Diagram of TPA

Two photon induced polymerization and lithography, as two of the promising applications for material micro-processing have

been reported using general UV photo-initiators or electron rich D- -D two photon absorbing dyes integrated with unsaturated resins to initiate polymerization.[vi] In both instances, either the two photon absorbance or the initiation efficiency has been low. Both of these observable traits could be improved ideally by finding a compound, which has both a large two photon absorbance and high initiation efficiency. In layman's terms, a photoactive group can be bound to the two photon absorbing dye, resulting in the production of an active species via an intra-molecular sensitization.

Since a nucleophilic secondary amine reacts easily with fluorotriphenyl sulfonium salt by nucleophilic displacement,[vii] it could serve in the efforts to build up a photo induced intra-molecular electron transfer radical initiator by simply choosing a suitable two photon absorbing dye as a donor.[viii] Marder and coworkers have shown from prior research that the electron rich symmetric D- -D molecules with di-alkyl amine as an electron donor on both ends have a large two photon absorption cross section. Based on the aforementioned, it is hypothesized that the photoactive tri-phenyl sulfonium group could be bound to this type of two photon dye using piperazine as a mutual link (Figure 2). Preliminary studies indicate that these compounds are better able to initiate the radical polymerization than the parent two photon dyes or the bimolecular systems of the parent two photon dyes with triphenyl sulfonium salts (TPS).[ix,10]

It should be duly noted that Marder and coworkers have already successfully synthesized a two photon acid generator using cyclic esters,

namely epoxides and oxetanes, as the monomeric units in 3D micro- fabrication. However, the advantage of this technology is that it can be extended to a wide variety of monomers. For the purpose of this research, vinyl monomeric units will be employed for 3D micro-fabrication.

A substituted bisstyrrylbenzene has been examined as both a monomolecular system and a bimolecular system (Figure 2). In previous experiments with the mono-molecular system, intra-molecular electron transfer from the excited dye to triphenylsulfonium salts (TPS) occurred with little difficulty. Conversely, the bimolecular system resulting from inter-molecular electron transfer did not.

Mono-Molecular System

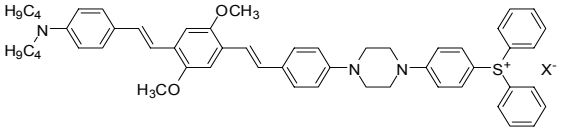

Bi-Molecular System

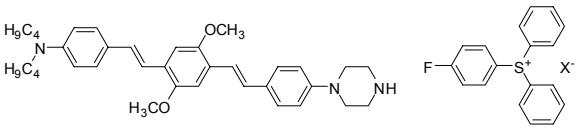

Figure 2. Prototype of Two Photon Generator

Results and Discussion

An electron rich dye and an electron deficient TPS were synthesized (Figure 3). Methods of characterization will include ^{1}H NMR, GCMS, absorption and emission spectroscopy, cyclic voltametry and photo-bleaching.

Electron Rich Dye

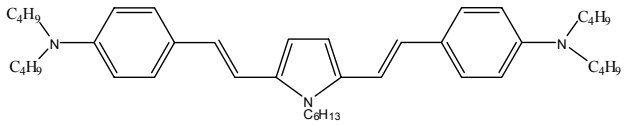

Electron Deficient TPS

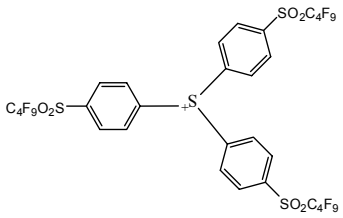

Mechanism

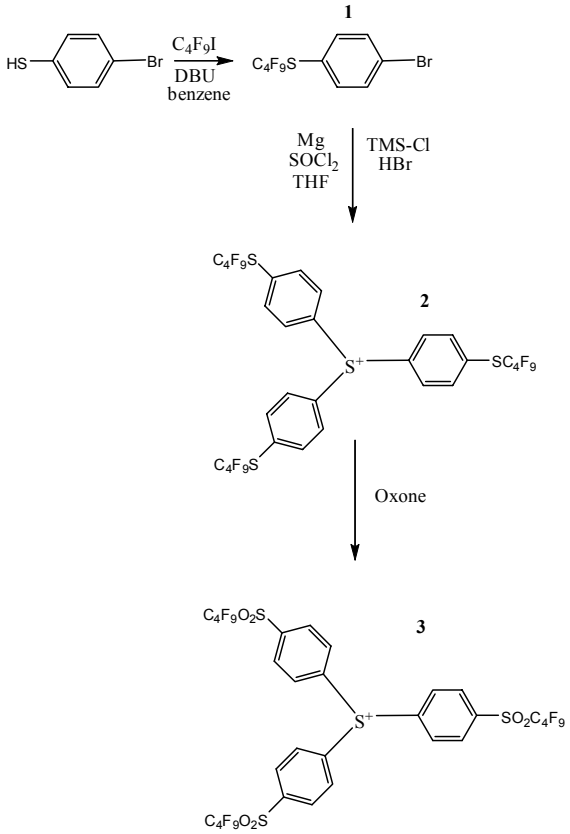

Figure 3. Synthetic Scheme of TPS

General Synthesis of Substituted Tri-Phenyl Sulfonium Salt

Sulfide **1** was prepared by mixing 4-bromothiophenol, 20mL of dry benzene and 2 equivalents of DBU under nitrogen. The mixture was cooled to 0° C, and twice the equimolar amount of nonafluorobutyl iodide was added. The reaction was stirred overnight at room temperature, added to water and extracted with $CHCl_3$. The organic extract was dried over $MgSO_4$, filtered and evaporated. The crude product was purified by flash chromatography.

A Grignard reagent was prepared from sulfide **1** and equimolar amounts of magnesium in dry THF. In a second and separate flask, dry THF, half and one-fifth the equimolar amount of TMSCl and $SOCl_2$ respectively, were added to a flask under nitrogen at 0° C. Sulfide **2** was prepared by transferring the Grignard reagent to the second flask using a cannula. The reaction was left overnight, added to HBr solution and extracted with ether.

The Sulfide **2** was converted to sulfone **3** by oxidation with oxone.

General Synthesis of a substituted bisstyrrylbenzene

Aldehyde **1** was prepared by mixing a solution of dibutylaniline in DMF with twice the equimolar amount of $POCl_3$ under nitrogen at 0° C. Mixture was stirred at 0° C for 1 hour, then warmed up to room temperature and stirred over night. The reaction mixture was poured into ice cold water and extracted with ether. Solvent was evaporated and the crude material was used without further purification.

Aldehyde **1** and reagent alcohol were charged in a round bottom flask and cooled to 0° C. $NaBH_4$ was slowly added to flask and stirred at room temperature for 5hrs. The solvent was evaporated and the crude material was poured into water, extracted with ethyl acetate, washed with water and dried with $NaSO_4$. The drying agent was removed by filtration and the solvent was evaporated at low pressure to get crude oil, alcohol **2**.

Phosphate **3** was synthesized by adding tri-ethyl phosphite and alcohol **1** to a flask that was cooled to 0° C. Iodine was slowly and the mixture was stirred. The mixture was distilled to remove excess tri-phenyl phosphite.

Aldehyde **4** was prepared from a mixture of

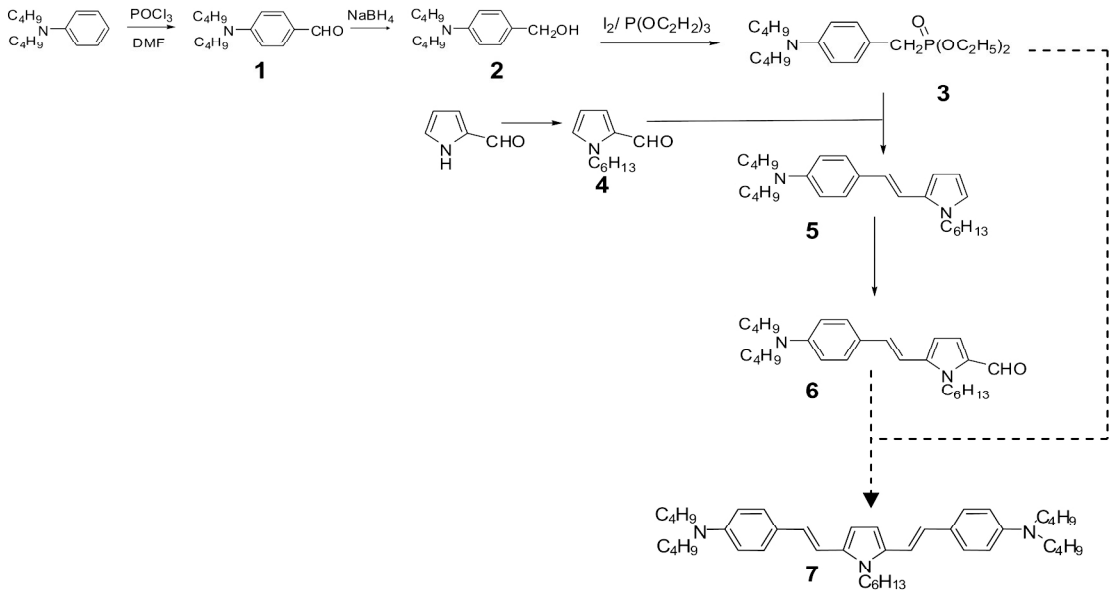

Figure 4. Synthetic Scheme of Electron Rich Dye

NaH and DMF and pyrrole-2-carboxaldehyde under nitrogen. The suspension was stirred at 0° C. A solution of nhexylbromide in DMF was added under nitrogen at 0° C; gas evolved. The reaction was stirred at room temperature for 3 days.

5 was prepared by charging aldehyde **4**, phosphonate **3** and THF in a flask under nitrogen. t-BuOK was added dropwise under nitrogen at 0° C for 1hr. The reaction was stirred overnight at ambient temperature.

Aldehyde **6** was synthesized by mixing a solution of **5** in DMF with an equimolar amount of $POCl_3$ under nitrogen at 0° C. Mixture was stirred at 0° C for 1 hour, then warmed up to room temperature and stirred over night. The reaction mixture was poured into ice cold water and extracted with ether. Solvent was evaporated and the crude material was purified using flash chromatography.

Conclusion

Several intermediates essential for the synthesis of the substituted bisstyrrylbenzene and tri-phenyl sulfonium salt have been synthesized, all of which have been characterized using ^{1}H NMR and GCMS. Synthesis of the target molecules is now underway; they will be characterized using ^{1}H NMR, ^{12}C NMR, elemental analysis, GCMS, absorption and emission spectroscopy, cyclic voltametry and photo-bleaching. The efficiency of this radical/acid generator will be evaluated comparatively with previously synthesized radical/acid generators.

References

[i] Cumpston, B. H.; Ananthavel, S. P.: Barlow, S.; Dyer, D.; Elrich, J.E.; Erskine, L.L.; Heikel, A.A.; Kuebler, S.M.; Lee, I.Y.S.; McCord-Maughon, D.; Qin, J.; Rockel, H.; Rumi, Wu, L; Marder, S.R.; Perry, J.W. ***Nature*** 1999, 398, 51

[ii] Mukherjee, A. ***Appl. Phys. Lett***. 1993, 62, 3423

[iii] He, G. S.; Xu, G.C.; Prasad, P.N.; Reinhardt, B. A.; Bhatt, J.C; Dillard, A.G. ***Opt. Lett***. 1995, 20, 435

[iv] Stiel, H.; Teuchner, K.; Paul, A.; Freyer, W.; Leupold, D. J. ***Photochem. Photobiol***. A: Chem.1994, 80, 289

[v] Denk, W.; Striker, J. H.: Webb, W.W. Science, 1990, 248, 73

[vi] Gura, T. ***Science***, 1997, 276, 1988

[vii] Albota, M.; Bejonne, D.; Brendas, J.-L.; Ehrlich, J.E.; Fu, J.-Y.; Heikal, A. A.; Hess, S. E.; Kogej, T.; Levin, M.D.; Marder, S.R.; McCord-Maughon, D.; Perry, J. W.; Rockel, H.; Rumi, M.; Subramanian, G.; Webb, W.; Wu, X-L.; Xu, C. ***Science*** 1998, 281, 1653

[viii] Toba, Y.; Usui, Y.; Konishi, T.; Ito, O.; Uesugi, T. ***Macromolecules*** 1999, 32, 6545.

[ix] Papps, S.P.; Pappas, B. C.; Gatechair, J. H. Jilek, Schnabel, W. ***Polym. Photochem***. 1984, 5, 1.

[10] Crivello, J. V.; Sangermano, M. J. ***Polym Chem***. 2001, 39, 343.

Acknowledgements

Center of Materials and Devices fro Information Technology Research (CMDITR)

NSF Science and technology Center, No. DMR 0120967

Special Thanks to Dr. Seth Marder (PI), Dr. Takashi Okada (mentor), and the Marder Group, for there support and encouragement in addition to hosting me for my first undergraduate research experience.

Charneal Dixon is presently majoring in Chemistry at Albany State University and intend on matriculating into an MD/PHD program upon graduating in 2008.

Development of Reliable Synthetic Methods for Asymmetric Di-Functionalization of Benzo[2,1,3]thiadiazole

Daniel L. Dodge, Eastern Washington University

Dr. Philip Sullivan, Dr. Larry Dalton, University of Washington

Introduction

In the last several years the importance of donor-bridge-acceptor chromophores in electro-optical systems has been important to scientists in several areas of focus. The photo-physical and electrochemical properties of these molecules have sparked interest in fields like telecommunications and computer technology. These systems have many implications in other areas where the advancement of technologies for creating electrical to optical signal transmission is a key factor. In areas like computing technology, the use of metal (dominantly copper) chips is the limiting factor of how fast information can be transferred. The use of electro-optical systems will be able to greatly enhance the speed at which information is sent and transferred.

The advancement of the efficiency of the chromophore is a very important aspect in realizing the potential of these electro-optical systems. Nonlinear optical chromophores are made of organic compounds with the donor-bridge-acceptor molecular architecture. This architecture creates a dipolar compound and if that compound has a high molecular hyperpolarizability, β, it will serve well as a chromophore. A high β value is realized when the chromophore allows for an efficient transfer of electron density from the donor to the acceptor. Another important value is the electro-optic coefficient known as $\mathbf{r_{33}}$, which is related to how well the molecules hyperpolarize when number density is high. $\mathbf{r_{33}}$ can be expressed by the following equation:

$$r_{33} = \langle\cos^3\theta\rangle N\beta \qquad \text{(Equation 1)}$$

In Equation 1, N is the number density, β is the first molecular hyperpolarizability, and $\langle\cos^3\theta\rangle$ is the order parameter in which θ is denoted as the angle between the dipole vector of chromophore and the poling axis.

The focus of this research was on the incorporation of the electron deficient molecule 2,1,3 benzothiadiazole into the bridge architecture of a chromophore. Traditionally chromophore bridges have been viewed as "inert conduits" that simply connect the donor and the acceptor via a π-conjugated system (See Figure 1.)[13] This bridge does not play a part in donating or accepting electrons, it only separates the donor and acceptor to create the desired electron asymmetry, while allowing electrons to easily "flow" throughout the conjugated system.

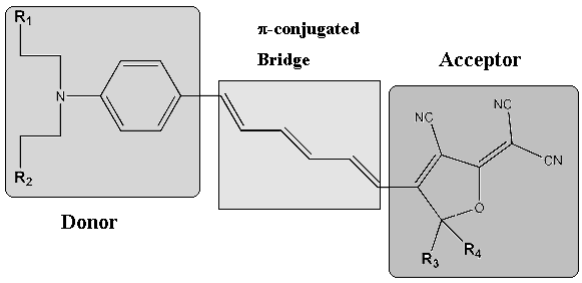

Figure 1: Simple donor-bridge-acceptor type chromophore with "inert conduit" •-conjugated bridge.

However by incorporating chromophore components that are electron deficient and electron rich into the bridge it will essentially create an "active bridge" (See Figure 2.)[13] When an electron deficient bridge component is placed next to the acceptor in a chromphore along with an electron rich bridge component next to the donor it creates a "Super Donor" and a "Super Acceptor." This helps to spatially localize the HOMO and LUMO to increase the ground state and transitional dipole moment. This localization allows a gradual change in the HOMO and LUMO stabilities rather than two steps between the donor and the bridge and then the bridge and the acceptor. This architecture increases the hyperpolarizabilty of the chromophore as well as decreases the bandgap.

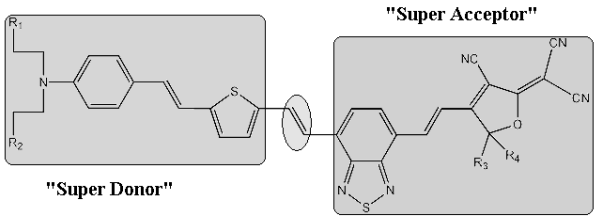

Figure 2: An example of a chromophore with an active bridge and a "Super Donor" and "Super Acceptor."

Results and Discussion

The major goal of this project was to incorporate benzo[2,1,3]thiadiazole into a donor–bridge-acceptor type chromophore. In order to achieve this the starting compound, benzo[2,1,3]thiadiazole, must be converted into a species capable of undergoing coupling reactions with the donor and/or acceptor. A typical and seemingly straight forward approach was to formylate one side of the compound prior to coupling, or after a donor/acceptor had been coupled to the other side. While many literature reactions showed the formylation of aromatic rings to be simple and give good yields, this was not so with benzo[2,1,3]thiadiazole. The first few reactions carried out focused on brominating benzo[2,1,3]thiadiazole **(1)** and the methylated version 4-methyl-benzo[2,1,3]thiadiazole**(3)** (See Scheme 1.) **1** and **3** were reacted with Br_2 in HBr to get **2** and **4** respectively.[1]

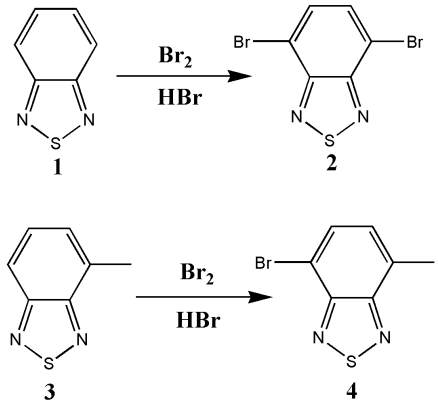

Scheme 1. Bromination of **1** and **2** with Br_2 and HBr.

Following the successful production of **2** in good yield, a series of reactions followed that attempted to mono-formylate one side of **2**. The desired product is shown below as **5** (See Scheme 2.)

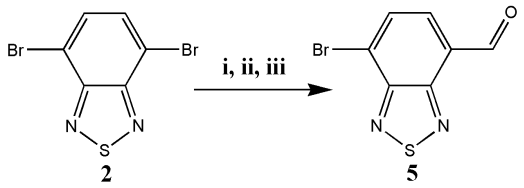

Scheme 2: **(i)** R: n-BuLi, DMF, S: diethyl ether at -78° C; **(ii)** R: t-BuLi, DMF, S: diethyl ether at -78° C; **(iii)** R: t-BuLi, DMF, S: THF ad -78° C.

All the attempted reactions failed to yield any aldehyde. Reaction **i** showed several spots on Thin Layer Chromatography (TLC) plates and none were consistent with an aldehyde. Reaction **ii** produced some minor impurity but the majority of **2** did not undergo any reaction, thus **ii** yielded primarily the reactant, **2**. Reaction **ii** also showed no spots consistent with aldehyde on TLC plate. Since **ii** did not produce multiple impurities, **iii**[2] was tried with a different solvent, THF, but again the reaction did not yield aldehyde, which was proven by dinitro-phenyl hydrazine (DNPH) dipping and no aldehyde peak on ^{1}H NMR.

After the failure of the formylation via lithium reagents a new approach involved attempting a direct mono-formylation of **1** to give **6** (See Scheme 3.)

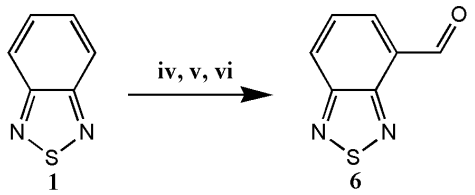

Scheme 3: (iv) R:Cl_2CHOCH_3, $TiCl_4$, S: DCM at -30°C; **(v)** R: LDA, DMF S: THF at –78°C; **(vi)** R: $POCl_3$, DMF S: CH_3CN at 0°C, then later heated to 90-100°C.

Reaction **iv** was carried out the reagents dichloromethyl methyl ether and titanium tetrachloride.[3,4] Again DNPH dipping showed no production of aldehyde. Reaction **v** was carried out with two different forms of lithium diisopropylamine (LDA), once with stock LDA and once with distilled diisopropylaime dissolved in n-butyl lithium to give a purer form of LDA than was obtained from the stock bottle.[5] Again these reactions showed no aldehyde when dipped into DNPH. The final attempt to directly formylate **1** was done using a typical Vilsmier type reaction (**vi**) which was carried out at 0°C and then was refluxed at 90 to 100°C.[6] Early in the reaction samples of solution dipped in DNPH

showed a small red dot which indicated aldehyde, but after further heating there was no longer any spot when dipped in DNPH.

The failure to find an easy synthetic approach for the formylation of benzo[2,1,3]thiadiazole using conventional literature reactions suggests that the molecule is extremely sensitive and it's properties inhibit the ability to successfully carry out a formyl substitution reaction.

Due to the apparent sensitivity of **1,** yet another approach was investigated which involved compound **4**. The first step was to radically brominate the methyl group on **4** using n-bromomsuccinamide in carbon tetrachloride (See Scheme 4.)

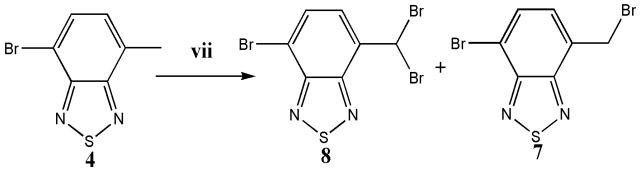

Scheme 4: Radical bromination of **4** using NBS in CCl_4. Reaction **vii** produced a mixture of the major product **8** along with the minor product **7**.

The literature reaction was followed exactly on a 10% scale.[7] While the reaction literature claimed a yield of 97% mono-bromination by radical mechanism (compound **7**), such results could not be reproduced although the reaction was ran multiple times following the literature experimental. The products yielded by reaction **vii** were determined to be a mixture of mono- and di-brominated methyl groups. Thus the products of the reaction were **7** and **8**, with the majority of the product being **8**. Products were confirmed using ^{1}H-NMR.

The mixture of **7** and **8** were extremely difficult to separate using silica gel column chromatography. Therefore, following reactions were executed using the crude product from reaction **vii**.

The conversion of a radically brominated methyl group into a formyl group was documented for both mono- and di-brominated methyl groups. However an ideal reaction for the crude product of **7** and **8** was one that had potential to convert both the mono- and di-brominated products into aldehydes during the same reaction (See Scheme 5.)

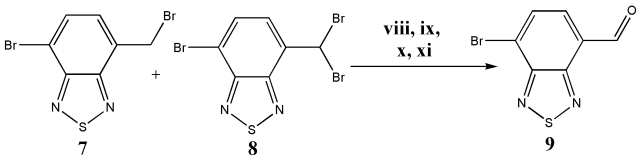

Scheme 5: Attempted formylation reactions with crude of **7** and **8**. **(viii)** R: dimethyl sulfoxide
S: dimethyl sulfoxide at 100°C **(ix)** R: $AgNO_3$
S: Ethanol (or aceonitrile) at 90°C
(x) R: diethylamine S: diethylamine at 60°C
(xi) R: formic acid S: water at 110°C

Reactions **viii** through **xi** all produced some kind of aldehdye. Reaction **viii** was carried out with dry dimethyl sulfoxide as well as deuterated dimethyl sulfoxide.[10] Both reactions yielded aldehdye. Small scale (approximately 50 mg of reactant) reactions yielded proton NMR peaks that were consistent with what was believed to be the spectra of the desired product. However larger scale reactions (500 mg to 1 g) showed proton NMR with peaks different than that of the small scale reactions, thus making it inconsistent with the believed product spectra. After reactions **ix** through **xi** were carried out it seemed that the proton NMR spectra for all large scale reactions were the same, leading to the assumption that the spectra obtained were indeed that of the desired product, although they were different than what was anticipated.

Reaction **ix** was carried with ethanol as solvent as well as with acetonitrile.[8] Both reactions seemed to be very contaminated, and reliable NMR spectrums could not be obtained. Reaction **x**[9] was simple and gave a fairly clean NMR, however at the time it was still believed that the spectra was incorrect so the final reaction (**xi**) was attempted. Reaction **xi**[11] was successful, and since a crude product of **7** and **8** an accurate yield could not be determined, however an overall yield from **4** to **9** could be determined, which turned out to be approximately 32%.

Following the successful formylation a "Heck" reaction was carried to connect a donor amine to **9** (See Scheme 6.) Reaction **xii** was carried out with in triethylamine and dimethyl formamide with the aid of a palladium and copper catalysts (See Scheme 6.)[12]

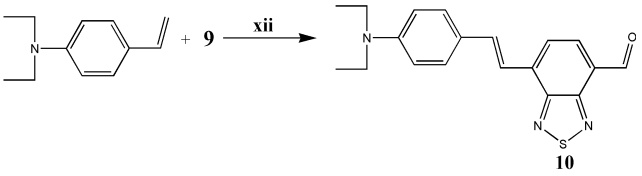

Scheme 6: Reaction of amine donor with **9** to create a donor-bridge product with an aldehyde group to allow for further reaction with an acceptor.

After initial purification, reaction **xii** yielded roughly 52% pure product. However, there was approximately another 15 to 20% of impure product that was suitable to be purified again.

Conclusions

Currently work is in progress to couple **10** to an acceptor. Results for this reaction are not available at this time.

From these reactions it can be determined that the benzothiadiazole molecule is extremely sensitive and very resistant to typical formylation procedures. Therefore the indirect formylation procedure via radical bromination, followed by the reactions previously discussed in Scheme 5, seems to be a reliable synthetic route to achieve the asymmetric di-functionalization of benzo[2,1,3]thiadiazole. To date, this type of di-functionalization has proven itself practical, because it easily reacted with the donor to form the desired donor-bridge-aldehyde (**10.**)

References

1. Da Silveria Neto, Brenno A.; *et al*. *Tetrahedron*. **2005**, *61*, 10975-10982.

2. Rumi, M.; Ehrlich, J.E. et al. *J. Am. Chem. Soc.* **2000,** *122*, 9500-9510.

3. Cheng, Z.; Harper, A.W.; Dalton, L.R. *Syn. Commun.* **2001,** *31(9),* 1361-13665.

4. Tatchell, A.R. *Vogel's Textbook of Practical Organic Chemistry,* 5th Ed., John Wiley and Sons: New York, **1989**, 997.

5. **Patentschrift (Switz.)**, 661270, 15 Jul 1987.

6. Beverina, L.; Fu, J. et al. *J. Am. Chem. Soc.* **2005**, *127*, 7282-7283.

7. Jørgensen, M.; Krebs, F.C. *J. Org. Chem.* **2005**, *70*, 6004-6017.

8. Harvey, R.G.; Dai, Q.; Ran, C.; Penning, T.M. *J. Org. Chem*. **2004**. *69*, 2024-2032.

9. Bankston, D. *Synthesis*, **2004**, *2*, 0283-0289.

10. Li, W.; Li, J.; DeVincentis, D.; Mansour, T.S. *Tetrahedron Letters*. **2004**,*45*, 1071-1074.

11. Vanelle, P.; Liegeois, C.T.; Meuche, J.; Maldonado, J.; Crozet, M.P. *Heterocycles*. **1997**, *45(5)*, 955-962.

12. Negishi, E., Ma, S.; Sugihara, T.; Noda, Y. *J. Org. Chem.,* **1997***, 62*, 1922-1923.

13. Sullivan, Phillip A. "Theory Guided Design and Molecular Engineering of Organic Materials for Enhanced Second-Order Nonlinear Optical Properties" Ph.D. Diss, University of Washington, **2006**.

Acknowledgments

Funds for this research were provided by the Center on Materials and Devices for Information Technology Research (CMDITR), and the NSF Science and Technology Center No. DMR 0120967.

The scientific guidance and assistance of the following people are gratefully acknowledged: Dr. Larry Dalton, Dr. Phillip Sullivan, Dr. Samy Elangovan, Joshua Davies, Tiffany Mealman, David Lao, and the rest of the Dalton Group members.

Personal Statement:

After finishing my undergraduate degree at Eastern Washington University, I hope to attend a graduate school or medical school. I would like to eventually conduct clinical research and aid in the development of new medicines.

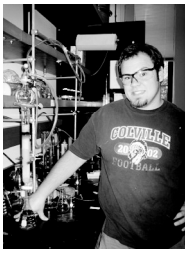

Investigating Carbon Nanotubes for Potential Electrode Applications

Patrick Duggan, Providence College

Roderick Jackson, Samuel Graham, Georgia Institute of Technology

Introduction

Recently there has been interest in the production of thin carbon nanotubes (CNT) films as potential electrode materials because of their flexibility, transparency, electrical conductivity, and large surface area for charge collection or injection into organic semiconductors.[1] There is hope that CNTs can replace indium tin oxide (ITO) as the anode in organic light emitting diodes (OLED, Fig. 1) and organic photovoltaic devices (OPV).[2] With the potential to functionalize and create soluble suspension, the potential to ink jet or screen print CNT electrodes may also become a reality.

Since the work function of CNTs is similar to ITO, charge injection and collection at these electrodes may have a similar performance as ITO. The benefits of moving to a flexible CNT platform over ITO lies in it damage tolerance which is necessary for flexible applications. Brittle materials like ITO are prone to developing cracks which degrade their electrical performance. However, random networks of CNTs form complex percolation networks with thousands of redundant interconnecting points. Thus, deformation of the network does little to alter the conduction characteristics, leading to relative insensitivity in flexible applications.

The overall electrical resistivity of CNT networks, however; has yet to show performance which is comparable to ITO. Thus, further studies are needed to investigate CNT networks on polymer substrates and how to improve their optical and electrical characteristics to become a viable ITO

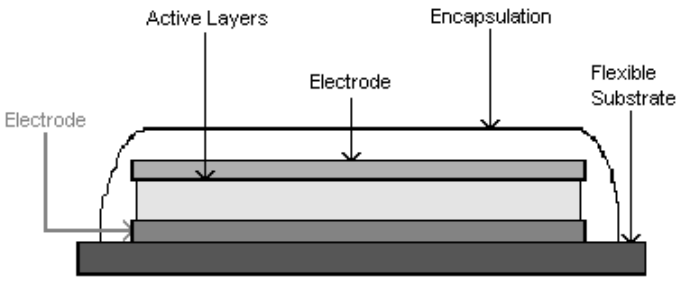

Figure 1. Basic diagram of an OLED

A CNT film capable of replacing ITO needs low resistivity, high transparency and low surface roughness. Low resistivity allow for efficient current injection and collection over large areas while minimizing voltage drops. High transparency will allow maximum light emission for bottom emitting OLEDS as well as light penetration for photovoltaics. Thin layers of CNTs are desired to minimize bending of flexible substrates upon changes in temperature. In general, CNT networks can have negative coefficients of thermal expansion which may alter the curvature of the flexible OLEDs or OPVs during operation. Surface roughness of the CNT electrodes must also be reduced to eliminate pin holes and electrical shorting in the thin film active layers which are deposited. The main issue with the development of high quality CNT electrodes is that the problems mentioned are coupled to each other. While a thinner film creates better transparency and limits bending due to CTE mismatches, they also result in more resistive electrodes.[3] Optimization is necessary to find the most advantageous use of CNT.

Objective

The objective of this work is to investigate the process of suspending single wall carbon nanotubes in solvent solutions followed by the creation of thin transparent electrodes on PET films. These nanotubes will be used as received (not purified or doped). While not expected to yield the best electrical characteristics, these as received nanotubes will allow the determination of the effects of solvent and various processing steps on reducing the electrical resistance of the thin nanotube networks. Properties such as transparency between 0.4-3 μm and room temperature sheet resistance will be studied.

Process

Step 1: Creating the CNT solution

Approximately 2 mg of commercially available single-walled carbon nanotubes (SWCNT) are mixed into 100 mL of dimethyl formamide (DMF). The mixture was bath-sonicated for 48 hours to aid in the dispersion of the nanotubes. Drops of the solution are mixed into water being stirred at 500 rpm on a stirring hotplate. This is necessary to prevent the CNTs from forming large agglomerates. Carbon nanotubes bundles create a film with high resistance and poor conductivity, so care must be taken to promote dispersion during processing.

Step 2: Depositing the solution onto the substrate

The solution is poured into a vacuum filtration system that deposits the nanotubes onto a Millipore hydrophobic filter. It is essential that the filter, vacuum filtration system and mixture are clean because any additional particles will end up on the film. Vacuum filtration is used since it provides and easy pathway of generating a uniform film of carbon nanotubes from the dispersed solution. The filter is used as an intermediate substrate which must be transferred to a clean polyethylene terephthalate (PET) film. The PET is cleaned using a series of chemicals: acetone, methanol, isopropanol (IPA) and DI water. After cleaning the plastic substrate, it is dried and gently placed on top of the nanotubes/filter substrate. Since the CNTs are not robustly attached to the filter, care must be taken during the placement of the PET substrate to avoid shearing of the CNT pattern.

Step 3: Removing the Filter

A beaker containing a small amount of acetone is heated as the filter and substrate are suspended over the top. The evaporated acetone vapor dissolves the filter. Special attention must used in this step. If the acetone is heated for too long, bubbles will form on the surface of the film. The bubbles can displace the CNT. Once the filter covering the CNT evaporates, the sample is laid out to dry. Since some of the filter remains on the substrate, a beaker is placed over the top of it. The beaker prevents the plastic substrate from curling. When dry, the film is placed in an acetone bath to remove the remnants of the filter. The same procedure to clean the substrate is used again to clean the surface of the film. The result is complete transfer of the CNT pattern from the Millipore filter to the PET substrate.

Step 4: Testing

The electrical resistivity of the samples was measured using a four point probe method (Figs. 2 and 3) while the surface roughness was determined using profilometry. Sample transparency was determined using a UV-Vis Spectrophotometer.

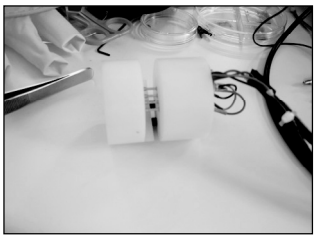

Figure 2. Four-Point Probe

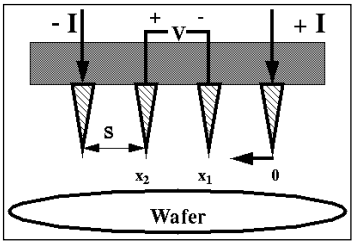

Figure 3. Probe Diagram

Thin Film Production Analysis

While the thin films of SWCNT are not mechanically robust, degradation does not occur if handled appropriately. Instead, problems with the films generally occur during the processing steps. Problems in producing SWCNT films are mainly associated with film homogeneity. The film's conductivity relies on the redundant interconnections of the CNT network. Therefore, an inconsistent layer of nanotubes can create deficient conduction. There are several key steps in the creation of the SWCNT. The first crucial step is the creation of a dispersed solution. Since nanotubes are hydrophobic, if not dispersed well they tend to agglomerate (Fig. 4-C&D). A reduction in nanotube bundles may be realized through the use of a centrifuge, which is common in processing CNT films. Our group has yet to incorporate the centrifuge, but there is hope that it will remove agglomerates and improve film consistency.

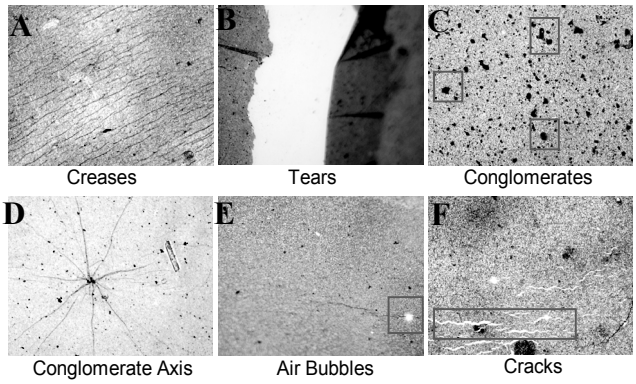

Another important step is when the SWCNT are transferred to the PET substrate (Fig. 5). Transferring the SWCNT to the PET is most effective when just freshly deposited. However, the nanotubes are also most vulnerable at this stage. Cracks and creases (Fig. 4-A&F) occur when manually placing the substrate on top of the deposited nanotubes. If the transfer is done correctly, the SWCNT will not be displaced and the sheet resistance should remain the same. In Figure 6, there is a significant difference in SWCNT sheet resistance before and after the transfer (diluted in DI water and on PET, respectively). These results suggest that there is still improvement to be made in transferring the SWCNT. The last critical step is the removal of the filter. If the acetone evaporates over the filter for too long air bubbles can infiltrate the nanotube network (Fig. 4-E). To completely remove the filter, the film is placed in an acetone bath. Despite an extended drying period, the SWCNT are still not mechanically robust. The film must be gently placed in the bath or it will tear (Fig. 4-B).

Variable Quantity Analysis

The first step in optimizing the properties of thin film carbon nanotubes is to determine the effects when varying the quantity of carbon nanotubes. Increasing the SWCNT amount will decrease the transparency. The volume deposited upon each filter is varied. The solution composition is not augmented because of the difficulty in measuring the mass of the SWCNT within 1 mg. The simplest way to vary the deposited volume was through pipettes of the solution (1 pipette ~ 1.5 mL, 1.5 mL ~ 0.03 mg of SWCNT).

Methods of Dilution

In our original process, the SWCNT:DMF solution was diluted before deposition in 40 mL of DI water. Although SWCNT are hydrophobic, a fairly consistent dispersion was realized. DI water was used because it is easier to filter and remove from the nanotubes. Since our SWCNT:DMF solution has a high concentration of nanotubes (2 mg in 100 mL of DMF), 40 mL would render the film opaque. However, a problem arises when the solution used does not mix well with DI water. This happened when attempting to use a SWCNT:nitromethane solution. Instead of diluting with DI water, our

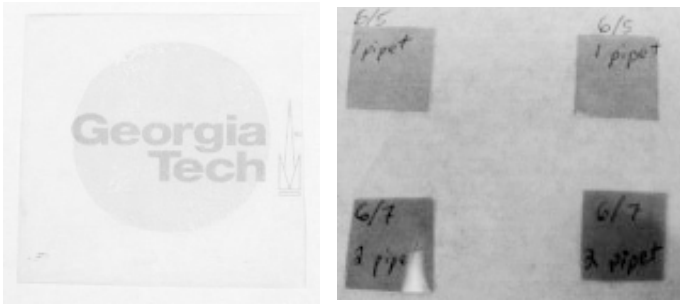

Figure 5. Final SWCNT films on PET

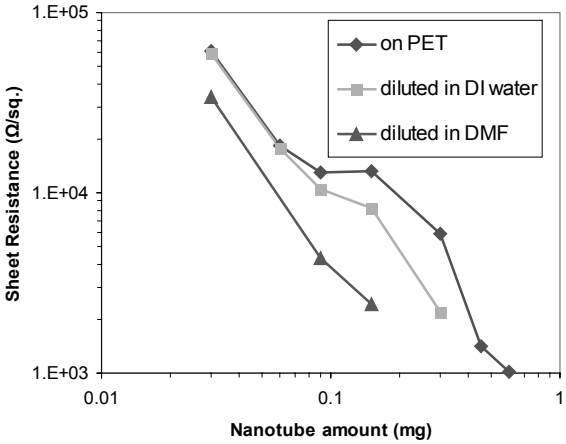

Figure 6. Dilution results with DMF

group found that diluting with nitromethane worked the best. To compare processing procedures, a SWCNT:DMF solution was diluted in DMF. The goal was to find out if DI water impacted the dispersion of the SWCNT. In Figure 6, the data shows that a SWCNT:DMF solution creates better dispersion if diluted in DMF. It is evident that DI water decreases the dispersion of the SWCNT. Presumably, a solution diluted in itself disperses better than with other solvents. But, it may only be true with DI water since SWCNT are hydrophobic. In the future, the dilution step may be eliminated if less concentrated solutions are prepared. Otherwise, a centrifuge step may be helpful in removing bundles which are difficult to disperse.

DMF vs. Nitromethane

Since properties of the SWCNT film relies on its consistency, there is significance in the solubility of the solution. Better dispersion will result in an even SWCNT coating and therefore better percolation between nanotubes. A solution's total CNT solubility depends on three parameters: dispersion, polarity, and hydrogen bonding. DMF has a high dispersion factor, but it was determined that nitromethane has greater overall solubility[4] (Fig. 7). A SWCNT and nitromethane solution was created and tested.

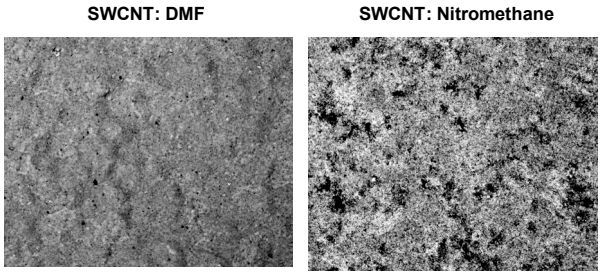

Figure 7. Dispersion of CNT in solvent

Creating SWCNT films from a nitromethane solution is not the same as with DMF. As previously mentioned, nitromethane does not dilute well in DI water. Nitromethane must be diluted in itself before it is deposited onto the filter. Alumina filters instead of Millipore membrane filters must also be used. However, a reliable transfer method has yet to be realized with alumina filters and SWCNT. Our suggestion is to use transfer printing techniques such as PDMS stamps or microwave transfer which was recently developed our research group. In Figure 8, it is evident that nitromethane allows for higher conductivity in the SWCNT network. The lowest sheet resistance is found to be at 157 (/sq.).

Augmentation of Sampling

An attempt was made to improve the properties of the SWCNT thin films, augmentation to the samples are made. The augmentations are made based upon the characteristics of the SWCNT and each sample.

Sample Heating

Heat is used to evaporate away the remnants of the solution from the deposition. If DMF or nitromethane is left on the film, it may decrease the conductivity of the film by impeding the electrical network.

Heating the films proved to be a successful augmentation as it decreased the sheet resistance in every sample (Fig. 9). However, the DMF samples decreased more nitromethane samples. In other words, more DMF was left on the thin films than nitromethane. Nitromethane is much more reactive and unstable than DMF so it is believed that much of it had already evaporated. More tests need to be done in order to optimize this augmentation. A longer, hotter process may induce further evaporation as long as there is no degradation to the PET substrate.

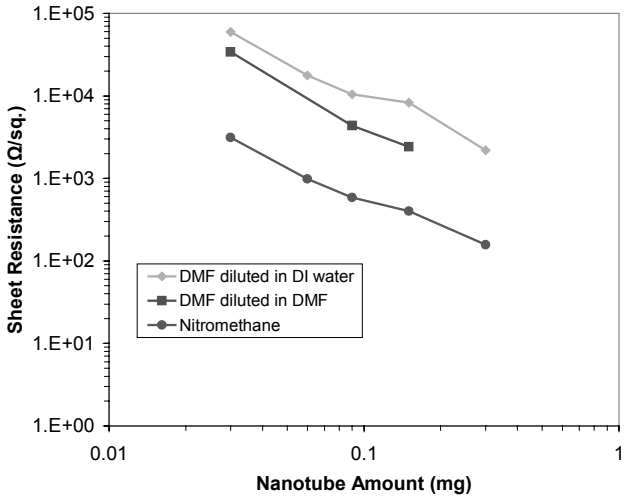

Figure 8. Impact on resistance from solvents

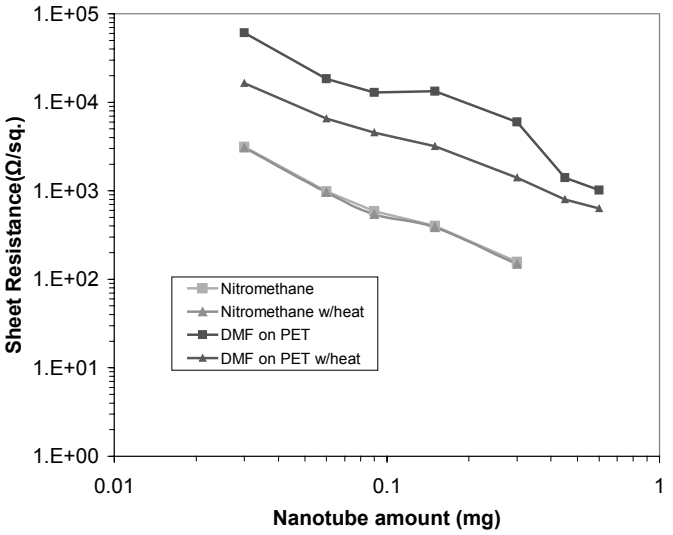

Figure 9. Impact on resistance from heat

Silver Layer

To increase the conductivity of the SWCNT films a layer of silver (3-5 nm) was deposited onto the samples. The silver was added using an e-beam deposition. Silver would fill in pin holes of the nanotubes network and could even weld the nanotube junctions together. A conductive junction between nanotubes would decrease the energy gap as well as the resistance. Additional tests need to be done to see if varying amounts of silver impact resistance. Silver could also be combined with SWCNT in a multi-layer format. Although, adding too much silver would allow electrons to travel solely through the silver layer and render the SWCNT layer useless.

In general, the layer added to the DMF decreased resistance while the layer added to the nitromethane increased it. However, it is believed that the silver layer did not increase the resistance of the film. It is likely that the resistance increase was due to the degradation of the samples. Several tests and experiments were done using the same samples (Figs. 10, 11 and 12). The spectrophotometer and e-beam deposition even require the samples be fastened to a surface.

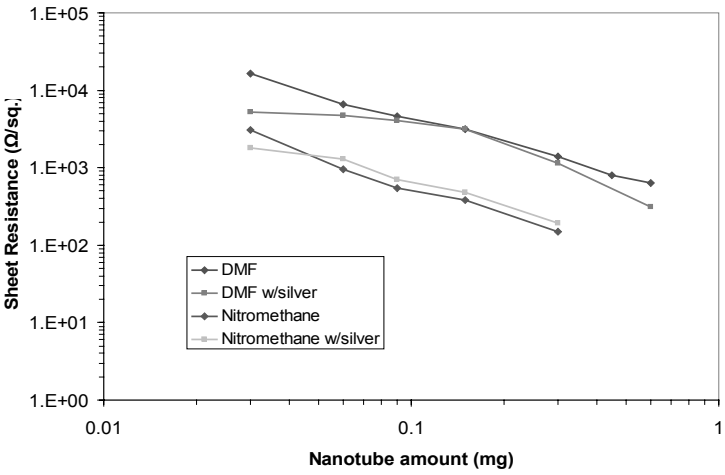

Figure 10. Impact on resistance from silver

Entrenched Technology Comparison

The current entrenched technology for producing electrodes in OLEDs and PVs is indium tin oxide. Indium tin oxide is an extremely conductive and transparent material, but brittle and expensive. Currently, ITO has a sheet resistance of about 10 /sq. In the visible spectrum, the light transmittance ranges from 48.0-83.1 % on PET.

A major challenge with using SWCNT is that volume per square impacts both resistance and transmittance of the film. Unfortunately, the relationship between the two parameters is inversely proportional. As the SWCNT films approach the sheet resistance of ITO, the transparency significantly drops.

In the middle of the infrared spectrum (1000 nm) the transmittance of ITO is less than 40 % on PET. Some of the samples have better transmission than ITO, but the sheet resistance is still too high.

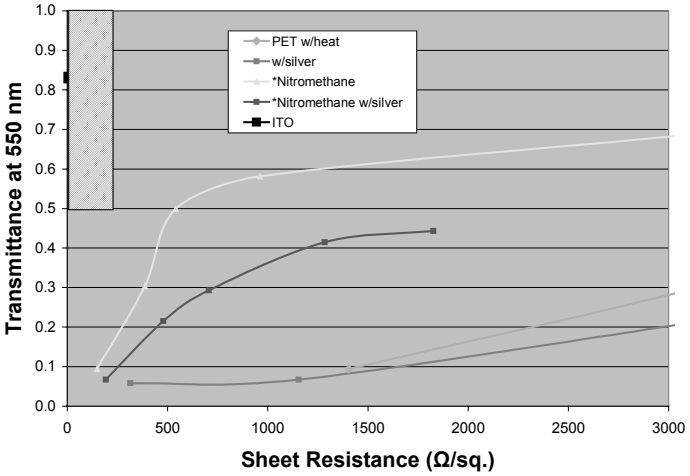

Figure 11. Comparison to ITO in visible spectrum

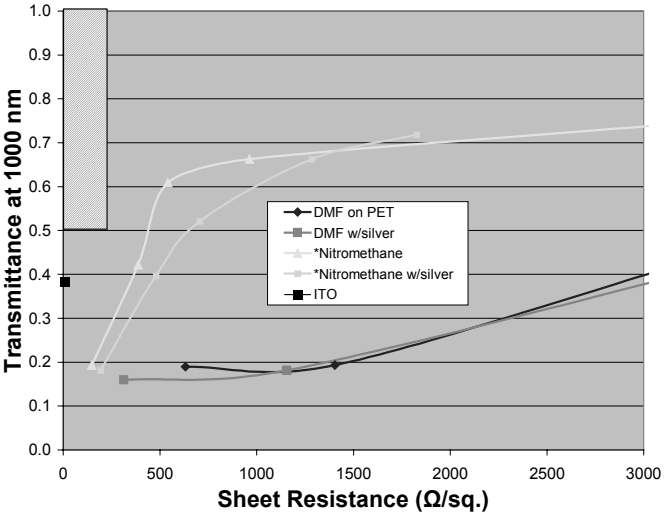

Figure 12. Comparison to ITO in IR spectrum

With the current results, there is potential use for CNT as top emitting OLEDs where the electrode can be opaque. The problem with this is that CNT will have to compete with highly conductive metals. There is also potential use for electronics that work in the IR regime.

Recommendations for Future Research

Since significant progress was made using nitromethane, additional solvents should be tested. Another solvent might do a better job at dispersing the nanotubes. Also, if the solution is sonicated for a shorter amount of time, the CNT will be longer and more conductive. Although this may create more agglomerates, these can be removed using a centrifuge. Other ideas which must be pursued include the purification and doping of the carbon nanotubes. It is believed that this will give sheet resistances in the 300 Ω/sq. range or lower. Also, improved sheet resistance should also consider the use of water-based surfactant suspensions.[5]

References

[1] Y. Zhou, L. Hu, and G. Gruner, A method of printing carbon nanotubes thin films. 1, (2006)

[2] A.D. Pasquier, H.E. Unalan, A. Kanwal, S. Miller and M. Chhowalla, Conducting and transparent single-wall carbon nanotube electrodes for polymer-fullerene solar cells. 1, (2005)

[3] M. Kaempgen, G.S. Duesberg, S. Roth, Transparent carbon nanotubes coatings. 2, (2005)

[4] Jing Liu, Tao Liu, Satish Kumar, Effect of solvent solubility parameter on SWNT dispersion in PMMA. 2, (2005)

[5] Andrew Rinzler, Transparent, Conductive Carbon Nanotube Films. 1-2, (2004)

Acknowledgments

Funds for this research were provided by the Center on Materials and Devices for Information Technology Research (CMDITR), and the NSF Science and Technology Center No. DMR 0120967. Special Thanks to: Dr. Samuel Graham, Roderick Jackson, Nam Su Kim, Entire Graham Research Group, William Potscavage and Kippelen Group, Olanda Bryant and Dr. Keith Oden.

My name is Patrick Duggan and I am an engineering student at Providence College. I love doing research and plan on going to graduate school in hopes of receiving a PhD.

Conductivity of Sol-Gel Polymer Waveguide Cladding Doped with Carbon Nanotubes

Brandon T. Fetroe, Walla Walla College

James Westphal, Nishant Bhatambrekar, Antao Chen, University of Washington

Introduction

In the past few decades, fiber optics, lasers and other optical devices have been used to expediently transport large amounts of information over long distances. Typically, optical networks convert electrical signals into optical signals in the form of pulses of light. Since there are limitations to the speed at which lasers can be turned on and off, a device called a modulator is needed to segment continuous laser light into optical pulses.

Most modulators are interferometers. An interferometer is a photonic waveguide device that consists of an active layer surrounded by two low-index cladding layers. Incoming light is coupled into the active layer, separated into two different paths, called arms, and then recombined at the other end. Usually the difference in optical path length is created by incorporating an electro-optic (EO) material into the active layer. EO materials change their index of refraction when subjected to an external electric field. In this way, light traveling through the EO material will travel faster or slower depending on the applied electric field, which results in constructive or destructive interference and causes the aforementioned pulsing.

While most commercial modulators currently incorporate inorganic materials such as lithium niobate, organic materials have several advantages including higher operating frequencies and decreased cost. Therefore, organic polymer waveguides are currently being developed for use in modulators with operational frequencies greater than 100 GHz.[1]

After initial fabrication, the organic EO material in these devices needs to be processed further using a process called "poling." Poling is one method of creating a net alignment of the dipole moments of the non-centerosymmetic EO molecules. This net molecular dipole alignment allows for high frequency manipulation of the refractive index of the EO layer.

Usually, poling is accomplished by heating a sample to its transition temperature and subjecting it to a DC electric field. The dipole moments of the EO molecules tend to align themselves in the direction of the applied field. The sample is then cooled in the presence of the field, maintaining the molecular dipole moments in their orientation. The electric field is removed once the samples have cooled to room temperature.

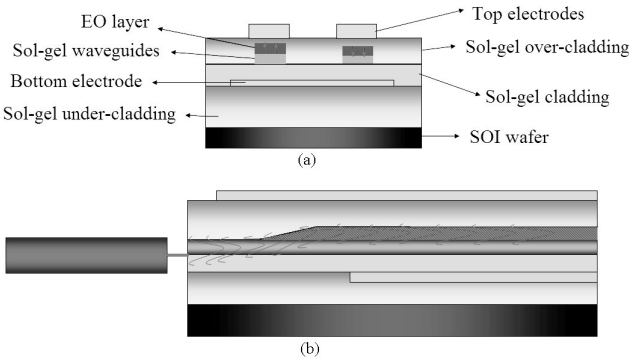

Figure 1. (a) Cross-sectional view of the sol-gel modulator. (b) Side view of the sol-gel modulator

Sol-gel can be used as the cladding material in the organic modulators (Figure 1), and for this reason it was used in the current study. Sol-gel is less conductive than most EO materials, which causes most of the applied electric field to drop across the sol-gel cladding rather than the EO core. Increasing cladding conductivity would allow for a stronger electric field within the EO layer, thus increasing net dipole alignment and reducing V_π. V_π is the voltage required to induce a phase shift of π radians between light traveling in the modulator's two arms. It is reported that doping carbon nanotubes (CNT) increases the conductivity of polymer[2], and for this reason, sol-gel polymer waveguide cladding was doped with CNT to study the effect of CNTs on the conductivity of sol-gel.

One can visualize the structure of carbon nanotubes as sheets of graphite that have been rolled into tubes. CNTs can be single-walled (SWNT) or multi-walled (MWNT), and individual nanotubes can have one of several rotational patterns for their

hexagonal, sp^2-hybridized carbon structure. The "armchair" and "zig-zag" structures, two of the many possible orientations, are illustrated in Figure 2.

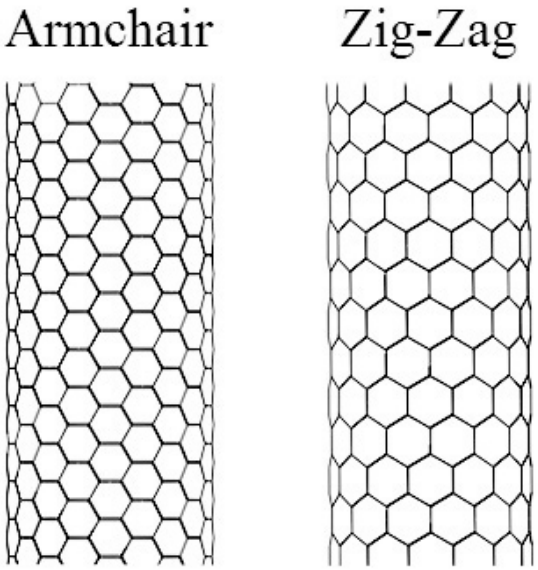

Figure 2. Armchair and zig-zag SWNT.

Conductivity ( ) is directly influenced by the geometry obtained during the formation, and although the electrical characteristics of SWNT are well known, the behavior of MWNT is more difficult to predict since the shells of MWNT do not all have to be the same type. For example, a double walled carbon nanotube could theoretically have an inner core with an armchair configuration, and an outer shell that is zig-zag. Due to the preliminary nature of this experiment, MWNT were used to reduce cost while retaining high purity nanotubes.

Results and Discussion

Homogeneous dispersions of CNT are extremely difficult to prepare, especially if the nanotubes are not functionalized. Thus, carboxylic acid functionalized MWNT pre-dispersed in methanol were purchased from NanoLab. They were then mixed with sol-gel solution, spin coated on ¼ of a gold-plated silicon wafer, and baked overnight at 120 ºC. Gold electrodes were sputter coated on the top of the sol-gel, wires were soldered in place, and the sample was poled.

The thin films were poled by first evacuating the poling chamber and backfilling with N_2, followed by heating the sample to 140 ºC in 15 min. The electric field was applied once the temperature reached 60-80 ºC, which corresponded to 5-7 min into the poling process. The potential was increased in steps every two or three minutes so that the desired bias was in place by the time the sample reached 140 ºC. The sample was kept at temperature for 15 min, after which it was returned to room temperature, and the bias was removed.

The current obtained during poling was used to calculate the conductivity using the following relation:

$$\text{Conductivity } (\sigma) = \frac{\text{Current (A)} * \text{Thickness of Sol-Gel (cm)}}{\text{Electric Field (V)} * \text{Electrode Area (cm}^2\text{)}}$$

Using Ohms law, the units become 1/(*cm), which is equivalent to S/cm, the traditional unit for measuring .

Although most of the samples had conductivity values that were significantly higher than sol-gel without CNT, the results did not monotonically increase with nanotube concentration as one might expect. Thus, while samples 2a, 3a, and 4a (Table 1) were all more conductive than 1a, sample 5a actually had a conductivity 36% lower than undoped sol-gel.

Sample #	% CNT	σ max (S/cm)	E-Field (V/μm)
1a	0	9.80E-11	102
2a	8.8E-06	6.63E-10	101.5
3a	4.4E-05	1.00E-10	72.3
4a	8.8E-05	5.30E-10	110.9
5a	1.8E-04	6.29E-11	101.5

Table 1. CNT doped sol-gel at 70-100 V/μm.

Samples 2b and 3b (Table 2) were the two highest concentrations of CNT tested, and they did not tolerate the regular 100 V/μm at 140 ºC. On the contrary, 2b and 3b repeatedly experienced dielectric breakdown (arcing) and shorted out under such a strong electric field. Consequently, a lower voltage regime was used to record the conductivity of these samples. For comparison, the 8.8×10^{-5} % CNT sample was also tested in the lower electric field.

Sample #	% CNT	σ max (S/cm)	E-Field (V/μm)
1b	8.8E-05	6.50E-09	5.5
2b	3.3E-03	2.40E-08	3.5
3b	6.6E-03	1.35E-08	6.25

Table 2. CNT doped sol-gel at less than 10 V/μm.

The two highest CNT concentrations (2b and 3b) show significantly higher than 1b. However, it may initially appear surprising that sample 3b, which had the highest CNT concentration, did not yield the largest . To contemplate this issue it is useful to compare samples 4a and 1b, which had the same concentration of carbon nanotubes yet displayed appreciably different conductivities.

The value of generally increases for each step of the electric field, as shown in Figure 3 by discontinuities in the first 19 min of heating. Thus, one might expect the 100 V/μm regime to yield greater , simply because larger steps in voltage involved. However, the samples tested at less than 10 V/μm actually exhibited greater conductivity than the samples tested at 100 V/μm. In other words, the conductivity of the cladding was dependant upon the electric field applied, and decreased as the potential is increased. For this reason, it is possible that sample 3b displayed a lower than 2b simply because 3b experienced nearly twice the electric field applied to 2b.

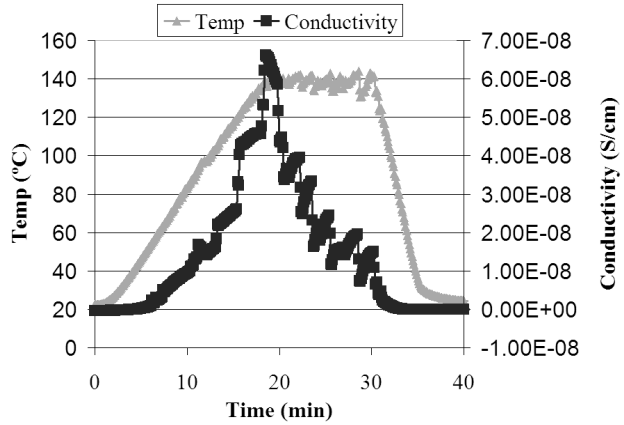

Figure 3. Temperature and conductivity of sample 2a, which contained 8.8×10^{-6} % CNT by weight.

A Perkin-Elmer Lambda 9 spectrophotometer was used to determine the absorbance of the samples. 2 mL vials were filled with sol-gel and cured at 70 ºC for 24 hours to obtain 0.5 cm tall samples with a diameter of about 1 cm. The results are shown in Figure 4 and do not indicate any significant changes in absorption around the 1.5 μm telecommunications window. Overtones from carbon-hydrogen stretching modes cause the peaks centered at 1.19, 1.40, and 1.62 μm, while oxygen-hydrogen bonds also contribute to the peak at 1.4 μm.

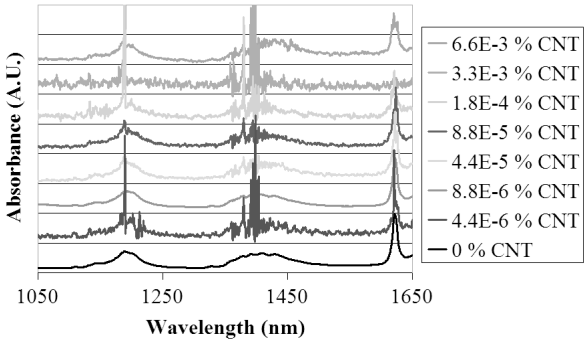

Figure 4. Absorbance of CNT-doped sol-gel.

Conclusions

Although most of the doped sol-gels had greater conductivity than the undoped sol-gel, the relationship between conductivity and CNT concentration cannot be clearly defined from the data obtained. Macroscopic imperfections and impurities, including air bubbles and dust particles were imbedded into the polymer during thermal cross linking of the sol-gel. Consequently, future work will not only include additional conductivity measurements of CNT doped sol-gel, but will be prepared in a clean room as to avoid contamination and the possibility of erroneous data.

In addition, the absorption characteristics of sol-gel were not significantly altered near the 1.5 μm wavelength telecommunications window. Therefore, doping sol-gel with CNT will not cause excessive optical loss, making these films suitable for use in waveguide-based photonic devices.

References

1. Dalton, Larry. Nonlinear Optical Polymeric Materials: From Chromophore Design to Commerical Applications. In *Advances in Polymer Science;* Springer Verlag: Berlin, 2002; Vol. 158, pp 1-86.

2. McLachlan, David; Chiteme, Cosmas; Park, Cheol; Wise, Kristopher; Lowther, Sharon; Lillehei, Peter; Siochi, Emilie; Harrison, Joycelyn; *Journal of Polymer Science B* **2005***, 43*, 3273-3287

Acknowledgments

Funds for this research were provided by the Center on Materials and Devices for Information Technology Research (CMDITR), and the NSF Science and Technology Center No. DMR 0120967. The authors would also like to thank Nathaniel Burt and Phil Sullivan for the technical help provided during many discussions.

Brandon Fetroe is attending Walla Walla College, where he plans to graduate with his BS degree in physics in 2007. He then plans to attend graduate school and wants to do research for a few years before teaching at either a high school or 4-year college.

Optical Properties of Two-Photon Chromophores in the Presence of Metal Ions and Electron-Deficient Molecules

Irma Hamilton, Jackson State University

Nisan Siegel, Dr. Mariacristina Rumi, Dr. Joseph Perry, Georgia Institute of Technology

Introduction

UV/Vis (color changing) and fluorescence-based sensing applications are continually being used and developed. They are useful for a variety of applications including hazardous-material detection as well as biomedical and security diagnostics. The variety and usefulness of applications could be extended with sensing processes involving two-photon chromophores. For example, studies have been performed by the Perry group on the optical properties of derivatives of bis(styryl)benzene (BSB)[1]. BSB derivatives are chosen to work with because of their structure which has an extended pi-electron system. This work resulted in design strategies and the identification of structure-property relationships for two-photon absorption and the synthesis of fluorescent molecules with unprecedented two-photon absorption. Molecules investigated possessed donor-pi-donor, donor-acceptor-donor, and acceptor-donor-acceptor structural motifs and demonstrated the effectiveness of bis-donor substitution in increasing the two-photon absorptive property/properties of dyes based on BSB.

In particular, donor-acceptor-donor chromophores with ligands such as aza-crown ethers have been demonstrated to efficiently bind to divalent metal ions. Experimental and computational results showed that the electron-donating strengths of the aza-crown nitrogen atom are reduced upon metal ion binding, and the absorption and fluorescent properties of the chromophores change accordingly[2]. Similar effects might be observed with other metal ions or analytes and the chromophores studied in this paper.

The purpose of this research was to determine the absorption and fluorescence properties of linear and cross-shaped two photon absorbing compounds which have electron donor substituents that are potential analyte binding sites. The binding properties of metal ions (Ag^+, Zn^{2+}, Ca^{2+}) and highly electron deficient organic molecules (as models for explosive substances) to these compounds were studied by monitoring changes in their absorption and fluorescence properties.

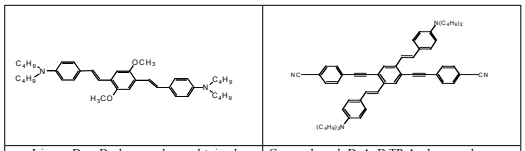

Linear D-π-D chromophore obtained from Seth R. Marder group | Cross-shaped D-A-D TPA chromophore was obtained from Uwe Bunz group

Figure 1: Chromophores studied

Results/Discussion

To determine λ_{max} and ε_{max} chromophores (see Figure 1) in the study and tetracyanoquinodimethane (TCNQ), solutions of the chromophores and serial dilutions were made and studied by UV/Vis spectroscopy. The results are in Table 1.

Table 1: UV/Vis data

Sample	λ_{max} *(nm)*	ε_{max} *(L/mol*cm)*
Compound L (acetone)	*427*	$8.2*10^{-4}$
Compound X (acetone)	*429*	$6.1*10^{-4}$
TCNQ (acetone)	*397*	$2.2*10^{-4}$
TCNQ (toluene)	*396*	

Legend: λ_{max} is the main UV/Vis absorption peak, while ε_{max} is the value of the molar extinction coefficient at that wavelength. Uncertainties in λ_{max} are +/-1nm and in ε_{max} are +/- 5%.

In order to study the binding properties between the analytes and chromophores, series of solutions (in acetone) were made with increasing concentrations of metal ions (from 0 to ~$6*10^{-3}$M) and a constant chromophore concentration of 10^{-5}M. The initial assessment of binding started with viewing of changes in the absorption spectra (i.e. as concentration of analyte increases a peak disappears, another peak appears and disappears, etc.). Increasing concentrations of zinc nitrate and calcium triflate show no systematic change in absorption spectra with either compound (see figures 2-5), indicating that little or no binding occurs at these concentrations of the metal ions.

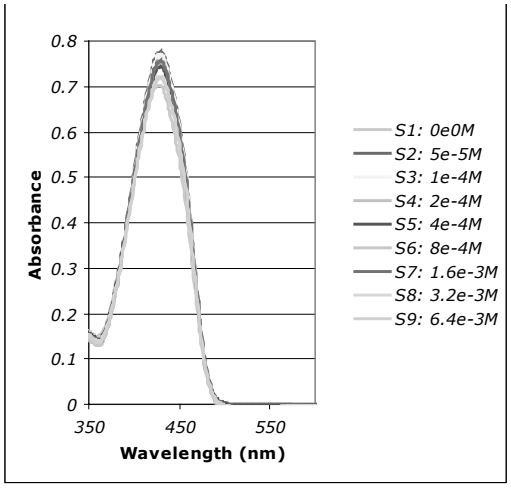

Figure 2: UV/Vis absorption spectra of series of mixtures of compound L and zinc nitrate in acetone

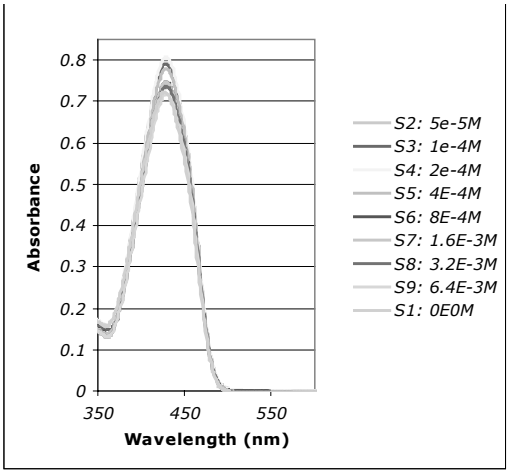

Figure 3: UV/Vis absorption spectra of series of mixtures of compound L and calcium triflate in acetone

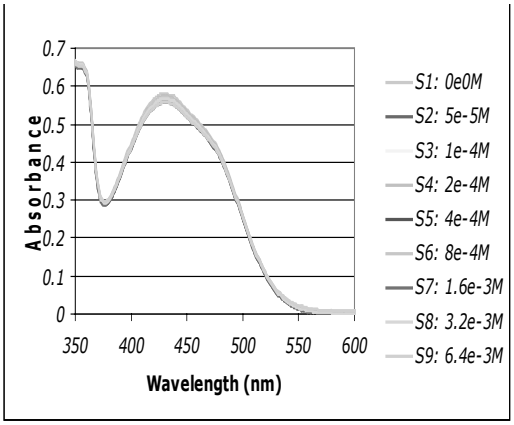

Figure 4: UV/Vis absorption spectra of series of mixtures of Compound X and Zinc nitrate in acetone

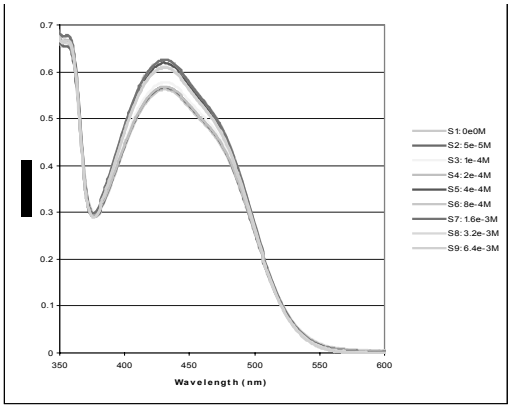

Figure 5: UV/Vis absorption spectra of series of mixtures of compound X and calcium triflate in acetone

Significant changes were observed for mixtures of either compound with silver nitrate (see figures 6-9). It has been shown in the literature[3] that the binding of two ligands to a single substrate can result in changes in UV/Vis absorption spectra described by the following equation:

$$\frac{\Delta A}{L} = \frac{[D_t](K_{11}\Delta\varepsilon_{11}[M] + K_{11}K_{12}\Delta\varepsilon_{12}[M]^2)}{1 + K_{11}[M] + K_{11}K_{12}[M]^2}$$

For the purposes of this paper, ΔA at any wavelength is defined as the absorbance of the pure compound minus the absorbance of the mixture of compound and analyte, L is length in cm (here equal to one and neglected), $[D_t]$ is total dye

compound minus the absorbance of the mixture of compound and analyte, L is length in cm (here equal to one and neglected), [D_t] is total dye concentration, [M] is metal concentration, K's are equilibrium binding constants for the binding of the analyte to the first and second amino groups on the chromophores, and $\Delta\varepsilon_{11}$ and $\Delta\varepsilon_{12}$ at any wavelength are defined as the extinction coefficient of the pure compound minus the extinction coefficient of the compound complexed to one analyte or two, respectively. This model applies when the concentration of either complex is much less than the concentration of free metal.

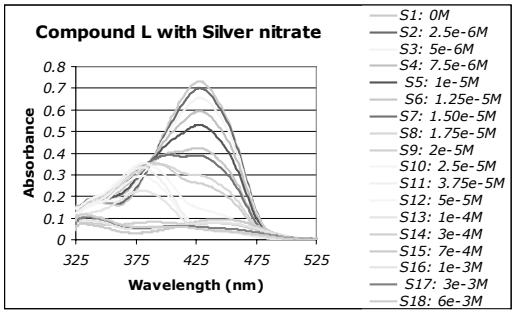

Figure 6: UV/Vis absorption spectra of series of mixtures of compound L and silver nitrate in acetone.

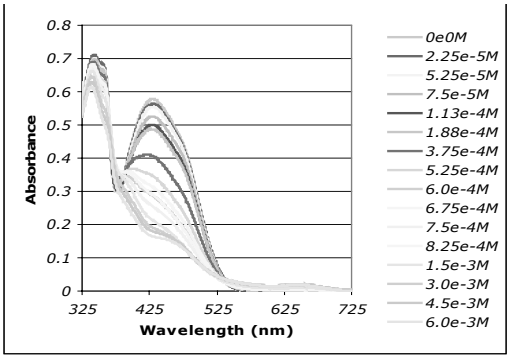

Figure 7: UV/Vis absorption spectra of series of mixtures of compound X and silver nitrate in acetone.

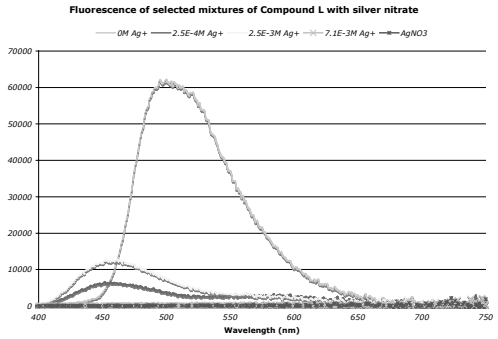

Figure 8: Fluorescence spectra of series of mixtures of compound L and silver nitrate in acetone. Concentration of compound L is $5*10^{-7}$M.

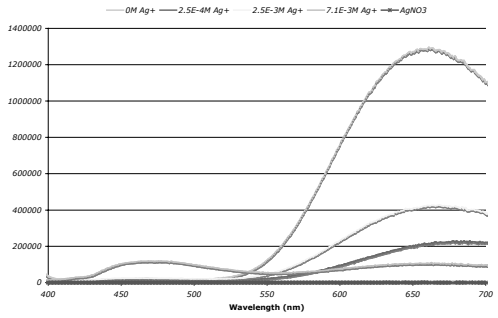

Figure 9: Fluorescence spectra of series of mixtures of compound X ($5*10^{-7}$M) and silver nitrate in acetone.

Absorption spectra of the compounds with TCNQ and dinitrotoluene (DNT) show no changes that are indicative of complex formation (see figures 10-11). Fluorescence spectra of the compounds when mixed with TCNQ show decreased intensity as TCNQ concentration increases (see figures 12-13). This is probably due to energy- or electron-transfer based quenching of the fluorescence by the TCNQ. Fluorescence spectra of the compounds when mixed with DNT showed no change at DNT concentrations comparable to TCNQ concentrations in the TCNQ-based plots, and these are not shown in this paper.

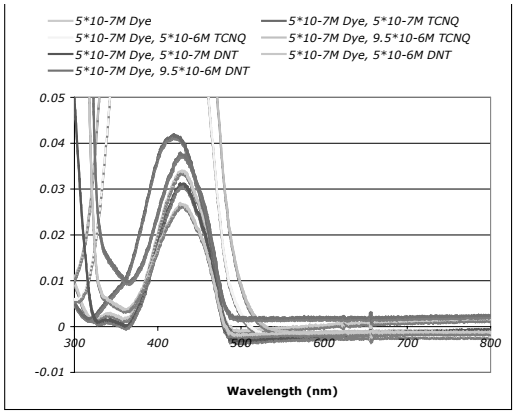

Figure 10: UV/Vis absorption spectra of series of mixtures of compound L and TCNQ or DNT in toluene.

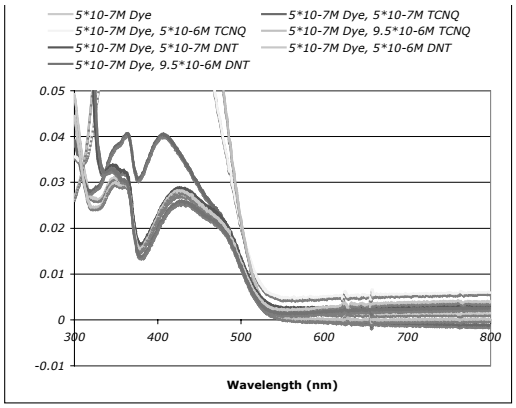

Figure 11: UV/Vis absorption spectra of series of mixtures of compound X and TCNQ or DNT in toluene.

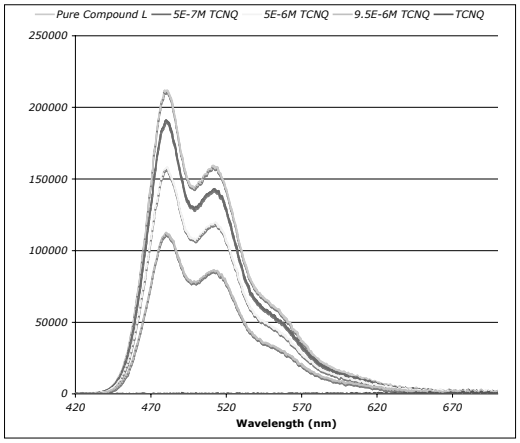

Figure 12: Fluorescence spectra of series of mixtures of compound L ($5*10^{-7}$M) and TCNQ in toluene.

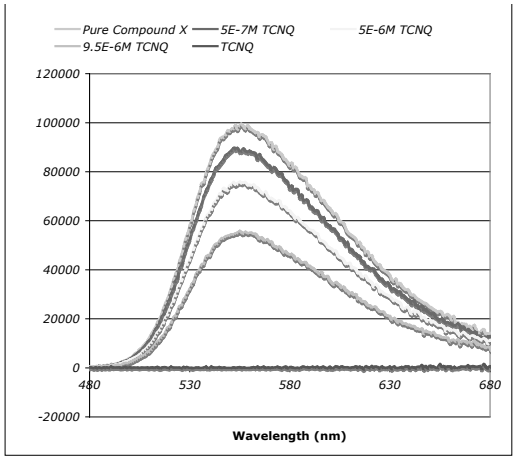

Figure 13: Fluorescence spectra of series of mixtures of compound X ($5*10^{-7}$M) and TCNQ in toluene.

Curves of experimentally determined ΔA as a function of [M] at several wavelengths were generated and fitted to the above equation of ΔA over length (see figure 14). From these fittings the equilibrium constants and $\Delta\varepsilon$'s were determined and are listed in Table 2. The initial guess for K_{11} was based derived from a semi-log plot[3]; the x-value at the point of inflection of the low-$[Ag^+]$ part of the curve is estimated to be equal to $\log(1/K_{11})$. In the case of compound X with silver nitrate, the initial estimate was ~10,000M^{-1} (see figure 15). The initial guesses for $\Delta\varepsilon_{11}$ were based on estimation from the observed spectra. This equation did not yield good fitting results for compound L and silver nitrate. A semi-log plot was generated of compound L and silver nitrate data (see figure 16) to obtain an estimate of K_{11}, resulting in a value of ~50,000M^{-1}).

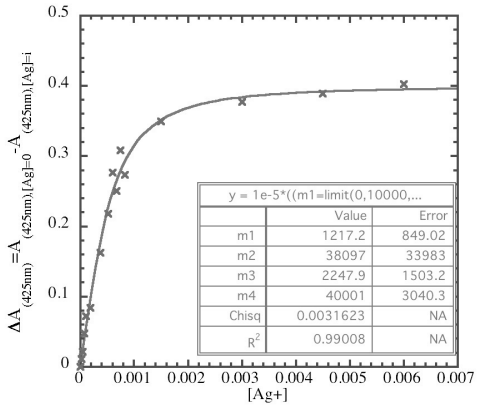

Figure 14: Plot of change in compound X UV/Vis absorbance at 425nm as a function of increasing concentration of silver nitrate. Concentration of compound X was 10^{-5} M in each solution. In the curve-fit results, m1=K_{11}, m2= $_{11}$, m3=K_{12} and m4= $_{12}$.

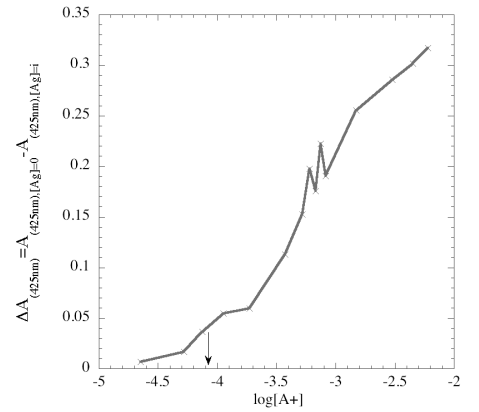

Figure 15: Semilog plot of change in compound X UV/Vis absorbance at 425nm as a function of increasing concentration of silver nitrate. Concentration of compound L was 10^{-5} M in each solution.

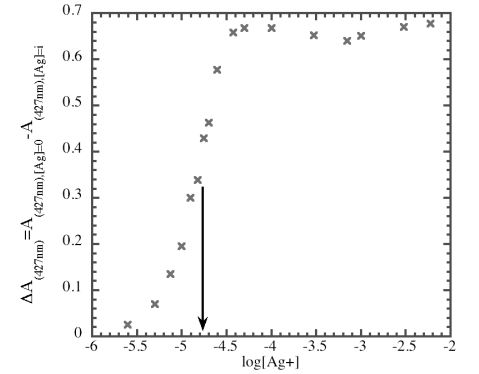

Figure 16: Semilog plot of change in compound L UV/Vis absorbance at 427nm as a function of increasing concentration of silver nitrate. Concentration of compound L was 10^{-3} M in each solution.

In the fits of the compound X/silver nitrate data to the equation on page 3, there is significant error in the values obtained for the binding constants (see Figure 14). Additionally, the second binding constant is calculated to be larger than the first, which is extremely unlikely. These problems are probably due to large covariance in an equation with four variables. A different fitting procedure should be used to attempt a more accurate fit. In the meantime, only the estimates of K_{11} as derived from the semi-log plots should be used as order-of-magnitude estimates of the binding strengths of the compounds with silver nitrate.

Conclusions

No significant change in UV/Vis absorption was observed for compounds L and X with zinc nitrate or calcium triflate, suggesting that no binding is occurring. Future work should be done to determine the fluorescent properties of these compounds with zinc nitrate and calcium triflate. Both compounds X and L are potentially useful for detection of silver ions by UV/Vis or fluorescence-based methods, with first binding constants on the order of 10,000 and 50,000 M^{-1}, respectively. These compounds may potentially be used for detection of selective organic analytes by energy- or electron-transfer based fluorescence quenching, although further work is needed to expand and refine knowledge of these systems.

References

1. Albota, Marius et al.; *Science* 1998. 281: 1653-1656
2. Pond, Stephanie J.K. et al; *JACS* 2004, 126: 9291-9306
3. Connors, Kenneth A. Binding Constants: The Measurement of Molecular Complex Stability. John Wiley & Sons, New York, 1987

Acknowledgements

Funds for this research were provided by the NSF Science and Technology Center on Materials and Devices for Information Technology Research (CMDITR). Special thanks to Dr. Joseph Perry's group, Mariacristina Rumi, Nisan Siegel, Georgia Institute of Technology, Jackson State University, Dr. Hong-tao Yu's group, Dr. Keith Oden, and Ms. Olanda Bryant.

After completing my undergraduate studies I hope to attend graduate school.

New Materials for High Efficiency Organic Light Emitting Diodes

Lauren E. Hayden, Georgia Institute of Technology

Dr. Simon Jones, Dr. Seth Marder, Georgia Institute of Technology

Introduction

The discovery of efficient electro-luminescence in organic and conjugated polymer thin films has led to interest in organic light-emitting diode (OLED) research. An OLED is a thin film light emitting diode in which the emissive layer is an organic or organometallic material. OLED technology potentially provides a less expensive alternative to the traditional liquid-crystal display (LCD). OLEDs do not require a backlight to function and, therefore, can potentially operate longer given the same charge and use less power than their predecessor. They can also be fabricated on more flexible materials allowing for the possibility of roll-up displays and portable screens. Some important problems stem from the limited lifetime of the organic materials used in the displays and the limited performance and durability of blue, green, red, and white OLEDs; therefore, more effective materials for OLEDs are required.

The structure of an OLED primarily consists of an organic emitter layer sandwiched between a transparent anode and a metallic cathode (Figure 1). The organic compound in the emitter layer must be able to transport electrons (high electron affinity) from the cathode and holes (low ionization potential) from the anode in order to produce light.[1] OLEDs emit light as a result of the recombination of the electrons and holes in the emissive layer (Figure 2). Holes are injected at the anode and move towards the cathode while electrons are injected at the cathode and move towards the anode. At the emissive layer, the electrons and holes recombine creating an excited molecule in either the singlet or triplet state. The excited molecule emits a photon as it relaxes back to the ground state leading to fluorescence (singlet state) or phosphorescence (triplet state).[2] The efficiency of this emission depends on the organic molecules used.

A problem with single layer devices is the difference in mobility of holes and electrons in the emissive layer. Holes typically move much faster from the anode towards the cathode than do electrons in the opposite direction, creating a charge imbalance. This imbalance causes many holes to move past electrons without recombination and emission.

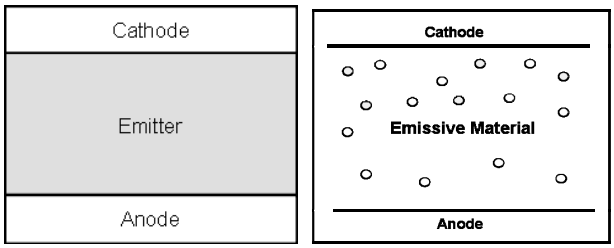

Figure 1. (left) General Structure of a single layer OLED device; (right) Rep. of electron and hole movement.

Therefore, using electron and hole transport materials to improve the probability of recombination can potentially improve the efficiency of the device. An easily oxidized material with high hole mobility and low electron mobility is needed for hole transport while an easily reduced material with high electron mobility and low hole mobility is needed for electron transport. These materials potentially allow for the concentration of electrons and holes at the emissive interface to maximize recombination.

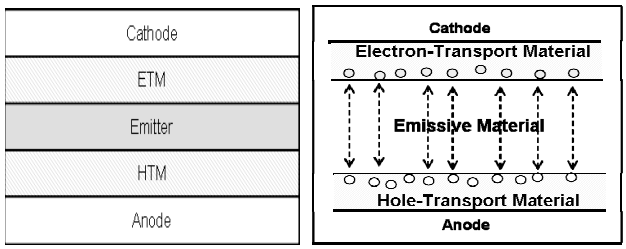

Figure 2. (left) Structure of a multi-layer OLED device; (right) Multi-layer rep. of electron and hole movement.

We are interested in polymerizable small-molecule materials such as (1) and (2) which could potentially increase the effectiveness and lifetime of OLEDs as they combine the properties of single

molecules with the material processibility of polymers. The two particular OLED materials studied were a bis(diarylamino) benzene-based hole-transport material (Figure 3) and a bis(carbazolyl) fluorene-based material (Figure 4). The hole-transport material (1) is an easily oxidizable material with the potential to be used as a hole-injection layer to improve injection of holes from the anode into the hole-transport layer while the carbazole-based material is based on small molecule analogues that have been shown to be effective hosts for iridium-based phosphors.[3,4] The important structural feature of our molecules is a polymerizable norbornene group.

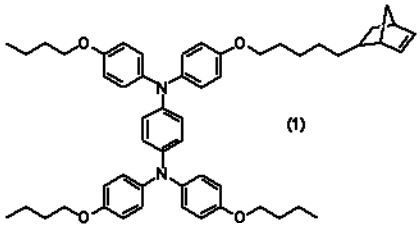

Figure 3. Structure of target molecule (1).

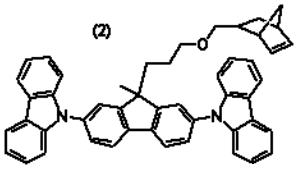

Figure 4. Structure of target molecule (2).

We have chosen norbornene as a suitable polymerizable group due to its low polarity and the ability to easily tune molecules through Ring Opening Metathesis Polymerization (ROMP) (Figure 5).

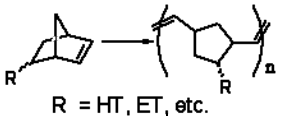

Figure 5. Norbornene polymerization.

Results and Discussion

A variety of techniques were used to synthesize, purify, and characterize the molecules. The molecules were synthesized using palladium amination, copper amination (Ullmann Reaction), and ether synthesis (Williamson Reaction). Subsequent functionalization reactions (e.g. bromination using N-bromosuccinimide (NBS)) were used to create substitution sites for further reactions. Protecting groups were also utilized in order to ensure the selective reaction of certain functionalities. Standard purification methods included column chromatography, recrystallization, and solvent extractions. ^{1}H and ^{13}C Nuclear Magnetic Resonance (NMR) Spectroscopy and Gas Chromatography with Mass Spectroscopy (GCMS) along with elemental analysis were used to identify synthesized compounds. Each new compound was fully characterized.

Synthesis of (1)

Target molecule (1) was synthesized in two parts, each using palladium amination. In the first half of the synthesis, aniline, along with *p*-butoxy bromobenzene, was stirred with $Pd_2(dba)_3$, 1,1'-bis(diphenylphosphino) ferrocene (DPPF), and sodium *tert*-butoxide in toluene. When complete, the catalyst was removed and the reaction mixture was purified by column chromatography. The triarylamine product was subjected to bromination using NBS in order to create a substitution site for further reactions. The reaction was carried out in dimethylformamide (DMF) under cold, dark conditions to ensure bromination at the desired site. After work-up, the reaction mixture was purified using column chromatography and characterized using ^{1}H NMR (1a).

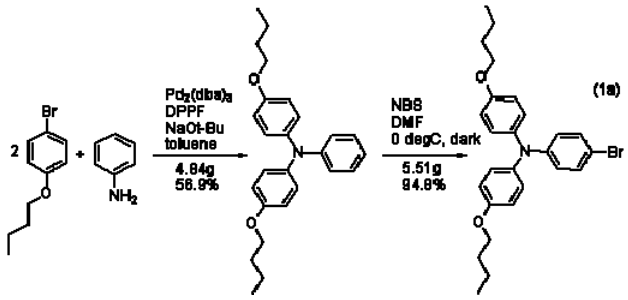

Scheme 1. Palladium amination and NBS bromination of aniline to synthesize structure (1a).

In the second half of the synthesis, a palladium catalyzed coupling reaction was performed with *p*-butoxy aniline, *p*-(*tert*-butyldimethylsiloxy) bromobenzene, $Pd_2(dba)_3$, DPPF, and sodium *tert*-butoxide in toluene. When complete, the palladium catalyst was removed from the mixture; the compound was purified using column chromatography and characterized by ^{1}H NMR (1b).

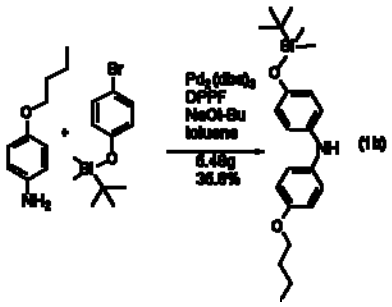

Scheme 2. Palladium amination of p-butoxy aniline and p-TBDMS bromobenzene to synthesize structure (1b).

The two purified compounds, (1a) and (1b), underwent an additional palladium amination to reach the current stage of the synthesis. This reaction formed the bis(diarylamino) benzene structure (1c) of target molecule (1).

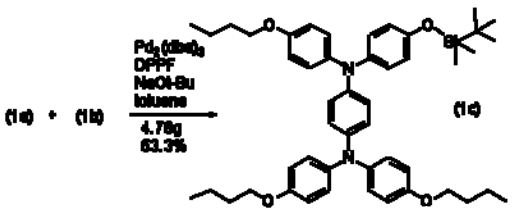

Scheme 3. Addition of (1a) and (1b) in a palladium catalyzed coupling reaction to synthesize structure (1c).

Two steps remain in the synthesis of target molecule (1): deprotection of the TBDMS group, and addition of the norbornene polymerizable group to the deprotected site. The deprotection will be carried out using tetrabutylammonium fluoride in THF followed by the addition of potassium carbonate, 18-crown-6, and the norbornene alkyl chain to form the target molecule. At each step column chromatography will be used to purify the compound and each new product will be fully characterized.

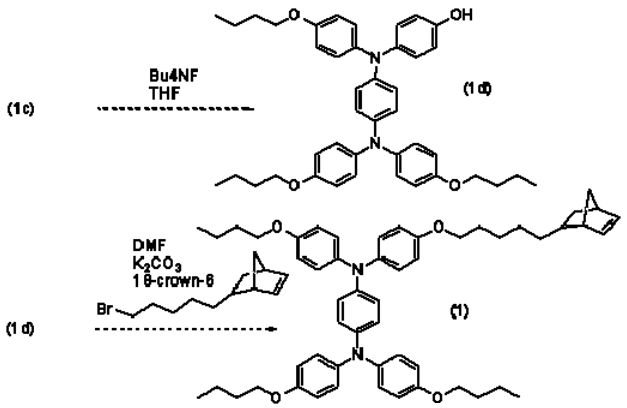

Scheme 4. Synthetic scheme of the remaining deprotection and alkyl norbornene addition in the synthesis of target molecule (1).

Synthesis of (2)

Target molecule (2) was partially synthesized from fluorene. Butyl lithium and methyl iodide were added to fluorene in dry tetrahydrofuran (THF) in order to methylate the 9-position on the fluorene molecule (2a). The methylated fluorene was iodinated (2b), to create substitution sites for further reactions. Each reaction product was purified by column chromatography.

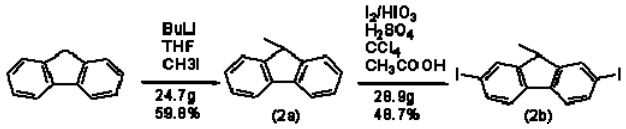

Scheme 5. Methylation and iodination of fluorene in the synthesis of (2a) and (2b) respectively.

3-bromo-1-propanol was protected using TBDMSCl and the protected compound was used to functionalize the 9-position of the fluorene. This group was added to provide a point of attachment for the norbornene polymerizable group. To attach this group, Diiodo-9-methylfluorene (2b) and 1-bromo-3-TBDMS were mixed with potassium hydroxide and 18-crown-6 in dimethylsulfoxide (DMSO). The reaction mixture was purified by column chromatography (2c).

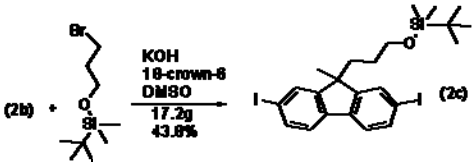

Scheme 6. Fluorene 9-position substitution of TBDMS alkyl bromide to synthesize structure (2c).

The bis(carbazolyl)fluroene structure was synthesized by reacting (2c) with carbazole in a copper amination (Ullmann Reaction). Following work-up, the product was purified by column chromatography and recrystallization.

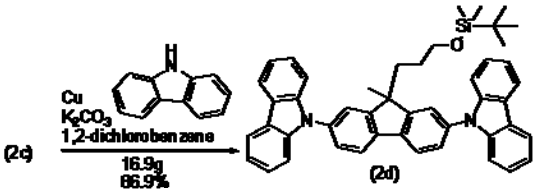

Scheme 7. Copper amination of carbazole with (2c) to synthesize the bis(carbazolyl)fluorene-based structure of target molecule (2).

Three steps remain in the synthesis of target molecule (2): a deprotection of the TBDMS group using tetrabutylammonium fluoride in THF, the addition of a tosyl group to the deprotected site to form a more easily substitutable tosylate, and an addition of the norbornene polymerizable group to the deprotected site using potassium carbonate and 18-crown-6 to form the target molecule. At each step column chromatography will be used to purify the compound and each new product will be fully characterized and recorded.

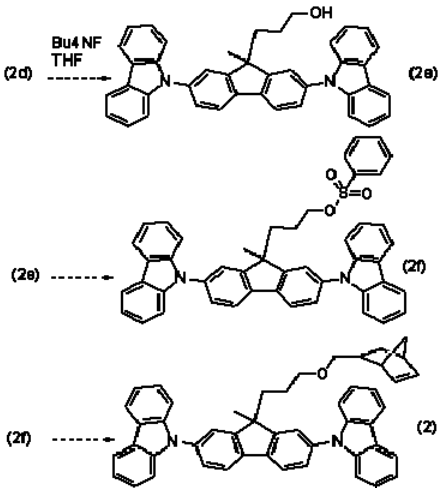

Scheme 8. Synthetic scheme of the remaining deprotection, tosylation, and alkyl norbornene addition in the synthesis of target molecule (2).

Conclusions

Significant progress towards the synthesis of potentially beneficial OLED materials has been made. Following completion of the syntheses, the materials will be tested in OLED devices to determine their effectiveness and overall benefit over current OLED materials.

References

1. A. Kulkarni, C. Tonzola, A. Babel, S. Jenekhe. *Chem. Mater. 16 (2004).* 4556-4573.

2. N. Armstrong, M. Wightman, E. Gross. *Annu. Rev. Phys. Chem. 52 (2001).* 291-422.

3. R. Hreha, C. George, A. Haldi, B. Domercq, M. Malagoli, S. Barlow, J. Brédas, B. Kippelen, S. Marder. *Adv. Funct. Mater. 13 (2003).* 967-973.

4. R. Hreha, A. Haldi, B. Domercq, S. Barlow, B. Kippelen, S. Marder. *Tetrahedron 60 (2004).* 7169-7176.

Acknowledgments

Funds for this research were provided by the Center on Materials and Devices for Information Technology Research (CMDITR), and the NSF Science and Technology Center No. DMR 0120967. Special thanks to Dr. Simon Jones, Dr. Seth Marder, and Dr. Stephen Barlow for their support and guidance.

Lauren Hayden is currently attending Georgia Institute of Technology with a major in Chemistry. After graduation in Spring 2007, she plans to attend graduate school and obtain her Ph.D in the field of Organic Chemistry.

Hydrophilicity and Hydrophobicity of Polymers on a Micro- and Macroscopic scales

Elizabeth Henderson, Bennett College

Robert Szoszkiewicz, Marcel, Lucas, Elisa Riedo, Georgia Institute of Technology

Introduction

Hydrophilicity (or a property of water- loving) pertains to polar molecules, and other materials that can effectively accommodate water's hydrogen-bonded structures.[1] Hydrophobicity (or a property of water- fearing) pertains to non- polar molecules and materials that disrupt the hydrogen- bonded structure of water without forming favorable interactions with the water molecules.[1] Hydrophilicity plays a key role in many diagnostic and medical device applications, for example in BD- logic glucose monitors and implantable intra-cranial pressure sensors,[2] as well as in drug delivery systems, such as transdermal and inhalation systems.[3] Enhancing hydrophilicity is important in industrial processes where restriction of a fluid flow creates problems, for example battery separators and printing applications.[4] Hydrophobicity plays a central role in many surface phenomena: it drives molecular self- assembly,[5] it is responsible for a structure of biological membranes,[6] and in determines the conformations of proteins.[7-8] On one hand, it has been known that some chemical groups protruding out of polymeric surfaces are making these surfaces either hydrophilic or hydrophobic. In particular, the carbonyl (- COOH) or amine (-NH_2) groups are hydrophilic, while alkyl (- CH_2-) or aryl groups are hydrophobic. These groups can be changed by a chemical reaction at the polymer surfaces, which should provide a convenient way of manipulating the hydrophilicity of the surface. On the other hand, the water on the lotus leaf has a high contact angle and rolls off the leaf, which is known as the lotus effect.[9] It has been showed that the cause of a lotus effect is not only the leaf's waxy surface composition, but as well the leaf's roughness on the microscopic and nanoscopic scales.[9] From that perspective, not only the surface chemistry, but roughness as well are the causes of hydrophobicity and hydrophilicity. Even more, it seems extremely beneficial to research any eventual changes in hydrophobicity/ hydrophilicity on the macroscopic as well as on the nanoscopic scales.

The objective of this project is to monitor the macroscopic and nanoscopic changes of hydrophilicity and hydrophobicity in the case of polymeric materials as a function of the temperature change. Temperature may cause alteration of roughness and surface chemistry of the chosen polymers. The Contact Angle Meter (CAM) is used to monitor the hydrophilicity changes on a macroscopic scale, while the Atomic Force Microscope (AFM) is used to monitor the hydrophilicity changes on a microscopic scale. CAM measures the contact angle of a droplet from a given fluid. The water contact angle is a direct indicator of macroscopic hydrophilicity/ hydrophobicity of that given surface. The AFM utilizes a sharp probe mounted on a cantilever, which moves over the surface of a sample in a raster scan. The changes of an angle of a laser beam reflected on the other side of the cantilever measure the cantilever's displacement. The vertical cantilever's displacement relates to the topography of the sample, while lateral cantilever's displacement relates to the frictional force between the tip and the sample. The AFM tips are usually hydrophilic, so the amount of their friction against a given surface is a good relative measure of the sample hydrophilicity at a local (nanoscopic) scale.

Polymer is a term used to describe a very long molecule consisting of structural units and repeating units connected by covalent bonds.[10] A few examples of polymers are DNA (the genetic blueprint that defines people and other living things), proteins and starches (in the food we eat), and tires (cars).[10] Based on their internal structure polymers can be divided into crystalline and amorphous polymers. Crystalline polymers include:

polyethylene and nylon. Amorphous polymers include: polystyrene and polyacrylic acid.

Polymer samples used in this study were synthesized and obtained (as 1 micron thick polymer films prepared on the glass substrate) by courtesy of Dr. Takashi Okada in Dr. Marder's group at the Chemistry Department at Georgia Tech. Details of the synthesis process will be published elsewhere. We used two different kinds of polymers (TAK-II- 020 and TAK-II-081). The sample TAK-II-020 is an ester derivative of the polyacrylic acid, while the sample TAK-II-081 is a cross-linked analogue of the TAK-II-020.

Results and Discussion

In figure 1 and 2 the contact angle measurements are presented as a function of the temperature, at which the polymeric samples were heated prior to the contact angle measurements at the room temperature.

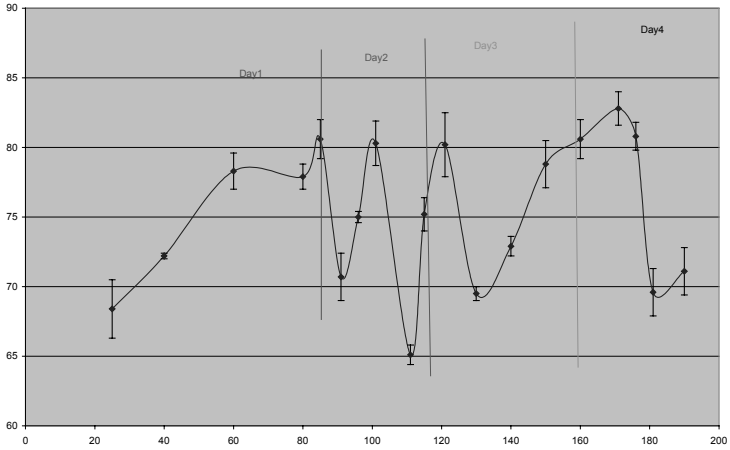

Figure 1: Temperature (deg C) vs. Contact Angle (deg) for ester derivative of the polyacrylic acid (TAK-II-20) sample.

The procedure used for the measurements consisted on placing the sample on the hot plate for five minutes, then letting the sample to cool down for five minutes, and finally starting the measurements at room temperature. These measurements were carried on during four consecutive days, so that in each day 3-4 new data points were obtained. The contact angle data points were calculated by taking the mean value of three independent contact angle measurements at

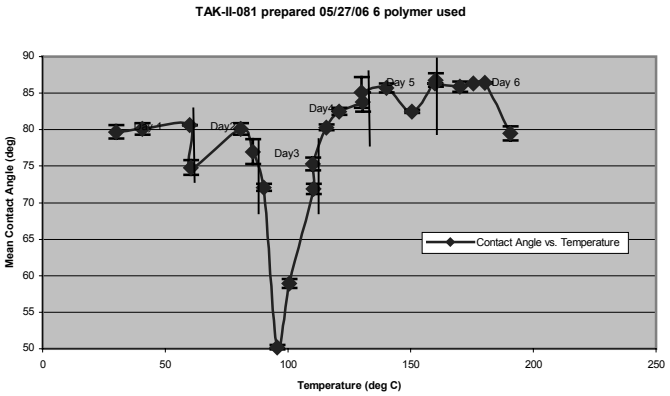

Figure 2: Temperature (deg C) vs. Contact Angle (deg) for cross-linked analogue of the TAK-II-020 (TAK-II-081) sample.

different points on the samples. The error (showed on the graph) was calculated by taking the standard derivation of these three contact angle measurements. To guide the eye, a smooth line unites the data points.

In both polymeric samples, as a function of the temperature, we expect a transformation of the moderately hydrophobic ester groups at the surface into the hydrophilic carboxylic acid groups, and eventually, under elevated heating, maybe slightly less hydrophobic anhydride can be formed at the surface. As a result, the overall contact angle of the samples against water is expected to decrease and then to increase as a function of the temperature. On the graphs we can see, however, oscillations of the contact angles and some inconsistency with a closer look. There are some factors that might cause these results not to be consistent. First, it is important to have the same size droplet, to be able to compare data and have accurate results. It has been tired to obtain contact angle with the same volume of the droplet. However, the volume of the droplets ranged from 9-20 milliliters. Second, any change of magnification on the camera and overall luminosity may cause the computer software to calculate the contact angle differently. The third factor is the time period. In figure 1, Day 1 (6/09/06) and Day 2 (6/12/06) the points on the graph have a huge gap (ten degrees). This might have something to do with measuring on a Friday and continuing to do the measurements on Monday. To have more accurate results, the last temperature on Friday should be re measured. In figure 2, Day 2 (6/16/06) and Day3 (6/26/06) the

points on the graph have a smaller gap (five degrees). This might have something to do with the measurements being done ten days later. When the measurements were done every day, the points on the graph looked consistent. When doing measurements and collecting data, it is important to do the measurements daily. Fourth, it has been noticed that the samples used for the contact angle measurements start with time to appear as if contaminated under magnifications of the optical microscope (a few tens of times). Small dust particles and maybe other contaminations as well collect on these samples, which is also believed to be a cause of the unexpected variations in the contact angles (fig.1, 2).

To investigate the micro-roughness effect on the hydrophobicity/hydrophilicity, the polymeric samples (TAK-II-020 and TAK-II-081) were also measured by an AFM. Four specimens were used, so that for each polymeric sample there was one specimen after the series of the contact angle measurements, and a new freshly prepared sample. The AFM data are presented in figures 3 to 6. Each figure consists on three images. The first image shows the topography of the sample. The second image shows the friction. The third image shows the topography cross section (line in the middle of the first image). The procedures for obtaining these images consisted on preparing the samples, placing an AFM cantilever in the cartridge for imaging, aligning the laser light on the AFM cantilever, and then on the AFM photodiode detector, then using software for to assist in the imaging process. The computer software calculated as well the RMS and mean roughness, which are respectively the root mean square and mean deviations from the mean height of the AFM image.

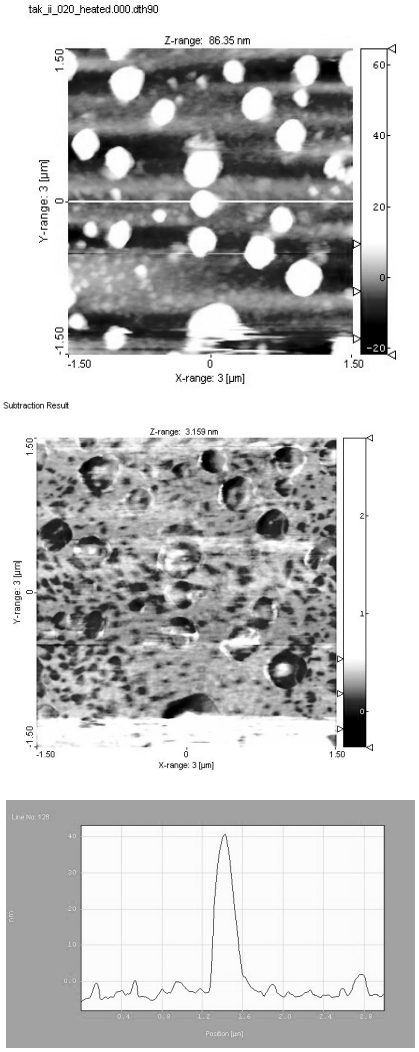

Figure 3: TAK-II-020 (non cross-linked) Heated

RMS = 10 nm

Mean roughness = 6.7 nm

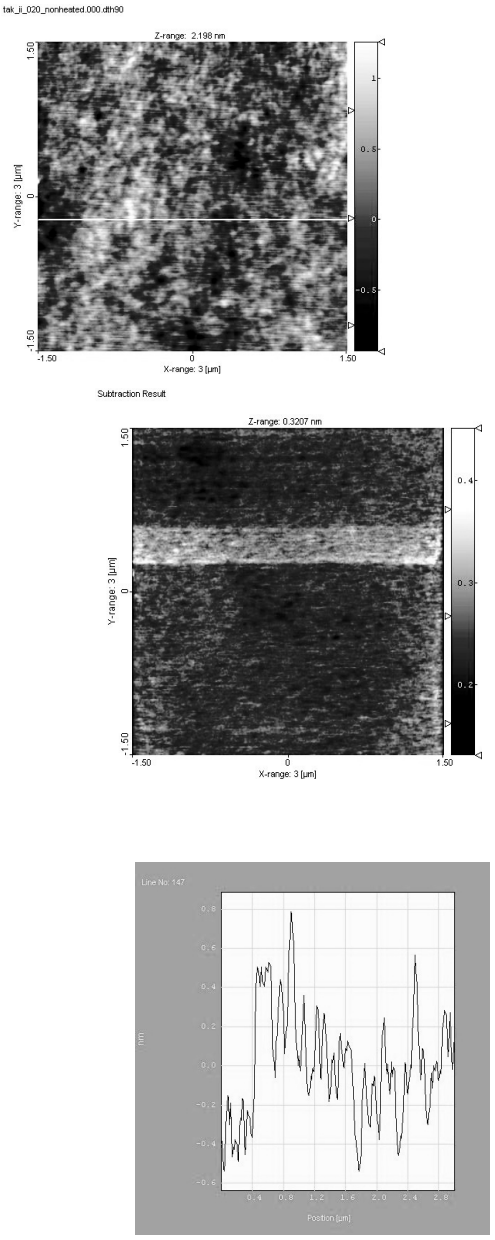

Figure 4: TAK-II-020 (non cross-linked) Not heated

RMS = 0.240 nm

Mean roughness = 0.190 nm

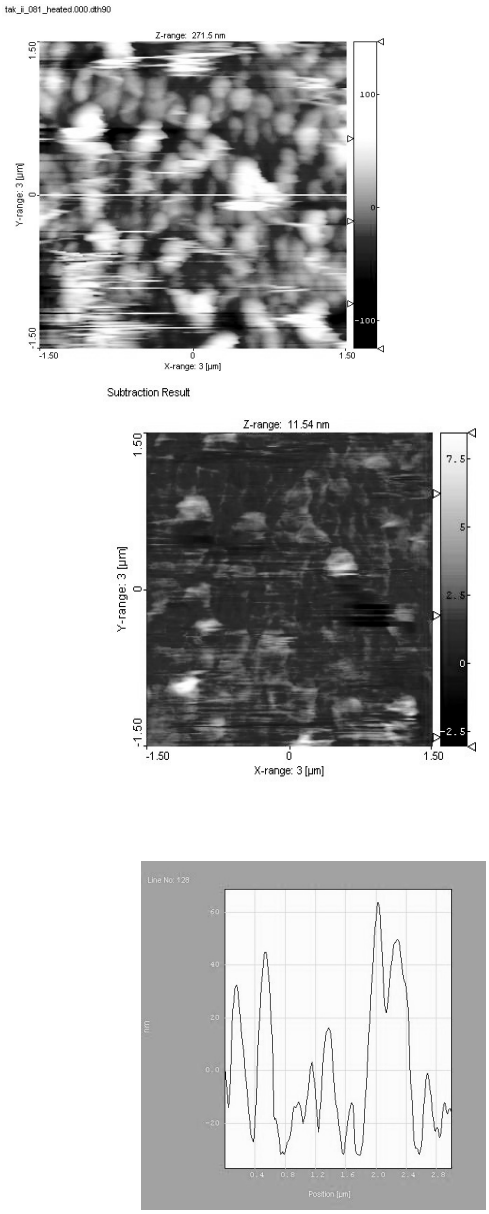

Figure 5: TAK-II-081 (cross-linked) Heated

RMS = 29.5 nm

Mean roughness = 23 nm

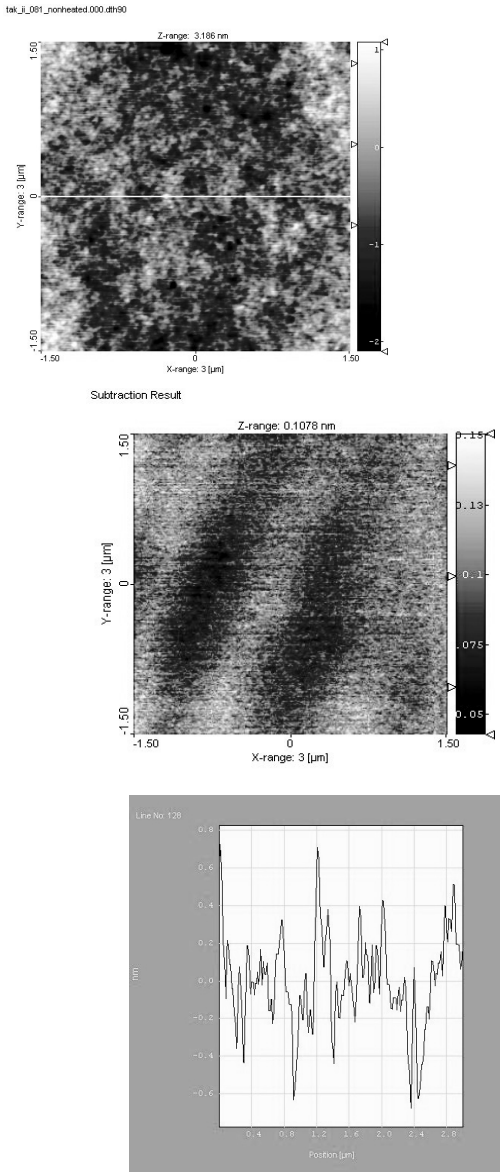

Figure 6: TAK-II-081 (cross-linked) Not heated

RMS = 0.268 nm

Mean roughness = 0. 212 nm

The AFM measurements show unambiguously that fresh samples are far smoother (smaller RMS and mean roughness values) that the samples imaged after prolonged contact angle measurements. Therefore, aging and dust accumulation might have influenced the contact angle measurements as well. Furthermore, we can speculate that maybe the heating changed the samples as well. To provide a benchmark of the hydrophilicity changes between heated and non-heated (fresh) samples, the overall friction was also calculated. For the TAK-II-020 sample the friction[11] on the fresh sample is 2.0 mV, while the friction on the heated sample is 33.5 mV. For the TAK-II-081 the friction on the fresh sample is 1.1 mV, while on the friction on the heated sample is 19.0 mV. These results show that heating and topography changes contributed to the increase of friction in the case of the two investigated samples. It will be, however, very interesting to investigate these changes of the topography and heating effects separately in the future by making AFM images after every few of the contact angle measurements.

Conclusion

In conclusion we have investigated the changes to the hydrophilicity induced by changes in the surface chemistry and topography of the two polymeric samples. Changes of the chemistry were realized by macroscopic heating, which was believed to transform the surface chemistry of the samples from the hydrophobic (ester groups on the surface) to hydrophilic (carboxylic groups at the surface) and then maybe slightly less hydrophilic (anhydride forming at the surface). Changes of the topography of the samples were observed when comparing the freshly prepared samples with the samples, which underwent the contact angles measurements. These topography changes are believed to originate during heating and via dust or other particles deposition caused be prolonged expose of the samples to air. Our results showed that the contact angle was indeed changing during heating on our samples, but oscillations of the contact angle and some inconsistencies are calling for the repetition of these measurements. AFM data showed as higher friction on the heated samples, which would be a sign of the increased hydrophilicity, but the friction interplay with topography calls for more detailed AFM measurements to be obtained between every few contact angle data points.

References

1. Definition of hydrophilicity/ hydrophobicity. http://www.qdots.com/live/render/content.asp (accessed 06/01/06).

2. Foster- Miller, Inc. Medical Devices/ Diagnostic Instruments http://www.foster-miller.com/m_mp_medical_devices_diagnostic_instruments.htm (accessed 06/02/06).

3. Gleason, William B. Drug Delivery Systems. Lecture Notes (accessed 06/01/06)

4. HydroLAST. http://www.astp.com/coating/hydrolast.html (accessed 06/02/06).

5. Self- assembly in nature is the way that hydrophilic and hydrophobic interactions cause cell membranes to self assemble. Wikipedia Encyclopedia. "Self- assembly". 2006. http://en.wikipedia.org/wiki/Self-assembly (accessed 06/01/06).

6. Cell membrane, mucous membrane, and S-layer. Wikipedia Encyclopedia. "Biological Membranes". 2006. http://en.wikipedia.org/wiki/Biological_membrane (accessed 06/01/06).

7. Fibrous proteins, such as collagen and keratin, consist of polypeptide chains arranged in roughly parallel fashion along a single linear axis. Protein. (n.d.). *The Columbia Electronic Encyclopedia, Sixth Edition*. Accessed 06/02/06, from Answers.com Web site: http://answers.com/topic/protein.

8. Israelachnvili, Jacob. Intermolecular and Surface Forces; Academic Press: San Diego, 1991. 131.

9. Cheng, Y.T. et al. *Effects of micro- and nano- structures on self-cleaning behaviour of lotus leaves. Nanotechnology* **2006**, *17,* 1359-1362.

10. Definition of polymer (physical and chemical properties)

http://en.wikipedia.org/wiki/Polymers#Physical_properties_of_polymers (accessed 06/19/06).

11. The error of friction data are + or – 2 mV.

Acknowledgements

The Center on Materials and Devices for Information Technology Research (CMDITR), Georgia Institute of Technology School of Physics, and the NSF Science and Technology Center No. DMR 0120967 provided funds for this research.

Personal Statement

My educational goal is to go to pharmacy school.

Electro-Optic Fabry-Perot Interferometer for Spatial Light Modulation at 980nm

Michael Hester II
"Norfolk State University"
Optical Engineering

Dr. Robert Norwood, Mentor
Dr. Nasser Peyghambarian, PI
College of Optical Sciences,
University of Arizona

Introduction

High-speed optical modulators and switches operating in the 1300 nm and 1550 nm range are proven to be ideal devices suited for optical communication networks such as long haul, metro, and fiber-to-home. Previous STC funded research has resulted in the demonstration of both modulators and tunable filters based upon a Fabry-Perot etalon consisting of a distributed Bragg reflector (DBR), a transparent electrode, and an electro-optic polymer and operating at 1550nm.

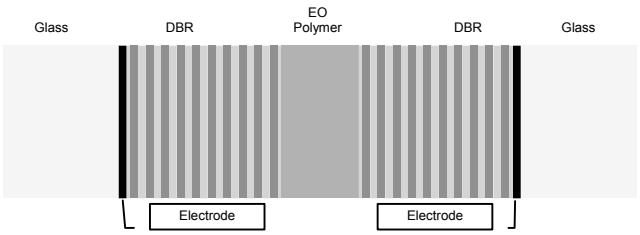

Figure 1. Standard EO-FP Layout at 1550nm

Objective of the Research Plan

The purpose of the proposed research is to design, construct, and characterize a Fabry-Perot etalon operating at 980 nm, that will focus on maximizing the reflectivity of the DBR mirrors while minimizing complete cavity loss; complementary studies will be performed in another program that will help to identify sources of cavity loss (i.e., surface roughness) and methods for minimizing them. The major advantage of the Fabry-Perot approach is that it can be applied directly to ultra-fast spatial light modulation; spatial light modulators (SLMs) are currently available using liquid crystals but these devices operate in the millisecond time scale, while EO polymer SLMs have the potential for extremely high speed operation (nanosecond time scale). There are several notable benefits to operating at 980nm, including the ready availability of sources at this wavelength, the good transparency of transparent electrode materials, and the enhanced activity of EO polymers at this wavelength. We believe that if the ITO electrode is moved inside of the cavity, absorption is reduced and leads to a lower operating voltage.

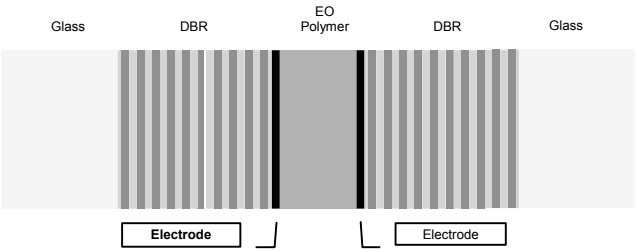

Figure 2. Proposed Fabry-Perot at 980nm

Research Methods

The research plan will be approached by using symbolic computation software, Maple 10™, to identify sources of cavity loss and methods to minimizing them. The new DBR mirror design will be constructed from alternating layers of the dielectrics silicon dioxide (SiO_2); with high chemical stability and electrical insulation, and tantalum pentoxide (Ta_20_5); with high thermal conductivity relatively high electrical conductivity, a high index of refraction. Fabrication of mirrors consisting of these materials can be performed using state-of-the-art sputtering systems in the College of Optical Sciences.

Figure 3 illustrates the results of design calculations for a mirror made from these materials with a design reflectivity of > 99% in the 1550nm region; actual measured reflectivities were in the 97% range. The goal is to use as few layers of SiO_2 and Ta_20_5 as possible which will increase the effective voltage

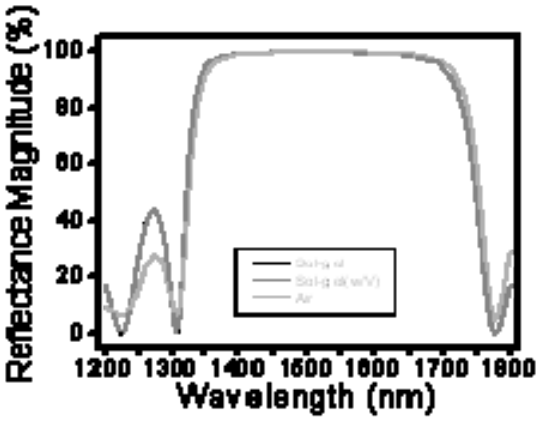

Figure 3. Design results for DBR mirror for the 1550nm region

across the EO polymer and decrease absorption loss and resistance. Using detailed measurements obtained from the optical properties of the new DBR determined by UV-VIS spectrometer measurements and direct measurements of fabricated etalons, I will compare theory with experiment and attempt to analyze the optical role of each layer in the Fabry-Perot. Key areas of interest include reflectivity, number of layers used, layer thickness, resonance wavelength, surface roughness/absorbance, and the refractive indices of all of the materials at the wavelength of interest. Based on these studies, the dependence of the refractive index on wavelength as determined by prism coupling measurements, film thickness, and surface roughness, one can attempt to improve uniformity and optimize the performance of the optical modulator.

Figure 4 illustrates the tuning of the transmission of an electro-optic Fabry-Perot etalon that has been accomplished in previous research.

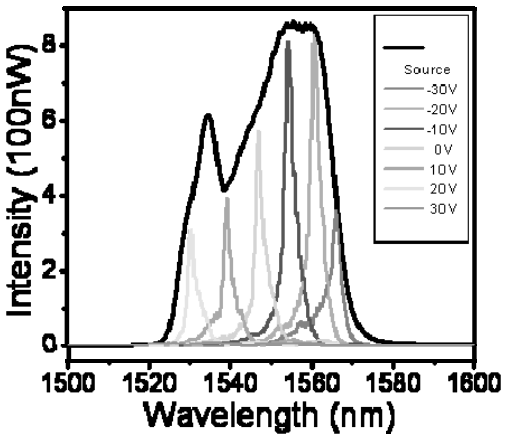

Figure 4. EO Fabry-Perot operating near 1550nm

Calculations

The following equations are based on the theory of multilayer films.

Equation 1:

$$M = \begin{bmatrix} Cos[k_0 h] & -iSin[k_0 h] \\ -\gamma_i iSin[k_0 h] & Cos[k_0 h] \end{bmatrix}$$

Where:

M = matrix layer
$k_0 = 2 /$ $_0$
h_0 = thickness
$_i$ = HI / LO Layer Index of Refraction
$_0 = 1050 * 10^{-9}$nm

Equation 2:

$$M = M_1 * M_2 * M_s * \ldots M_n = \begin{pmatrix} m_{11} & m_{12} \\ m_{21} & m_{22} \end{pmatrix}$$

Equation 3:

$$r = \frac{-m_{21} + m_{11}\gamma_0 - m_{22}\gamma_s + m_{12}\gamma_0\gamma_s}{m_{21} + m_{11}\gamma_0 + m_{22}\gamma_s + m_{12}\gamma_0\gamma_s}$$

Where:
r = reflectivity
$_0$ = layer
$_s$ = substrate

Equation 4:

$$R = |r|^2$$

Where:
R = reflectance
r = reflectivity

Results

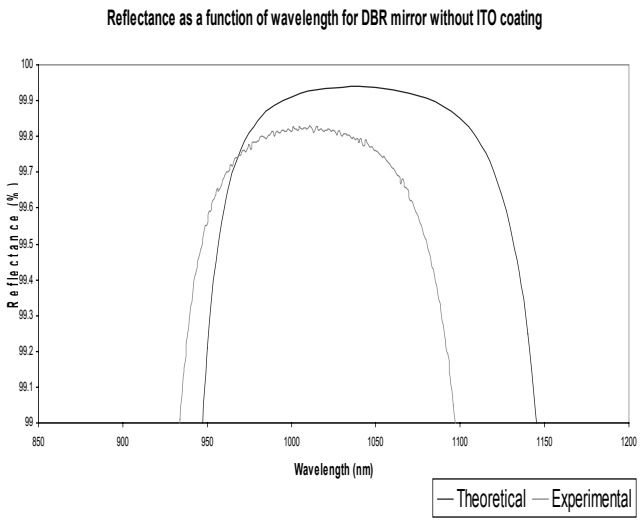

Figure 5. Reflectance as a function of wavelength for DBR mirror without ITO coating.

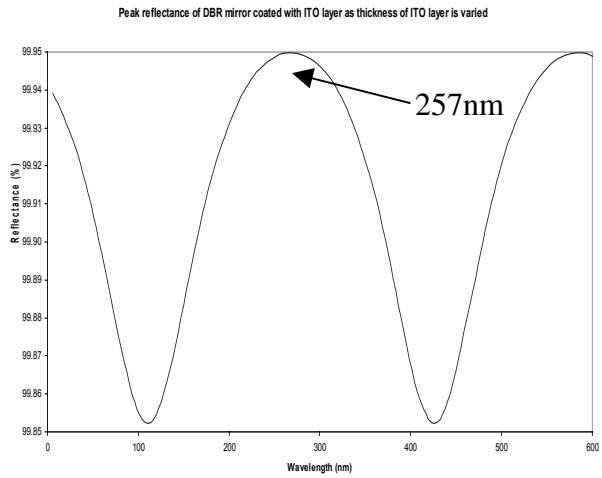

Figure 6. Peak reflectance of DBR mirror coated with ITO layer as thickness of ITO layer varies

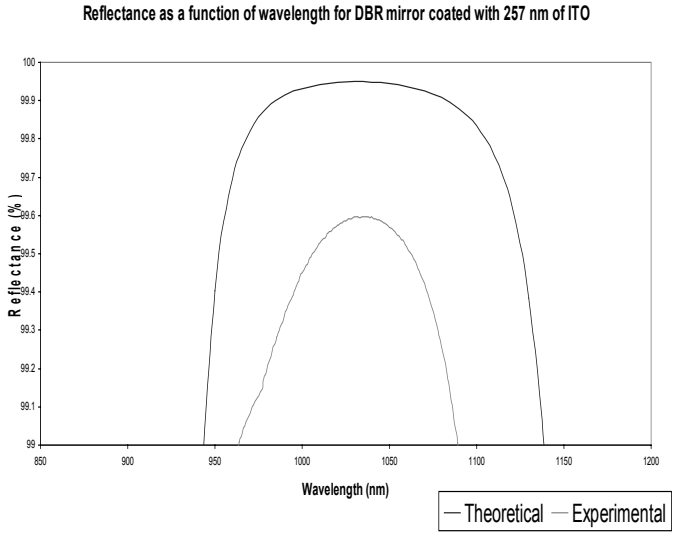

Figure 7. Reflectance as a function of wavelength for DBR mirror coated with 257nm of ITO

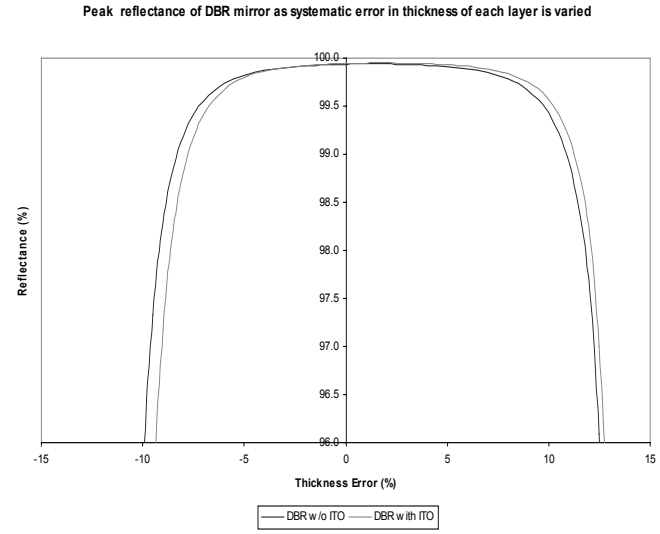

Figure 8. Peak reflectance of DBR mirror as systematic error in thickness of each layer is varied

Conclusion / Discussion

Based on the performed research, we can conclude that while theoretically the addition of an idealized ITO layer to a DBR mirror at 980nm does in fact maintain the designed reflectance, absorption and scattering in the actual deposited ITO layer decreases the reflectivity of the mirror from the predicted value. There is about a .3% difference. The resulting reflectivity is still much higher than what is possible at 1550nm with an ITO layer. The essential point is that we will be able to make a high finesse Fabry-Perot within ±5% error at the convenient wavelength of 980nm.

Future research will be to design and construct a distributed Bragg reflector mirror with ITO at 980nm, measure ITO properties, and model effects of film thickness variations.

References

1. Wyant, James; *Optics 505* **Spring 2000,** http://www.optics.arizona.edu/jcwyant/Optics505(2000)/ChapterNotes/Chapter08/multilayerfilms.pdf (accessed June 2006/July 2006)

2. Macleod, H.; *Thin-Film Optical Filters* **1969,** American Elesevier Pub. Co.

Acknowledgments

I would like to acknowledge the NSF Science and Technology Center on Materials and Devices for Information Technology Research (CMDITR, No. DMR 0120967 for funding; graduate student, Charles Greenlee, who assisted with the fabrication and use of the symbolic simulation software and assistance with characterizing the multilayer film stack; mentor, Dr. "Bob" Norwood, for his continuous interest and effort and involvement with the research, research plan, and presentations. Special thanks to Elena Temyanko, lab technician; Rick Franco, Majid Behabadi, Margaret Harden, Marilyne Stains, and Dr. Nasser Peyghambarian for their continued support and interest in inspiring youth of tomorrow in Science and Technology and the opportunity to have a progressive and successive research summer.

Future plans are to successfully earn an undergraduate degree in Optical Engineering with honors and pursue a Master's of Science degree in Optical Engineering with an aspiration of one day working in the government in the area of Optoelectronics.

Characterization and fabrication of liquid crystal lens

Terence Holloway
Norfolk State University

Guoqiang Li, Nasser Peyghambarian
College of Optical Sciences
University of Arizona

Introduction

Vision correction of age-related optical changes in the eye has been increasingly important as the life expectancy will continue to increase. Presbyopia is the symptom that people have difficulty in focusing close objects onto the retina because of the age-related decrease in amplitude of accommodation. While these people could have clear vision of distant objects, they would require reading glasses for viewing nearby objects. Since presbyopia tends to affect people in their forties, there is a significant need for this vision compensation. Ophthalmic lenses will be more capable and attractive if they have the freedom in adaptive changing the focusing power [1,2].It will provide the eye with an external accommodation to bring objects of interest at different distances into focus. Electrically controllable focusing lens can achieve this goal with the greatest field of view and high image quality without switching between the lenses. This kind of lens then allows the focal length to be voltage controlled without bulky and inefficient mechanical movement. Our goal is to create liquid crystal diffractive lens with high diffraction efficiency, relatively large aperture, fast response time, low operation voltages, and power-failure-safe configuration for near- (reading), intermediate- (e.g., computer screen, TV), and distance-vision[1,2].

Research Methods

The first steps taken in achieving this goal were the characterization of previous liquid crystal diffractive lens to improve the diffraction efficiency of the diffractive lens. Then we proceeded to fabricate a 16-level phase diffractive lens.

Fabrication:

The schematic drawing of the fabrication procedure is shown in Fig. 1. Using photolithographic techniques, concentric and rotationally symmetric transparent indium tin oxide (ITO) electrodes were patterned on a float-glass substrate. A 1 μm gap was required between adjacent electrodes to maintain electrical isolation and ensure a smooth transition of the phase profile introduced by the liquid crystal. Over the patterned ITO, a 200 nm-thick electrically insulating layer of SiO_2 is sputtered and into which small via openings were etched, allowing electrical contact to be made to the underlying electrodes. An electrically conductive layer of ITO is subsequently sputtered over the insulating layer to fill the vias and contact the electrodes and patterned to form eight independent electrical bus bars. Each bus bar connects the discrete phase level electrodes of equal counting index in all Fresnel zones.

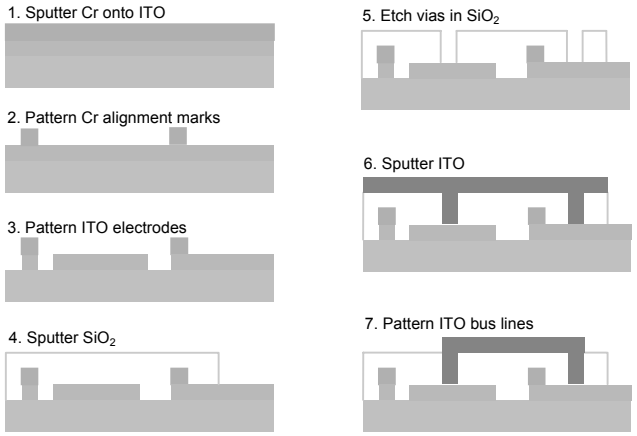

Figure. 1 Fabrication procedure

The patterned substrate, as well as an additional substrate with a continuous ITO electrode that acts as the electrical ground, were spin coated with poly(vinyl alcohol) to act as liquid crystal alignment layer. The alignment layers were rubbed with a velvet cloth to achieve homogeneous alignment and the two substrates were assembled. The commercial nematic liquid crystal E7 (Merck) was used as the electro-optic medium and was filled

by capillary action into the empty cell at a temperature above the clearing point (60°C) and then cooled at 1°C/minute to room temperature. The cell was then sealed with epoxy and connected to the drive electronics. The drive electronics consist of custom fabricated integrated circuits that contain eight independently controlled output channels. Each channel generates a modified square waveform with variable peak-to-peak amplitude between 0 and 5 V.

Characterization:

There many characterization steps involved such as the microscopic inspection operation of the electrodes, macroscopic inspection of extinction ratio & transmission, Interferometric testing focal length, wavefront, MTF, etc. The characterization procedures I was involved in are as followed:

(1) Operation of all the electrodes: Use a polarizing microscope to inspect the quality of fully fabricated lens on a microscopic scale as well as to check that all electrode structures are operating properly.
(2) Muller matrix imaging of an 8-level lens for phase map calculation;
(3) Measurement of the diffraction efficiency of the 8-level lens.
(4) Imaging property of the lens.

Results and Discussion

The function of the diffractive lens is based on near field diffraction by a Fresnel zone pattern. Constructive interference of the spherical waves coming from the various points creates high intensity at the observation point, corresponding to high diffraction efficiency[1,2]. The phase profile of an ideal diffractive lens is obtained by removing the multiple 2 phase retardation from the refractive lens. The most important parameter for a diffractive lens is diffractive lens is diffractive efficiency, which is determined by the phase profile across the lens. As the number of phase levels in the subzones increase, the diffraction efficiency also increases. In the diffractive liquid crystal lens, the Liquid Crystal (the electro-optic medium) is sandwiched between two pieces of glass in the vertical direction.

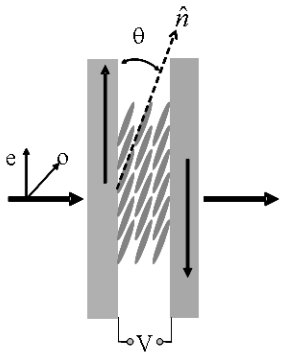

Figure. 2 Liquid Crystal Cell

The arrows in Fig.2 indicate the vertical axis. The optic axis of the liquid crystal molecule is aligned by vertically rubbing a velvet cloth in the vertical direction. Applying voltage to the cell changes the orientation of the liquid crystal molecules. is the angle between the optic axis of the liquid crystal molecule and the vertical axis. This angle maybe used to find the effective refractive index using the equation below:

$$n_e^{'}(\theta) = \frac{n_o n_e}{\sqrt{(n_e^2 \sin^2\theta + n_o^2 \cos^2\theta)}}$$

To obtain the phase retardation of the liquid crystal as a function of the applied voltage, the liquid crystal cell is placed between two crossed polarizers that are aligned with their transmission axis at 45° and -45° respective to the horizontal axis of the liquid crystal alignment layer, and the intensity of the transmitted light is recorded when the voltage is changed[1,2]. A total of two liquid crystal cell were tested. The data taken from Cell 1 was the intensity values with the range of the applied voltage being from 0.600 V to about 2.185 V.

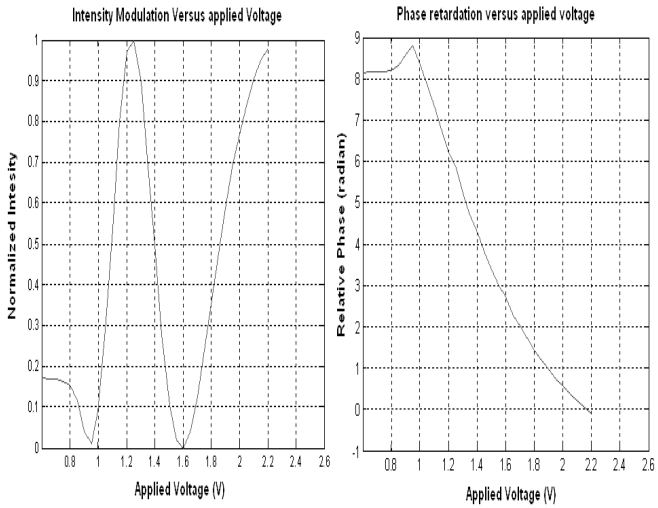

Figure 3 Data on LC Cell 1

As shown in the first graph we find that intensity modulation is a function of applied voltage. From that we are able to find the Phase Retardation of the cell. In the second graph, we find the relative phase retardation is a function of the applied voltage. In Cell 2 the same procedure was also taken but the range of the applied voltage was from 0.600 V to 1.900 V.

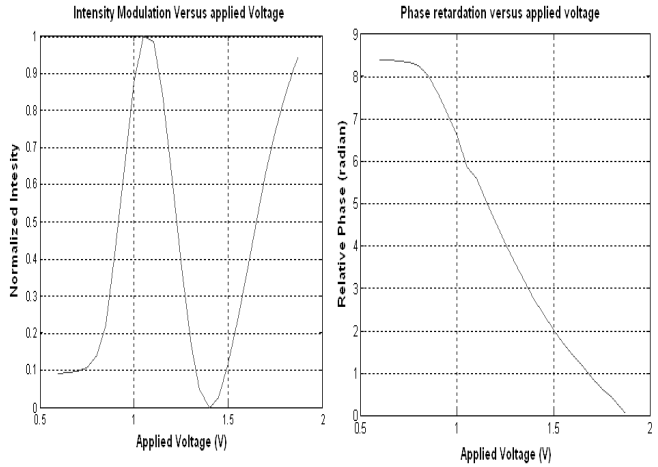

Figure 4 Data on LC Cell 2

The results shown in Cell 2 are very similar to what we found in Cell 1. Shown in the second graph is the threshold voltage, the point where the line starts to decrease linearly. This is due to when voltage is applied to the liquid crystal cell the orientation of the liquid crystal molecules are changed. The threshold value for both liquid crystal cells is about 0.800 V. When the voltage is larger than the threshold voltage, the director of the liquid crystal starts to reorient and there is an area in which the phase change is linear to the applied voltage. The linear range provides a phase change more than 2 , which is necessary for the diffractive lens. We find that the intensity changes with the change of the phase of retardation.

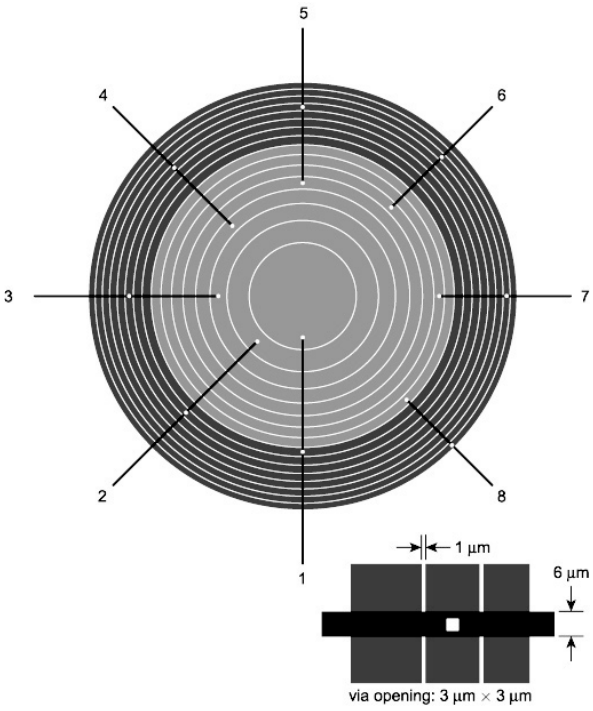

Figure. 5. Layout for 1-layer electrode pattern

In Fig. 5 we have a l-layer electrode pattern for an 8 level lens. This image has two central zones with 8 subzones in between. There is a 1-μm gap between each subzone. An electrical insulation layer with vias is added as shown with white dots. Each bus line connects to one electrode (subzone) in each central zone. By applying voltage to the electrode, different focal lengths can be obtained[1].

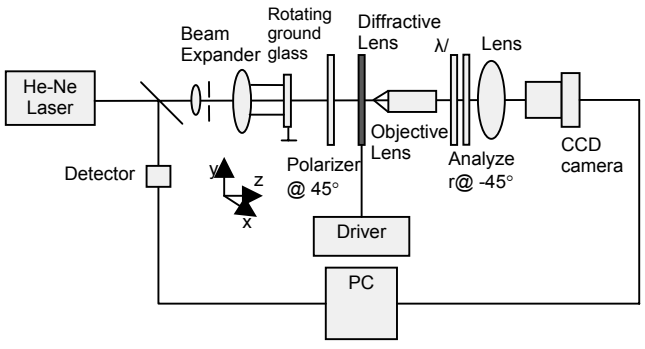

Figure. 6 Muller-Matrix Imaging

The setup as shown in Fig. 6 is the setup for the Muller-matrix imaging. The diffractive lens is placed between two crossed polarizers that are aligned with their transmission axis at 45° and 0° respective to the horizontal axis of the liquid crystal alignment layer, and the intensity of the transmitted light is recorded when the voltage is changed.. The He-Ne laser is used as the light source, the CCD is used to capture the intensity values, and the quarter waveplate is turned on the fast axis to capture the intensity values of the zones at 3 different angle positions. For each position on the lens, the intensity seen by the CCD is a function of the voltage dependent phase retardation between the ordinary and extraordinary wave components at the exit surfaces of the lens.

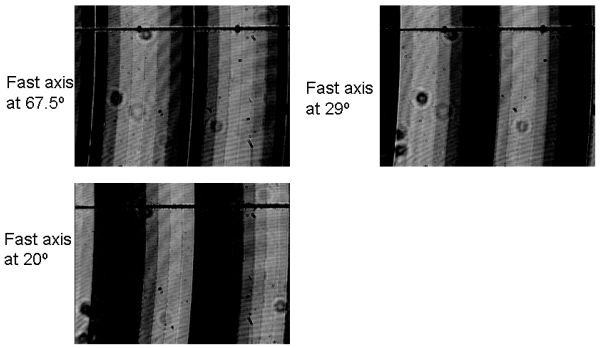

Figure 7. Results (1-D lens): Muller matrix imaging

The images shown in Fig. 7 are results of the intensity values of the zones and subzone when the fast axis of the quaterwave plate is set at 3 different angle positions. The voltage dependent phase retardation of each electrode can be inspected by observing the intensity variations over its area. The phase map can be calculated based on Muller matrix algebra

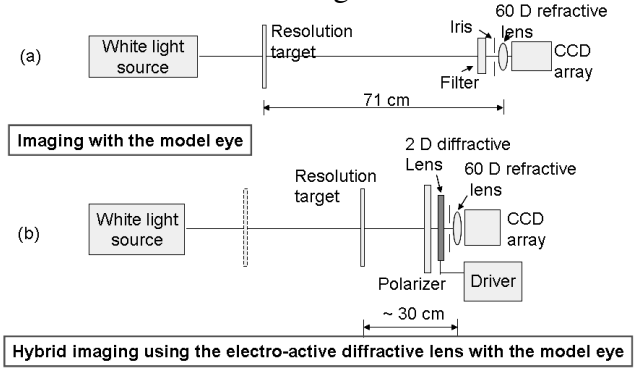

Figure 8. Model Eye-Vision

The image shown in Fig. 8(a) is the experimental setup for imaging with the model eye. The CCD camera acts as the retina; a 60 Diopter refractive lens is placed in front of the CCD to mimic the vision of the human eye; the filter is used to match the human photopic response. The resolution target is 71 cm away and that distance the image is clear. The image shown in Fig. 8(b) is the experimental setup for hybrid imaging using the electro-active diffractive lens with the model eye. The setup is similar to the first setup for the model eye but now a 2 diopter LC diffractive lens is placed in front of the model eye and a polarizer is added to the setup. The function of diffractive lens is to provide near-vision correction of the resolution target. The resolution target is now placed at 30 cm where the resolution target is not in focused. By applying voltage from the driver to the diffractive lens, different focal lengths can be obtained.

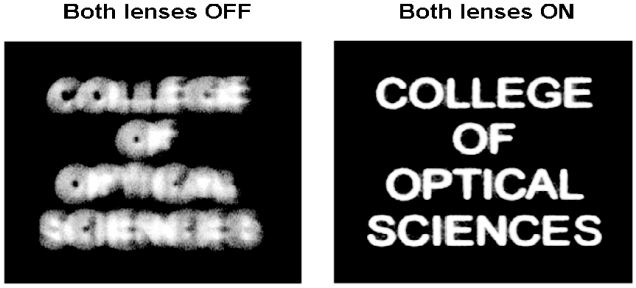

Figure 9. Hybrid imaging results

The images shown in Fig. 9 are the hybrid imaging results of the Liquid Crystal diffractive lens. When voltage is not applied to the liquid diffractive lens, the image is blurry. By applying voltage the lenses are placed into focus, thus the image becomes clear.

Conclusions

In conclusion, I was able to gain the concept of the LC lens and obtained hands-on experience in the following three aspects: Two liquid crystal cells have been assembled and characterized; an 8-level lens was studied from the microscopic scale based on polarizing imaging technique; went through all the processing steps for fabricating a new LC lens. The next steps to be taken, based on the research of Guoqiang Li, is the 16 phase level liquid crystal diffractive lens that was fabricated is to be characterized. Characterizations of this generation liquid crystal diffractive lens can be used to

progress and further advance other generations of liquid crystal diffractive lens. The goal of fabricating and characterizing Liquid crystal lens where met and maybe used in applications that may not only be limited to ophthalmology, but also in 3D imaging, optical data structure, optical information processing; fields where switchable lens elements with low operation voltages, high diffraction efficiency and rapid response time is desirable.

References

1. Li**,** Guoqiang; Valley**,** Pouria; Mathine, David L.; Äyräs, Pekka; Haddock, Joshua N.; Giridhar, M. S.; Williby, Gregory; Schwiegerling, Jim; Meredith, Gerald R.; Kippelen, Bernard; Honkanen, Seppo; and Peyghambarian, Nasser. *Proc. Natl. Acad. Sci,.* 2006, V103, 6100-6104.

2. Li, Guoqiang; Valley, Pouria; Giridhar, M. S.; Mathine, David L.; Meredith, Gerald R.; Haddock, Joshua N.; Kippelen, Bernard; Peyghambarian,, Nasser. *Appl. Phys. Lett.,* 2006, V89, (in press).

Acknowledgments

Funds for this research were provided by the Center on Materials and Devices for Information Technology Research (CMDITR), and the NSF Science and Technology Center No. DMR 0120967. I would also like to thank Dr. Arlene Maclin, Dr. Sean Jones, the faculty & staff of University of Arizona & Norfolk State University.

Terence Holloway will graduate from Norfolk State University in Fall 2008 with a B.S. in Optical Engineering. Upon completion he plans to pursue his Masters and possibly his PhD.

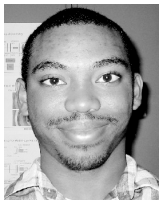

Designing and Building an Optical System to Measure the Birefringence of Polymer Optical Fibers

Andrea N. Joseph, Norfolk State University

Dr. Werner Kaminsky, Hien T. Pham, Dr. Ann Mescher, University of Washington, CMDITR

Introduction

The objective is to design and construct an optical device, which will allow the measurement of the polarimetric properties of polymer fiber. In particular, the optical device will be used to generate microscopic images from which the birefringence, extinction angle, absorption and linear dichroism of polymer optical fibers can be determined on a sub-second timescale. These features can be correlated with fiber quality, tension, orientation of micro-fibrils, and the dimensions of birefringent fiber. When coupled to the fiber manufacturing process, such process analytical measurements can be highly valuable in the fine-tuning of the optical properties of polymer fibers.

Optical fibers are transparent solid cylinders which transmit light through a large number of total internal reflections.[1] The Polymer Optics and Processing Laboratory is interested in fabricating and characterizing optical fiber composed of polymethyl methacrylate (PMMA). The material is often used as an alternative to glass. Advantageous properties of PMMA fibers include:[2]

- Simpler and less expensive components,
- lighter weight,
- operation in the visible light range,
- greater flexibility,
- ease in handling (polymer fiber diameters are ~ 1mm compared with 125 μm for glass),
- use of simple and inexpensive test equipment, and
- greater safety than glass fibers that require laser light sources for coupling in the waves.

Polymer optical fibers are emerging as increasingly significant components in a wide variety of optical transmission systems, particularly over short distances (10 to 100m apart).[3]

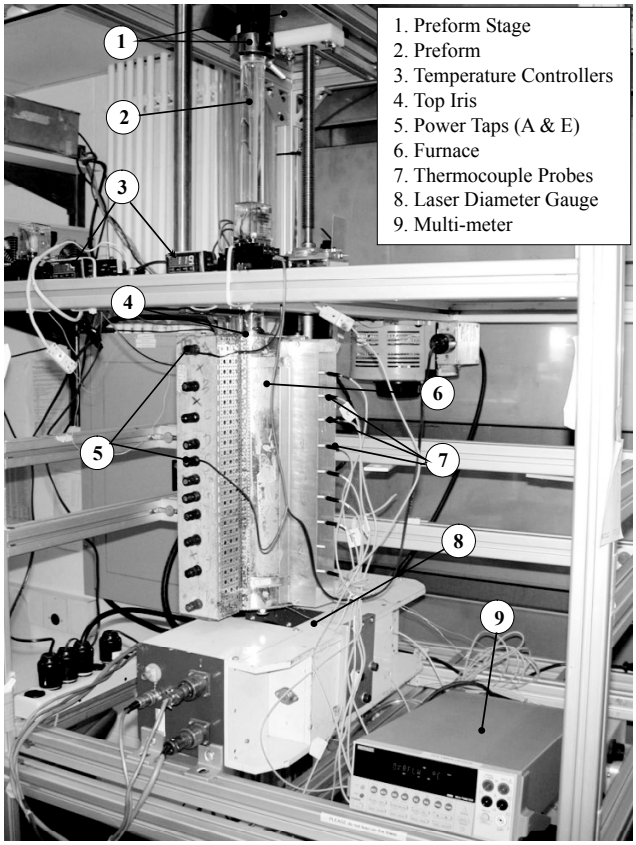

Figure 1: Polymer Optics and Processing Lab, Fiber Draw Tower.

In the Polymer Optics and Processing Laboratory, polymer fibers are fabricated using a draw tower (shown in Figure 1) in which the cross-sectional shape of the original preform is preserved as the polymer is drawn into fiber. For the birefringence measurements, a rectangular fiber cross-section will be used. Therefore, an acrylic preform with rectangular cross-section will be heated above its glass transition temperature in order to begin the fabrication process. Figure 2 shows a schematic of the fiber draw process. As the polymer is stretched into a fiber, the molecules within the polymer stretch and align along the long

axis of the fiber (Figure 2). The fiber is drawn at a speed which is many times greater than the speed at which the preform enters the furnace.

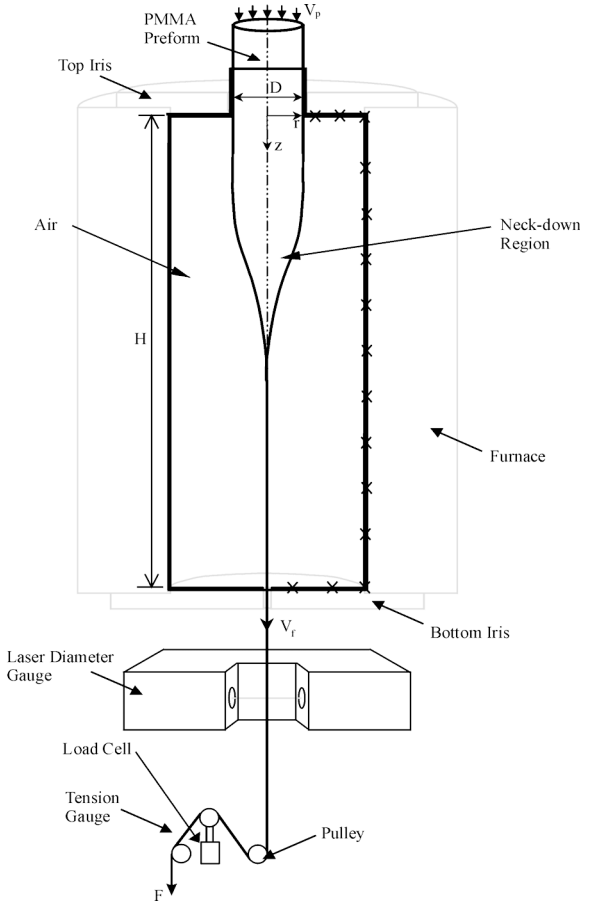

Figure 2: Polymer Optics and Processing Lab, Schematic of Fiber Draw Process.

Molecular alignment contributes to the birefringence and linear dichroism of the fiber. Birefringence is the measured difference between the indices of refraction within the fiber along both major and minor orthogonal axes. Similarly, linear dichroism refers to the smallest and largest absorption when measured with linearly polarized light for different polarization directions. One simple method to test the level of molecular orientation in a polymer optical fiber is to measure its birefringence, that is, the degree of refractive index anisotropy, which allows light in two orthogonal polarization states to travel at different speeds through the material.[4] As the birefringence is measured, it can be correlated to the mechanical stress placed upon the polymer during the draw process. As stress and birefringence are correlated and directly proportional, finding proper production settings for avoiding or minimizing birefringence may be desirable, allowing improvements in the fiber quality.

Birefringence can, however, have another profound impact on the propagation of electromagnetic energy through the polymer fiber, as it leads to constructive or destructive interference, which could be used to modulate the transmitted light intensity by the fiber itself for properly applied electric fields and electro-optic core materials. Characterizing birefringence can thus lead to the further development of light modulating devices, which could merge individual electro-optical switches directly within the fiber.

In application, a fiber will need to be moved in curved paths to connect between other optical entities. Bends and stresses in the fiber introduce regions of birefringence with varying orientation, leading to changes in the polarization of the guided light. The use of highly birefringent fibers can reduce such environmental influences.[5] By purposely influencing birefringence, it can become less of a liability in fabrication.

Results and Discussion

Based upon the design and drawings of Dr. Werner Kaminsky, we constructed an optical system capable of measuring birefringence of the polymer fibers. While many of the system components were commercially available, some of the components were fabricated using templates machined by Kevin Soderlund in the Mechanical Engineering Departmental Machine Shop. In Figure 3 some of these components are pictured.

In order to build this device, we first ordered certain commercially available components including: an achromat, a 70x20 lens, a 20mm glass polarizer, a 70mm glass polarizer, an IR filter and a commonly available CCD camera. Using the aluminum templates, we were able to create the glass prisms from common window glass.

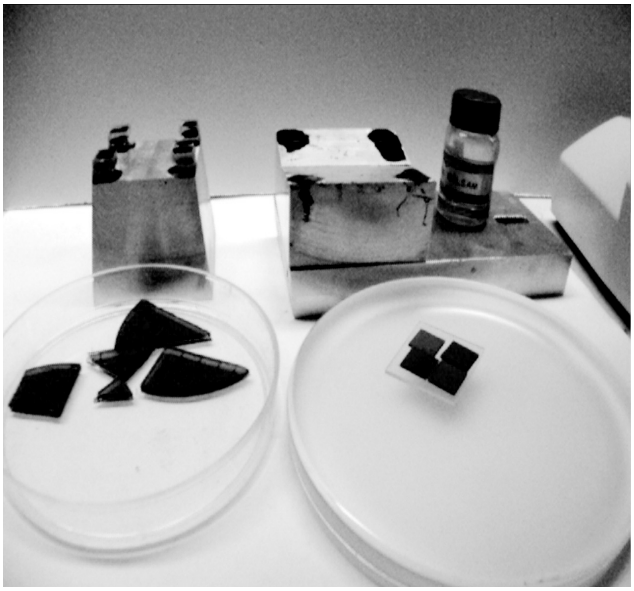

Figure 3: Templates and components used to fabricate the optical system. Clockwise from top left: Prism edge template, prism surface template, Canada balsam, common glass on grinding plate, cut pieces of polarizer glass.

The rough cut pieces of glass were affixed to the top four corners of the prism edge template (shown in Figures 4a and 4b) using common pitch. The edges were then ground flush and smooth with the seven degree angle of the template using a diamond surface glass grinder.

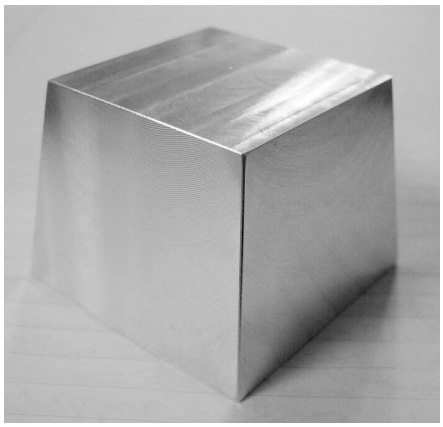

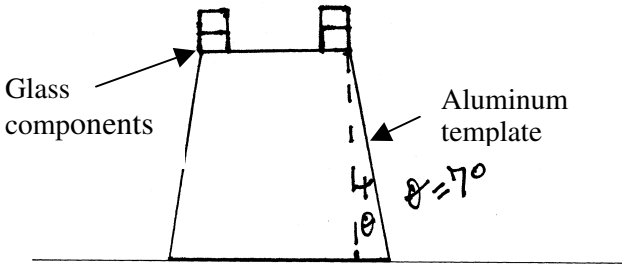

Figures 4a (top) and 4b (bottom): Prism edge template photograph (4a) and diagram (4b). Glass prism components are affixed in two layers to each of the top four corners of this template using pitch. This template is used to give each of the prism components a 7° slope along two edges.

The edge grinding to seven degrees was done on a diamond grinding plate to ensure that the internal edges of a 4-piece prism fit together in a flush and smooth manner. Additional fine grinding was done using sapphire grinding powder and a grinding plate.

Following the grinding of the edges, the glass pieces were then attached to the prism surface template (Figures 5a and 5b) using pitch. The surfaces were then ground smooth to the desired surface elevation of ten degrees. Again, fine grinding was performed using the sapphire grinding powder and grinding plate.

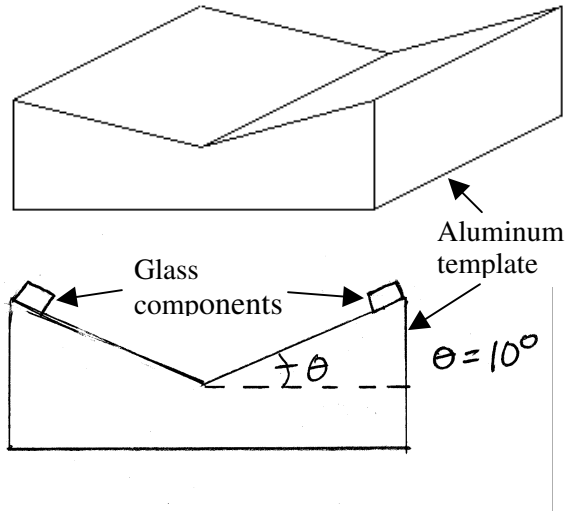

Figures 5a (top) and 5b (bottom): Diagram of the prism surface template. Figure 5b shows how the glass prism components are affixed to this template using pitch. The surface of the glass is ground on the diamond plate. This template is used to give the surfaces of the prism components a 10° slope.

The polarizers were ground without using pitch, but were rather affixed within a template (Figures 6a and 6b) to protect the heat sensitive glass-polymer-glass layers of the polarizer glass and to prevent scratching. The polarizers were oriented as shown in Figure 6b, and then the edges were ground flush to the straight template edges using the diamond grinding plate.

Both the prism and polarizer components were assembled (Figures 7a and 7b) using Canada Balsam, because it has the same index of refraction as glass and therefore does not interfere in the optical pathway. These components were then affixed within the housing of the device as shown in Figure 8. The housing for the device shown in

Figure 9 was fabricated by Kevin Soderlund based on the drawings and specifications of Dr. Kaminsky.

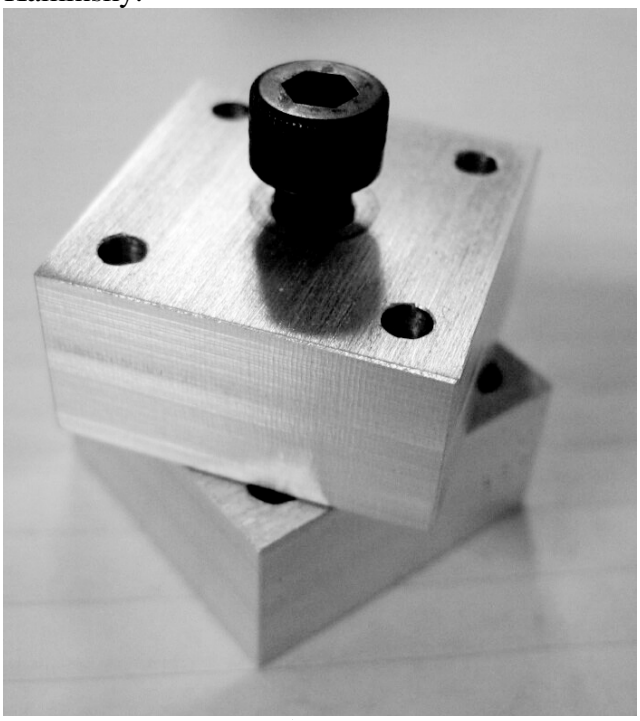

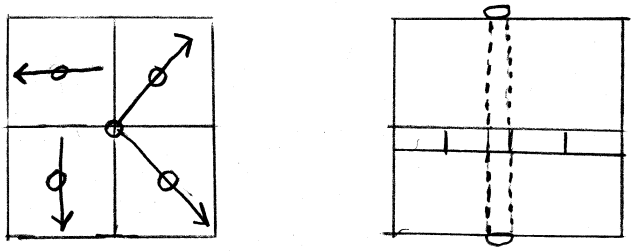

Figures 6a (top) and 6b (bottom): Polarizer template photograph and diagram. Polarizer components are affixed within this template under the holes on each corner between the two blocks which fasten with a screw. The holes in the template allow the verification of the orientation of the polarizer pieces. The polarizer orientations are shown in the lower left diagram.

Conclusions

An optical imaging device which generates images of the birefringent fiber was successfully constructed. The Milliview© software, as shown in Figure 10, then analyzes those images generated by the device.

The software analysis provides values which correspond to the birefringence of the fiber, the extinction angle, and the relative intensity of the transmission through the fiber. The software is also interactive with the microscope settings. For example, the magnification setting of the microscope can be indicated within the software. Additionally, the software can be set to select a range of light wavelengths (red, blue, or green) for imaging the fiber.

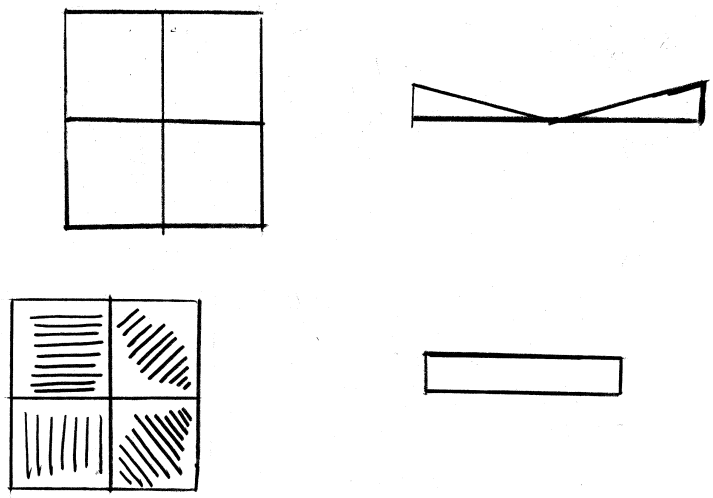

Figures 7a (top) and 7b (bottom): In Figure 7a on the left is the "top down" view of the assembled prism. On the right is the side view of the prism in which the 10 degree slope can be seen. In Figure 7b on the left is the "top down" view of the assembled polarizer showing the relative orientations. On the right is the side view of the polarizer.

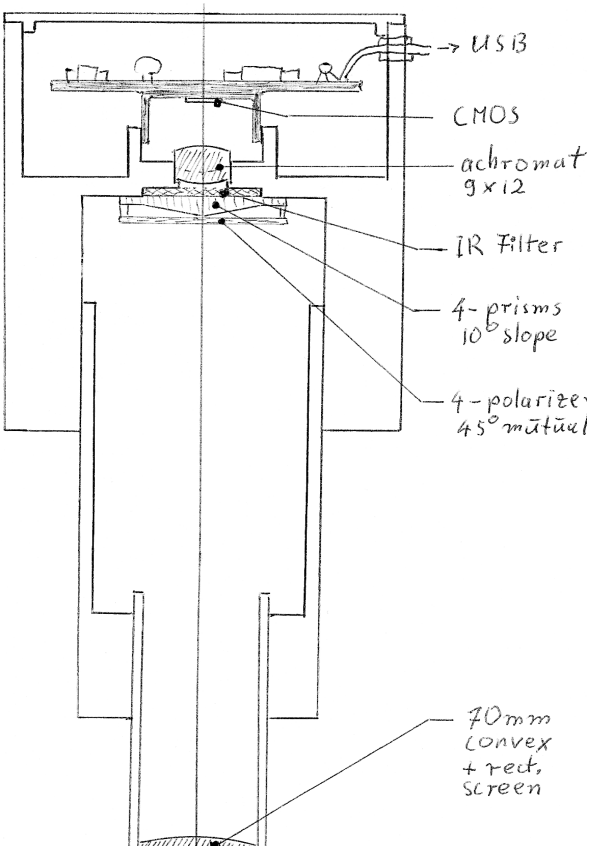

Figure 8: Drawing of Assembled Optical Device by Dr. Werner Kaminsky.

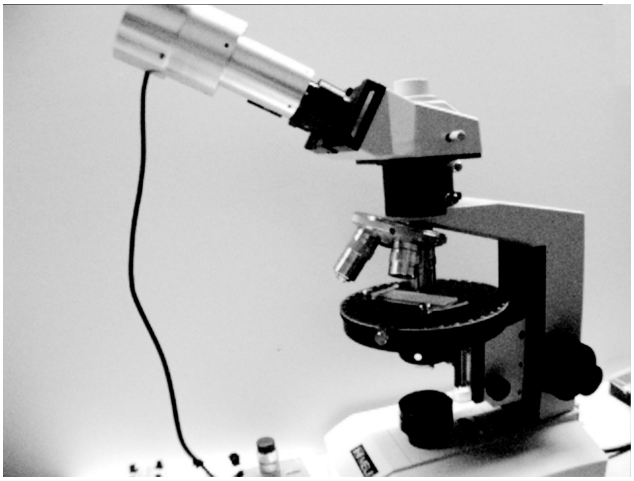

Figure 9: Birefringence Imaging Device, attached to a microscope through an ocular slot.

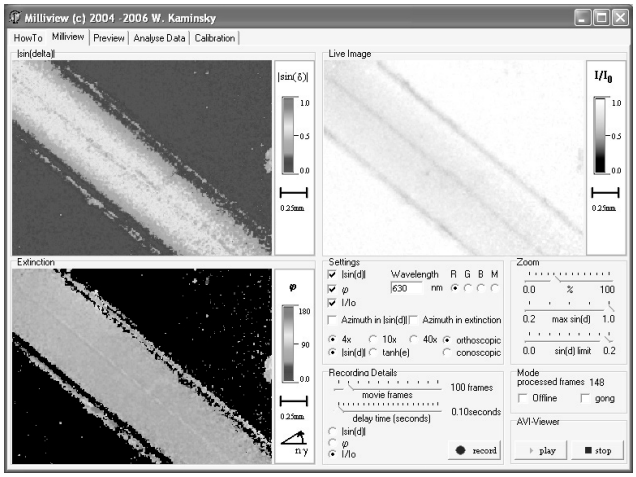

Figure 10: Milliview© Screenshot of Polymer Fiber (rectangular cross-section). Clockwise from top left: images of birefringence, relative intensity, settings/control panel, and extinction angle.

The software also has additional capabilities. For example, the software can record video files to demonstrate the changes in the image values (through changes in color along the gradient) as the sample stage is moved through the light source. The software can also create graphs of the values of interest (birefringence, extinction angle or the relative intensity). Both the device and the software are subject to patents pending.

This technology will allow birefringence measurements to be performed at a reduced cost compared to currently available commercial systems. Further work in this area will be done in Dr. Mescher's group in collaboration with Dr. Kaminsky to further develop and refine the system and its corresponding software.

References

1. Pedrotti, Frank L., S. J.; Pedrotti, Leno S. *Introduction to Optics*, 2nd Ed; Prentice-Hall: Saddle River, 1993; pp 501-502.

2. Polishuk, P., Plastic Optical Fiber Branches Out, Industrial Physicist (AIP), **2004**

3. Kuzyk, M. G.; Garvey, D. W.; Canfield, B. K.; Vigil, S. R.; Welker, D. J.; Tostenrude, J.; Breckon, C. *Chemical Physics* **1999***, 245*, 327-340.

4. Ji, P.; Li, A. D. Q.; Peng, G. In *Transverse birefringence in polymer optical fiber introduced in drawing process;* Kuzyk, M. G., Eich, M. and Norwood, R. A., Eds.; SPIE: 2003; Vol. 5212, pp 108-116.

5. van Eijkelenborg, M. A.; Argyros, A.; Barton, G.; Bassett, I. M.; Fellew, M.; Henry, G.; Issa, N. A.; Large, M. C. J.; Manos, S.; Padden, W. *Optical Fiber Technology* **2003***, 9*, 199-209.

Acknowledgments

Funds for this research were provided by the Center on Materials and Devices for Information Technology Research (CMDITR), and the NSF Science and Technology Center No. DMR 0120967. Special thanks to: Dr. Ann Mescher, Dr. Werner Kaminsky, Hien T. Pham, Gregory Winchell, University of Washington, Center for Materials & Devices for Information Technology Research; Kevin Soderlund for Fabrication of Device Housing and Templates, Bill Kuykendall for Technical Assistance, Russell Noe for Instructional Assistance; Administrative Staff, University of Washington, Mechanical Engineering; Dr. Suely Black, Dr. Carl Bonner, Norfolk State University, Center for Materials Research; Kristin Wustholz, Sara Selfe, Dr. Philip Reid, Dr. Glen Shen, Dr. Jeanne Small, and Janis Hill of CMDITR.Andrea N. Joseph is an undergraduate Physics major from Norfolk State University in Norfolk, Virginia.

Synthesis of "Retrofitted" Nonlinear Optical Dyes for use in Dye-Sensitized Solar Cells

Bonaire L. Le
Yale University

Dinesh G. Patel, Glenn P. Bartholomew
University of Washington

Introduction

The ongoing depletion and scarcity of fossil fuels has elevated the importance of an alternative energy source large enough to meet the growing demands of the human population. Current development of photovoltaic devices takes advantage of solar energy as a readily accessible global reservoir of power. While silicon based devices have proved to be most successful with their high efficiency, the cost to manufacture these devices is expensive and therefore unable to compete with the lower price of fossil fuels. The costly production of silicon-based solar cells has resulted in an increased interest to develop more economically appealing alternatives.

Dye-sensitized solar cells (DSSCs) are cost effective and promising alternatives to silicon-based photovoltaic devices.[1-3] The relatively inexpensive components of DSSCs consist of a semiconductor oxide film, a sensitizer dye, and a redox electrolyte (Figure 1). Studies have shown that the material of choice for the oxide film is TiO_2 over other oxides such as ZnO and Nb_2O_5.[1] A monolayer of sensitizer is absorbed onto the oxide film, which is placed in contact with a redox electrolyte or organic hole conductor.[1] Photoexcitation of the dye (S) allows for the injection of an electron into the oxide conduction band. The oxidized dye is reduced by the electrolyte, which in turn is regenerated at the cathode, thus completing the electronic circuit.[1-3] Alignment of the HOMO and LUMO of the dye sensitizer is crucial towards a functional DSSC. By principles of electrochemistry, electrons can transfer down while holes can shift up in energy levels. The sensitizer's HOMO must therefore lie at a lower energy level than that of the redox electrolyte and its LUMO must be at a higher energy level than that of the oxide film in order to allow for proper oxidations and reductions to take place within the cell.

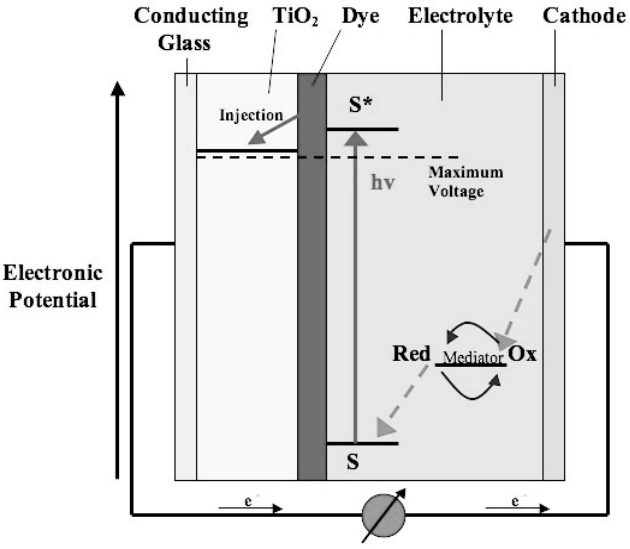

Figure 1. A diagram displaying the components of a DSSC with a TiO_2 as the semiconductor oxide film. Light is absorbed by the sensitizer dye (S), which, in its excited state, injects an electron into the oxide film. The sensitizer, now oxidized, is reduced by the electrolyte, which itself is regenerated at the counter electrode by returning electrons.

In pursuit of high efficiency (η) DSSCs, a number of dyes have been tested as sensitizers over the past 15 years.[4] Efficiencies of 10% have been reached but the cell suffers from a few drawbacks.[1] Specifically, the most efficient dye sensitizer is a relatively expensive ruthenium complex, with a moderate absorption coefficient at 520 nm; blue relative to solar flux maximum (700 nm).[1] Ruthenium-complexed dyes are known to have extinction coefficient values, ε, of ~13000 $m^{-1}cm^{-1}$, hindering the overall performance of the photovoltaic device due to the lack of photon absorption by the sensitizer. In addition, a corrosive liquid electrolyte is used as the hole transport layer, reducing the overall life of the solar cell.[1]

By "retrofitting" currently known nonlinear optical (NLO) dyes to allow for binding to TiO_2, a new homologous series of all-organic dyes exhibiting high absorption coefficients and improved spectral overlap with solar output prove

to be promising replacements for the Ru-complexed dye sensitizer.

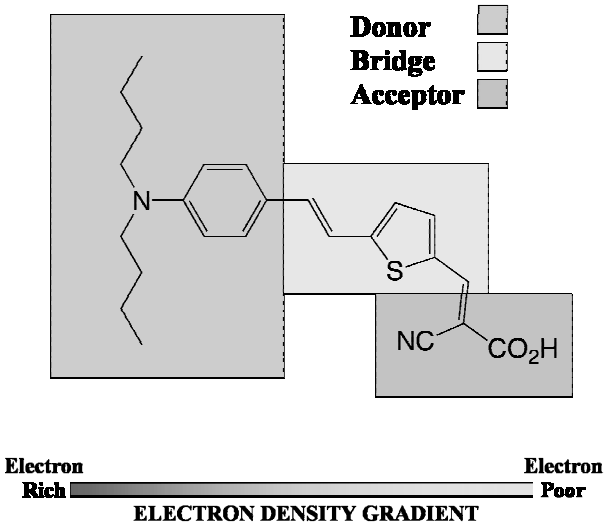

Figure 2. This diagram displays the three regions of the synthesized dye sensitizer. The electron rich donor and the electron poor acceptor create an electron density gradient throughout the molecule naturally pulling electrons from the donor into the acceptor, which binds to the oxide film with the carboxylic acid group.

The molecular design of the synthesized dye structurally optimizes the interactions between three distinct molecular regions: the donor, the bridge, and the acceptor (Figure 2). These regions follow the model of FTC type molecules used as optical dyes for nonlinear applications by Dalton and coworkers.[5,6] During excitation, the lone pair on the nitrogen in the donor allows for easy electron donation into the molecule. The thoiphene bridge and carbon-carbon double bond on either side act as a conjugated spacer, which shift the molecule's absorption towards the red region of the light spectrum. The placement of the carboxylic acid group in the acceptor anchors the molecule onto the TiO_2. Throughout the molecule an electron density gradient is present as the result of the electron rich donor and the electron poor acceptor regions. This gradient promotes charge separation, aiding in the transfer of electrons through the molecule during excitation, therefore naturally pulling electrons from a region of high density into one of low density where they can be passed into the metal oxide film.

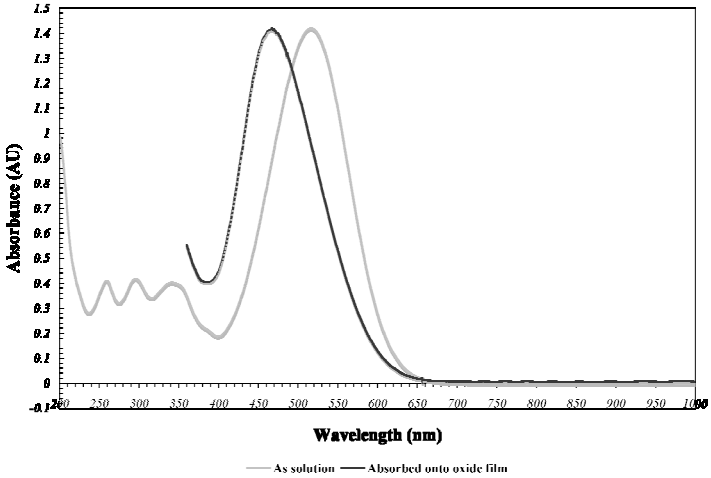

Figure 3. Normalized UV-Vis spectra for ASD as a 1.65 X 10^{-5} M solution in CH_3CN and absorbed onto TiO_2. ASD was absorbed onto TiO_2 by soaking in a 3 x 10^{-4} M ASD in dry ethanol solution for ~45 min. Analysis showed that λ_{max}(solution) = 516 nm, λ_{max}(solid) = 467 nm, ε = 44000, ΔE = 2.017 eV.

Results and Discussion

ASD was synthesized through a series of five reactions in good yield (Scheme 1). The purity of the dye sensitizer was confirmed by ^{1}H NMR and TLC.Results of UV-Vis spectroscopy allowed for comparison of the dye's absorption profile to the solar spectrum (Figure 3). Multiple samples were made for UV-Vis in progressively increasing concentrations, resulting in a maximum absorption at λ_{max} = 516 nm and extinction coefficient of ε = 44000 $m^{-1}cm^{-1}$. Upon absorption onto TiO_2 the

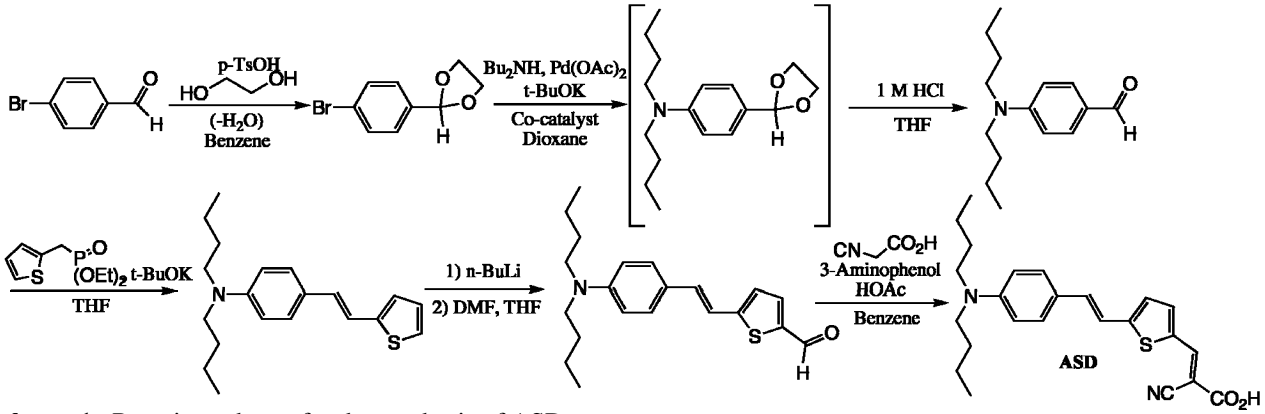

Scheme 1. Reaction scheme for the synthesis of ASD.

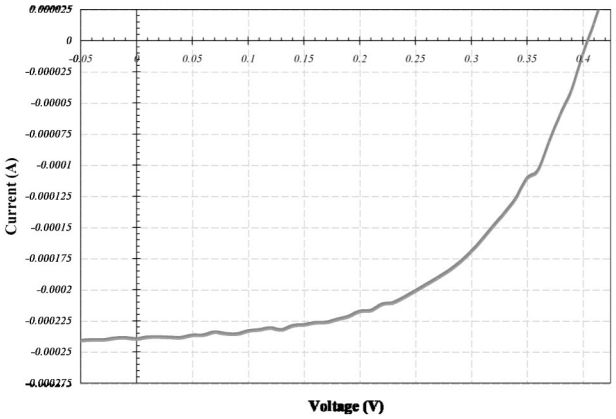

Figure 4. Photocurrent voltage curve of a DSSC with ASD absorbed onto TiO_2. The conversion efficiency in full AM 1.5 sunlight was 0.47%. At V = 0, I_{sc} = -0.239 mA and at I = 0, V_{oc} = 0.41.

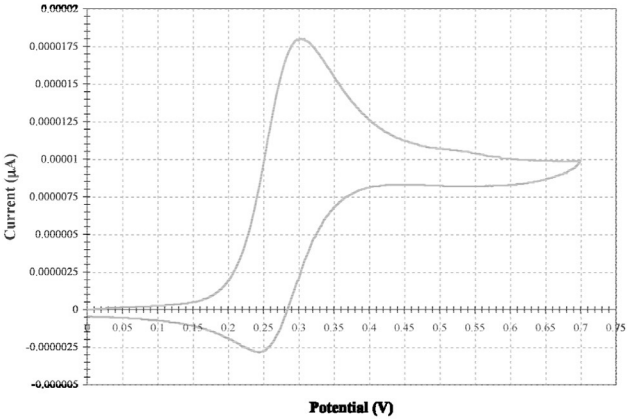

Figure 5. A Cyclic voltammetry plot displaying oxidation and reduction of ASD over a voltage potential ranging from 0 mV to 700 mV. The sample was prepared as a 2 x 10^3 M solution of ASD in 0.1 M $(Bu_4N)PF_6$ in acetonitrile.

maximum absorption of ASD became blue shifted at λ_{max} = 467 nm. The difference in energy between the HOMO and LUMO of ASD was calculated to be ΔE = 2.017 eV. Results of UV-Vis demonstrated a moderate improvement over Ru complexed dyes. While the values of λ_{max} for ASD and Ru-complexed sensitizers lie within the same region of the solar spectrum, ASD's extinction coefficient is at least 3 times greater than the ~13000 $m^{-1}cm^{-1}$ of the N3 Ru-based dye.[1]

Performance of the synthesized dye was assessed through a working nanocrystalline TiO_2 DSSC for spectral photovoltaic response and global efficiency under AM 1.5 illumination (Figure 4). The sensitizer dye was absorbed onto TiO_2 by placing a TiO_2 coated electrode in a 3 x 10^{-4} M solution of ASD in dry EtOH over night. The electrolyte injected into the DSSC was a mixture of 0.05 M I_2/ 0.5 M LiI / 0.5 M *tert*-butylpyridine in CH_3CN solution. The short circuit current, I_{sc}, was – 0.239 mA and the open circuit voltage, V_{OC}, was 0.41 V. The overall efficiency of the dye-sensitized cell is determined by the photocurrent density measured at short circuit (I_{sc}), the open-circuit photovoltage (V_{oc}), the fill factor of the cell (ff), and the intensity of the incident light (I_s).

$$\eta_{global} = i_{ph} V_{oc} (ff)/I_s \quad [1]$$

With a calculated ff = 0.53, I_s = 1000 W cm^{-2} for 1.5 AM illumination, and an aperture opening of 0.11 cm^2, the efficiency of ASD under our experimental conditions was determined to be η = 0.47 %.

Cyclic voltammetry was employed to compare the dye's HOMO and LUMO levels with respect to those of the TiO_2 conduction band and the electrolyte-shuttle's redox potential (Figure 5). The CV sample was prepared as a 2 x 10^{-3} M solution of ASD in 0.1 M $(Bu_4N)PF_6$ in acetonitrile. Parameters were set to V_i = 0 mV, range of potential: 0 mV – 700 mV, and scan rate of 20 mV/s. Cyclic voltammetry measurements showed that the energy levels of the HOMO and LUMO of ASD were at –4.973 eV and –2.956 eV respectively.

It is suspected that the HOMO and LUMO of the sensitizer are not aligned properly with those of the redox electrolyte and the conduction band oxide. Misalignment of energy levels within a DSSC is one the possible factors effecting the sensitizer's performance. Without ASD's LUMO at an equal or higher energy level than the that of the conduction band, and its HOMO at a lower energy level than that of the electrolyte, the energy level alignment of the dye, the oxide, and the electrolyte would not be condusive towards a functioning DSSC.

Despite its high extinction coefficient, a three fold improvement over that of the Ru-based N3 dye, ASD's photovoltaic performance is much lower than the 10% Ru-based sensitizers have achieved when tested in a DSSC.[1] It was hypothesized that the dipole nature of ASD caused aggregation, aligning molecules anti-parallel to each other. Aggregation of the dye would limit the efficiency of the electron transfer into the semiconductor oxide film, hindering the overall photovoltaic performance of ASD and explaining ASD's low η value.

Amount ASD (mg)	Molarity	λ_{max} (nm)	Absorbance (AU)	Solvent
2.5	1.958*10^(-5)	515	0.79002	CH_3CN
2.1	1.645*10^(-5)	516	0.59243	CH_3CN
1.8	1.410*10^(-5)	516	0.50893	CH_3CN
1.5	1.175*10^(-5)	516	0.38572	CH_3CN
0.9	7.049*10^(-6)	514	0.24874	CH_3CN
1.5	1.175*10^(-5)	509	0.52552	EtOH
1.5	1.175*10^(-5)	542	0.63691	$CHCl_3$

Figure 6. A comparison chart of UV-Vis data for ASD in multiple concentrations and a variety of solvents.

However, further UV-Vis spectroscopy showed that maximum absorption was relatively constant around λ_{max} = 516 nm with respect to increased and decreased concentrations of ASD in acetonitrile (Figure 6). Because of this lack in shift of λ_{max} through varying concentrations of ASD in CH_3CN, the presence of aggregation between ASD molecules is eliminated as factor hindering the performance of the sensitizer in the DSSC.

Due to multiple λ_{max} obtained through the analysis of ASD UV-Vis spectra in a variety of solvents, the solvatochromism of ASD was assessed. Solely considering the λ_{max} of ASD in aprotic solvents (CH_3CN and $CHCl_3$), ASD demonstrates negative solvatochromism, which lends to the fact that during photoexcitation, ASD is promoted from a polar ground state into a less polar excited state. The solvatochromism of ASD confirms its charge-separated state which results from its structural electron density gradient.

Conclusions

The synthesis of ASD resulted in an anchorable dye that absorbs well in the visible region and exhibits a high extinction coefficient approximately 3 times greater than those of Ru-based coordination complexes. UV-Vis spectral analysis exhibited ASD's maximum absorption at λ_{max} = 516 nm with an extinction coefficient of ε = 44000 $m^{-1}cm^{-1}$. Cyclic voltammetry demonstrated HOMO and LUMO energy levels of ASD at – 4.973 eV and – 2.956 eV respectively. DSSC testing showed the performance efficiency of ASD to be η = 0.47%. Upon further analysis, it was hypothesized that the cause of ASD's low global efficiency, despite its high absorption abilities, was due to the misalignment of its HOMO and LUMO energy levels with those of the metal oxide film and the hole transport layer. Future synthesis of similar dyes will focus on obtaining better alignment of the HOMO and LUMO levels of the sensitized dye with those of the semiconductor oxide film and redox electrolyte. Energy level alignment may involve modifying the type of oxide and electrolyte utilized in the DSSC in addition to electron density modifications of the donor and acceptor regions. The optimization and engineering of a surface anchorable dye sensitizer will beneficially lead to the development of a more efficient and cost effective photovoltaic alternative to silicon based solar cells.

References

1. Grätzel, M.; *Inorg. Chem.* **2005**, 44, 6841-6851.
2. Tae, E. T.; Lee, S. H.; Lee, K. L.; Yoo, S. S.; Kang, E. J.; Yoon, K. B.; *J. Phys. Chem. B* **2005**, 109, 22513-22522.

3. Ito, Seigo; Zakeeruddin, S. M.; Humphry-Baker, R.; Liska, P.; Charvet, R.; Comte, P.; Nazeeruddin, M. K.; Péchy, P.; Takata, M.; Miura, H.; Uchida, S.; Grätzel, M.; *Adv. Mater.* **2006**, 18, 1202-1205.
4. Spanggaard, H.; Krebs, F. C.; *Solar Energy Materials & Solar Cells* **2004**, 83, 125-146.
5. Wang, F.; Ren, A.S.; He, M.; Lee, M. S.; Harper, A. W.; Dalton, L. R.; Zhang, H.; Garner, S. M.; Chen, A.; Steier, W. H.; *Polym. Prepr.* (*Am. Chem. Soc., Div. Poly. Chem.*) **1999**, 39, 1065-1066.
6. Wang, P.; Zakeeruddin, S. M.; Moser, J. E.; Nazeeruddin, M. K.; Sekiguchi, T.; Grätzel, M.; *Nat. Mater.* **2003**, 2, 402-407.

Acknowledgments

Special thanks to Dinesh Patel and Glenn Bartholomew for their greatly valued knowledge, guidance, and support. Many thanks to all the members of the Bartholomew Group for use of their lab and for their companionship. Funds for this research were provided by the Center on Materials and Devices for Information Technology Research (CMDITR), and the NSF Science and Technology Center No. DMR 0120967.

Bonaire Le is currently completing his undergraduate studies at Yale University. In May 2009 he will obtain an ABET accredited B.S. in Chemical Engineering.

Measuring Inverse Piezoelectric Effect in Electro-optic Polymers with WYKO Interferometer

Beth Martine
University of North Texas

Haiyong Gan, Mahmoud Fallahi, and Robert A. Norwood
Fallahi Lab, College of Optical Science
University of Arizona

Introduction

An inverse piezoelectric effect occurs when voltage is applied across the surface of solid and the surface undergoes a deformation. The piezoelectric effect, along with the electro-optic effect, contributes to the performance of Fabry-Pérot étalon devices. The electro-optic (EO) effect is a change in the index of refraction due to an applied electric field. The piezoelectric effect is used in Fabry-Pérot étalon devices for high-speed data transmission. Key components in the improvement of Fabry-Pérot étalons involves (i) high finesse, (ii) large tenability, (iii) high speed, (iv) wide tunable range, and (vi) understanding the mechanics of both the electro-optic and piezoelectric effects. This researched explored the behavior of the piezoelectric effect.

Device

Fabry-Pérot étalons are structures made with layers of indium tin oxide (ITO), a highly reflective (>99%) mirror called a Distributed Bragg Reflector (DBR) and the electro-optic (EO) polymer.

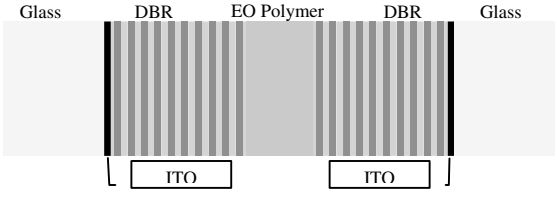

Figure 1- Fabry-Pérot Étalon Schematic

As light moves through the cavity, resonance due to the internal reflection between the DBR mirrors cause interference in the waves, canceling out frequencies of light until only specific wavelengths emerge.

Fabry-Pérot étalons are frequently used in data transfer and have functions in optical switches, tunable filters, and modulators. The essential difference between the two effects is the speed. The piezoelectric effect is moderately fast working in the 10^{-6} to 10^{-3} second range, making it ideal for applications in tunable filters and wavelength switch matrices. The electro-optic effect, operating at about 10^{-12} seconds for transmitting information, is extremely important for high speed spatial light modulators and ultra fast switch matrices.

Material

Most Fabry-Pérot étalon use the EO polymer AJL8/APC, yet in this research a material similar to AJL8 was used: AJLS102. The polymer is just one of the layers in the sample.

The first layer deposited on the substrate glass is ITO, a transparent substance acting as an electrode. Then the electro-optic polymer is spin coated onto the ITO, followed by a barbell shaped gold conductive material layered on top. The gold is useful since it is both conductive and reflective. After baking, the sample is poled above the glass transition temperature (degree at which molecules have little mobility) and at a high voltage. The purpose of poling is to orient all the molecules of the polymer into the same direction. After poling,

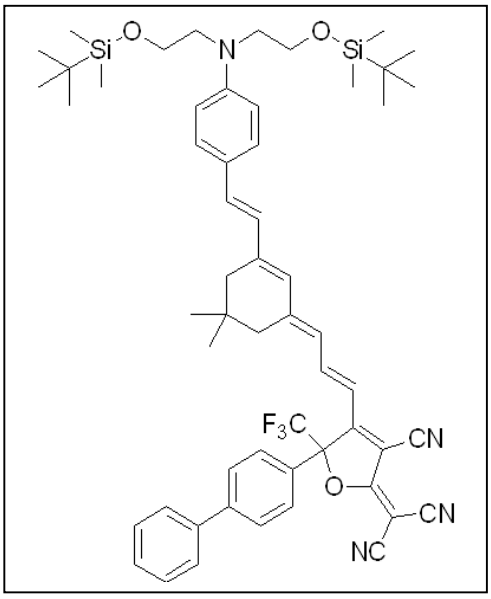

Figure 2- AJLS102

wires are secured to the sample so that voltage can pass through. One wire attaches to the conductive gold material and the other connects to the EO polymer. Scratches were placed on the slide to get a clear measurement of the height difference from the top of the sample to the bottom. The scratch takes off a portion of the ITO and EO polymer layers, leaving the unchanging glass surface. Only the areas with polymer can alter as a result of the piezoelectric effect.

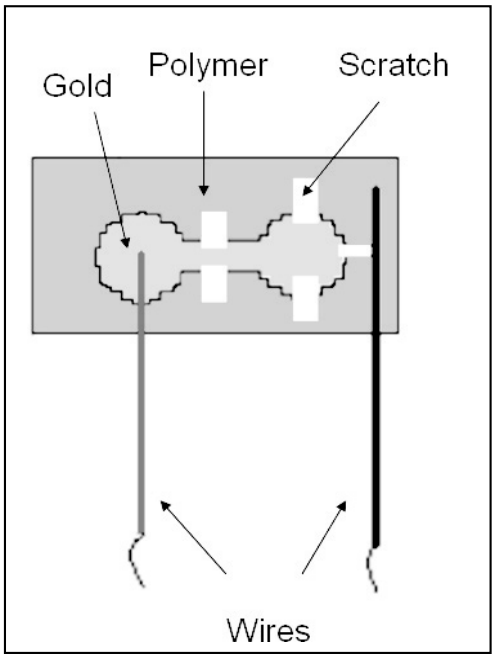

Figure 3- Sample Schematic- Vertical View

Methods

The piezoelectric effect is measured using a WYKO Interferometer which scans the sample surface using light interference patterns. The sample is taped to the WYKO stage to prevent movement vibrations. The wires are connected to a high voltage amplifier and a voltmeter. The viewing area is set at a scratch edge so as to have half of the area being the gold surface and the other half having the glass surface. As measurements are taken by the WYKO at voltages of -10, -5, 0, 5, and 10, the glass layer remains the same while the gold layer moves. This changing height is the piezoelectric effect. After processing the data, the degree to which the surface changed per volt can be determined.

WYKO Interferometer

The WYKO interferometer has two modes of measurement: Phase Shifting Interferometry (PSI) and Vertical Scanning Interferometry (VSI). The differences between the options are the conditions of filtering the white light from its source and the part of the fringe that is measured. PSI filters the white light whereas the VSI does not. PSI also measures the phase of interference. This research used the VSI mode which measured the degree of fringe coherence.

Inside the machine, a source shines white light horizontally to a beam splitter that directs the light to the stage. The light goes through a converging lens that directs the rays towards a single point that will be focused on the sample. After going through the lens, the light hits another beam splitter that redirects part of the rays to a reference mirror while leaving the remaining wave to pass through the beam splitter and to hit the surface in a pinpoint of light approximately one millimeter in diameter. The light reflecting off of the sample and the reference mirror meet back at the beam splitter creating fringes. The light then proceeds upward into the CCD camera where the image is displayed on a screen. The screen shows the fringes made from interference

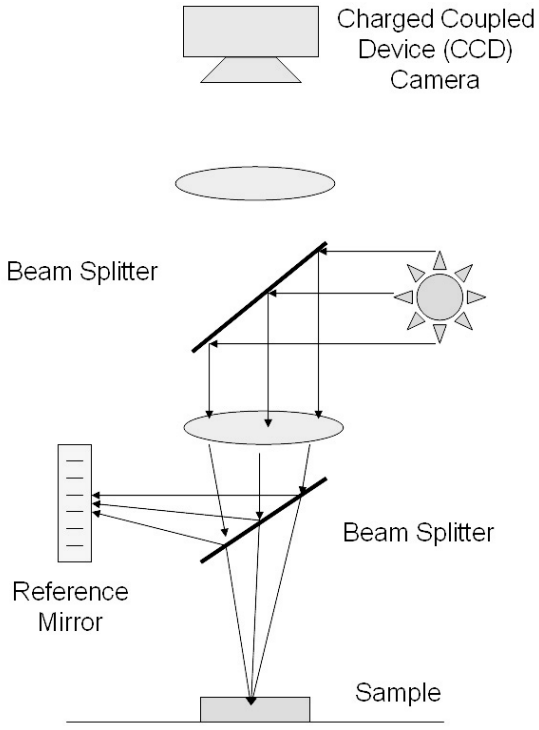

Figure 4- WYKO Schematic

waves. Constructive and destructive interference occurs by which opposing waves cancel out- making black and white fringe lines. When the distance from the reference mirror to the beam splitter equals the distance from the sample surface to that same beam splitter, then shown on the screen is a set of fringes with the most contrasting white and black shades. This is the moment where the interferometer has the best focus on the surface and is the opportune moment to measure.

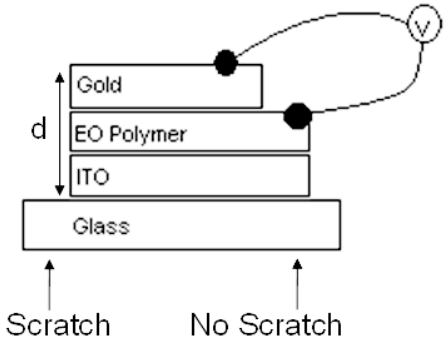

Figure 5- Sample Schematic- Vertical View

Results & Discussion

The WYKO measures the height difference between the bottom glass layer and the top gold layer. This distance is d. With the EO polymer rising up and down as voltage is applied, the amount of change the electro-optic material undergoes per volt is found. This change from 0 volts is •d. Before calculating the change in thickness, the data curves were normalized and combined together in one graph.

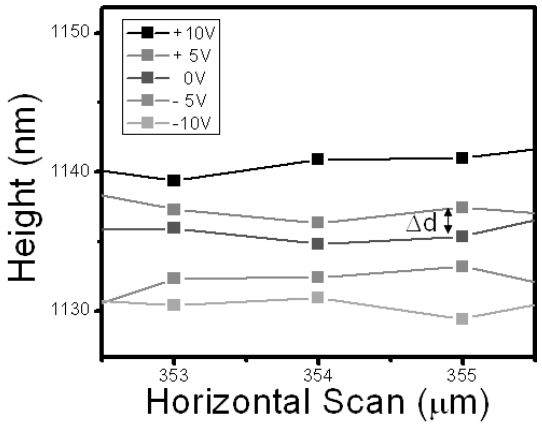

Figure 6- Surface Shift Results

Analyzing the data from Figure 6, it is noted that for 20 volts, there is movement over about 10 nm. Therefore the change in height is about -0.5 nm/V. This is the amount of shifting done on the EO polymer due to the piezoelectric effect. With this information, the degree of shifting due to the electro-optic effect in Fabry-Pérot étalons can be determined by the following equation.

$$\frac{\Delta\lambda}{\lambda} = \frac{\Delta d}{d} + \frac{\Delta n}{n}$$

Equation 1

The lambda term is the wavelength shifting in Fabry-Pérot cavities, which is composed of the piezoelectric effect and the EO effect. The piezoelectric effect has a change in distance, so it is the middle term and the EO effect involves a

change in the refractive index, making it the ending term.

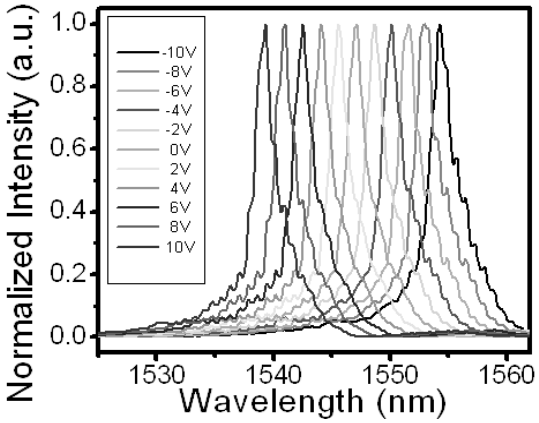

Figure 7- Wavelength Resonance Shift in a Fabry-Pérot etalon.

Conclusion

This research used a new technique of using the WYKO interferometer to directly measure the inverse piezoelectric effect. It was able to isolate the inverted piezoelectric effect from the electro-optic effect, which has a shift of -0.5 nm/V. This is a part of the amount of wavelength shift. Determined from previous work, there is a -0.35 nm/V shift for the EO polymer AJL8/APC and a -0.75 nm/V shift for TCBD/Sol-gel materials. These measurements included the voltage applied across two DBR mirrors and the polymer whereas this research applied the voltage only across the polymer, meaning that the amount of voltage that reaches the polymer after passing through the mirrors is decreased from the initial voltage reading. This has helped to gain a better understanding of the piezoelectric effect which can improve Fabry-Pérot etalons in order to advance the rate of accessing information in a majority of data transmission devices.

Future Work

More research is being performed to improve the speed of data transmission through Fabry-Pérot devices. Developing better parts of the Fabry-Pérot, such as increasing the reflectivity of DBR mirrors, is a step in achieving that goal.

References

1. H. Gan, H. Zhang, C. T. DeRose, R. A. Norwood, N. Peyghambarian, and M. Fallahi, Applied Physics Letters 89, 41127, July 2006.
2. University of Arizona College of Optical Sciences Class Notes. http://www.optics.arizona.edu/jcwyant/Optics505(2000)/ChapterNotes/Chapter07/multiplebeaminterference.pdf (accessed June 20, 2006)
3. B. Eby, H. Gan, H. Zhang, M. Fallahi, "Electro-Optic Properties of Hybrid Sol-Gel Materials in Fabry-Perot Modulators", REU 2005 summer report.

Acknowledgemente

Christopher DeRose, Charles Greenlee, Robert Kester, Jeremy Rogers, National Science Foundation, University of Arizona, College of Optical Science

Funding for this research was provided by the NSF Science and Technology Center on Materials and Devices for Information Technology Research, No. DMR 0120967

Personal Statement

Beth Martine is an undergraduate at the University of North Texas. She plans to graduate with a Chemistry Bachelor of Science degree and proceed to graduate school where she will earn her PhD.

Synthesis of a Chromophore Bridge Component and an Active Hyper-Branched Polymer Host for Chromophore Doping

Tiffany D. Mealman,
Seattle Pacific University

Philip A. Sullivan, Larry R. Dalton,
University of Washington

Introduction

This work demonstrates the synthesis of a chromophore bridge component and an active host hyper-branched polymer. The bridge component, functionalized benzothiadiazole, is synthesized to be incorporated into a donor-bridge-acceptor chromophore or to be altered for further chromophore synthesis. The hyper-branched polymer is synthesized to be utilized as an active host material for chromophore doping. Hyperpolarizability (β) of individual chromophores will be determined, as well as the r_{33} of the bulk materials.

Research incorporating organic materials into 2nd-order nonlinear optical (electro-optic) applications has increased greatly in recent years due to the ability of these materials to improve the performance and cost of telecommunications, computing and numerous other applications. The basic role of electro-optic (EO) material is to serve as electrical-to-optical signal transducers, also called EO modulators. The EO modulator acts as an optical switch, translating digital or analog electrical signals into optical signals and back into electrical signals again.[1] Nonlinear optical effects change the way in which electromagnetic radiation interacts with materials, thus changing the properties of the materials. An important material property of specific interest is index of refraction. Nonlinear optical effects can be described by refractive index modulation induced by an electric field. The refractive index of a material, its linear polarizability and dielectric constant at optical frequencies are all directly related. A major focus in the characterization of chromophores (nonlinear optic dyes) is optical susceptibility, $\chi^{(n)}$, which defines the propagation medium polarization response to an incident optical field. For a linear electric field, polarization (P) is defined by equation 1.

$$P = \chi^{(1)} * E \quad \text{(Equation 1)}$$

In this equation $\chi^{(1)}$ represents the linear optical susceptibility and E corresponds to the amplitude of the optical field. In nonlinear optics, higher order polarization is achieved and thus higher order nonlinear optical susceptibilities are included, see equation 2.

$$P = \chi^{(1)} * E + \chi^{(2)} * EE + \chi^{(3)} * EEE + \ldots \quad \text{(Equation 2)}$$

In the above equation, $\chi^{(2)}$ for individual chromophore molecules can be expressed as the second-order polarization response to the electric field, also known as β, the hyperpolarizability. Along with β, r_{33} (electro-optic coefficient) values of these chromophores can be analyzed in order to determine the magnitude of change in refractive index with respect to the applied electric field.[1]

Target chromophores are typically constructed in the form of a donor-bridge-acceptor architecture, as seen in **Figure 1**.

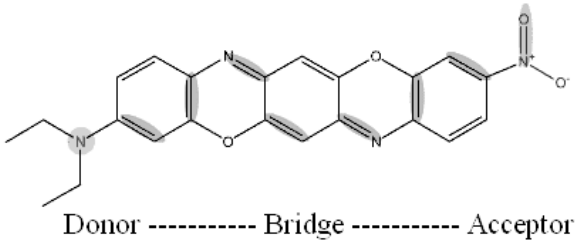

Figure 1. Typical donor-bridge-acceptor chromophore architecture

The donor is an electron rich molecule; the bridge is an inert molecule, and the acceptor is an electron poor molecule, thus creating an overall structure with the necessary electron density asymmetry to move electrons, as demonstrated in **Figure 2**. The main goal is to synthesize super-donor/super-acceptor type molecular-orbital architecture with an active bridge in hopes to spatially localize the HOMO and LUMO, increasing dipole moment,

reducing band gap, and increasing hyperpolarizability.[2]

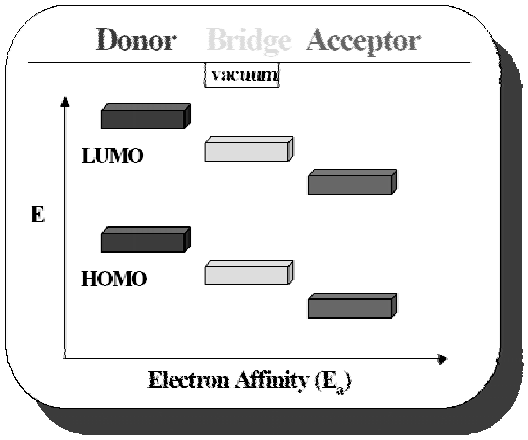

Figure 2. Electron affinity gradient of HOMO and LUMO of a chromophore

Synthesis of functionalized benzothiadiazole, an electron-poor bridge component, for the incorporation into a donor-bridge-acceptor chromophore, as shown in **Figure 3**, will engender an electron affinity gradient by enhancing the ground-state electron-density asymmetry, creating a "super-donor/super-acceptor" effect.

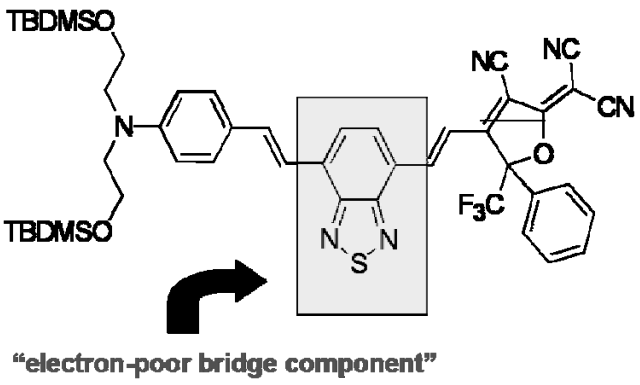

Figure 3. Benzothiadiazole bridge component to be incorporated into a chromophore structure

Chromophores are typically dispersed into transparent host polymer materials which are then poled by a strong DC poling field. The molecular dipole orientation of the chromophores change due to the applied electric field during poling, as illustrated in **Figure 4**.[3-6]

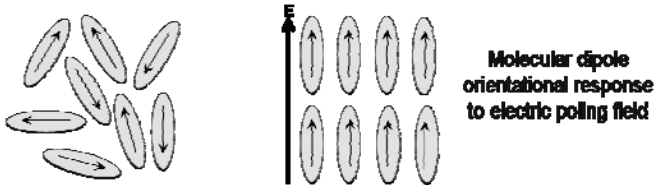

Figure 4. Chromophore molecular dipoles orient in response to an applied electric poling field

The hyperpolarizability (β) of individual chromophores and the r_{33} value of the bulk materials can be determined through poling. A few problems arise during poling: difficulty maintaining homogeneous conditions between the guest-host composite material, low thermal stability, and interchromophore electrostatic interactions. The later is the main focus of this work; **Figure 5** illustrates this dipole interaction.[7-9]

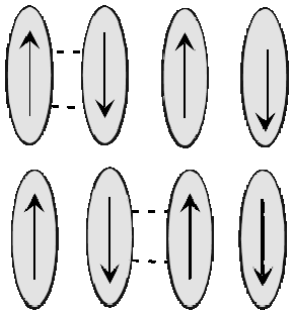

Figure 5. Interchromophore electrostatic interactions cause dipole flipping during poling

The incorporation of hyper-branched polymers decreases the electrostatic interactions between chromophores by increasing the steric bulk around the chromophore; hyper-branched polymers also have the potential for increased chemical and thermal chromophore stability. Previous research has shown that higher r_{33} values are obtained when chromophores are doped into an active hyper-branched polymer as apposed to an inactive polymer. Synthesis of the active hyper-branched polymer in this work will provide a host for chromophore doping and result in more favorable r_{33} values for the bulk material.

Results and Discussion

Synthesis of a functionalized benzothiadiazole bridge component is carried out using the following synthetic pathway illustrated in **Scheme 1**.

Scheme 1. Synthesis of functionalized benzothiadiazole bridge component[10]

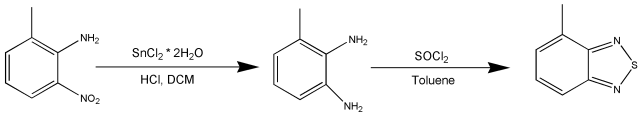

Synthesis of active hyper-branched polymer host materials is carried out by the following synthetic pathway, as shown in **Schemes 2** and **3**.

Scheme 2. Synthesis of alcohol reagent for active hyper-branched polymer host

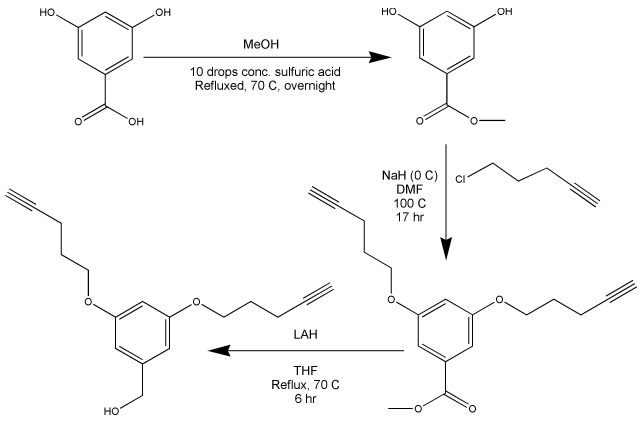

Scheme 3. Synthesis of ester reagent for active hyper-branched polymer host

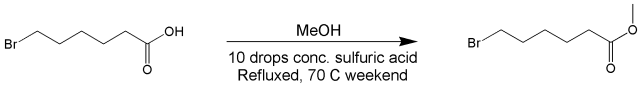

NMR spectra acquired on a 301 MHz machine are obtained for synthetic products to confirm success of synthesis and are illustrated in **Figures 5-7**. Products synthesized in **Scheme 2**, the alkylated ester and alcohol, show peaks in the aromatic region around 7.0 ppm, representative of the three aromatic protons. Both structures also display peaks around 4.0 ppm and the region between 1.8 - 2.5 ppm, representative of the alkyl group protons. The ester displays a peak at 3.8 ppm representative of the methyl group protons which are shifted downfield due to the shielding caused by the adjacent oxygen. The alcohol shows a peak at 4.5 ppm representative of the two protons shifted downfield by the shielding of the oxygen of the hydroxyl group.

Peaks at 3.5 ppm, for the product synthesized in Scheme 3, are representative of the three methyl protons on the ester. The peaks at 3.3 ppm are due to the protons shifted downfield because of shielding from the bromine. The peaks at 2.2 ppm represent the two protons shifted slightly downfield due to shielding from the carbonyl group. The peaks between 1.3 – 1.8 ppm are representative of the other alkyl protons.

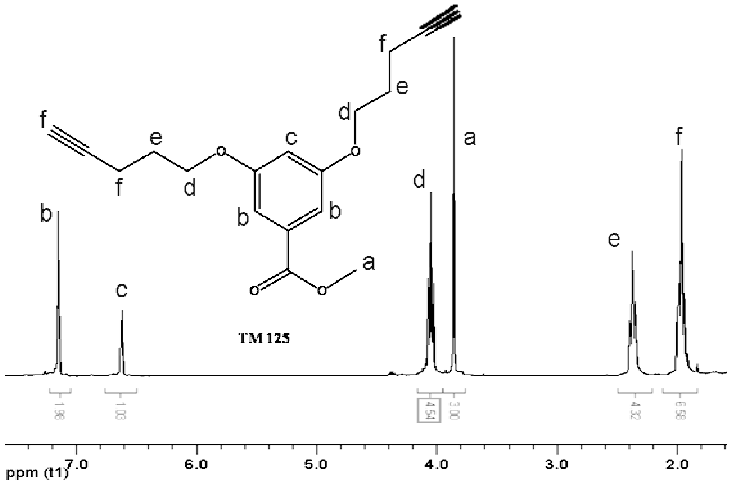

Figure 5. NMR spectra of **Scheme 2** intermediate

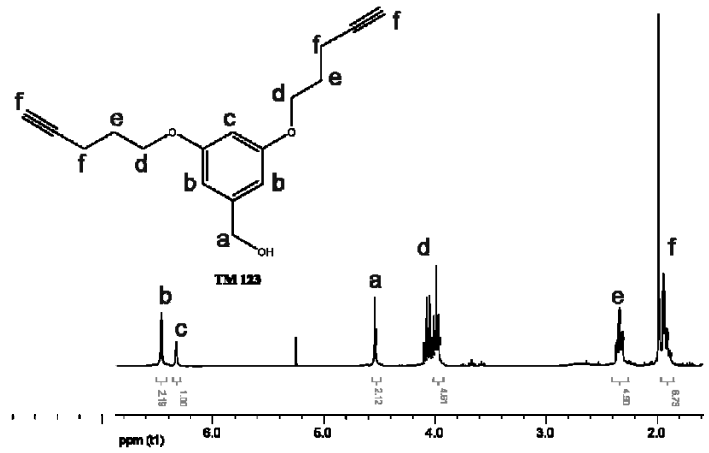

Figure 6. NMR spectra of **Scheme 2** product

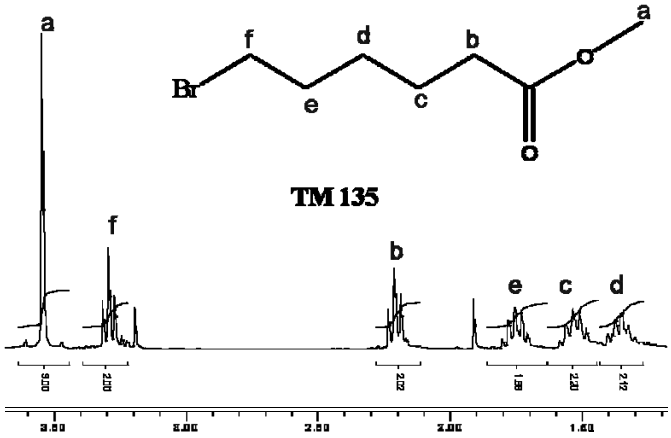

Figure 7. NMR spectra of **Scheme 3** product

Conclusions

Synthetic products of **Scheme 2** and **Scheme 3** will be coupled to produce a structure, shown in the pathway below, **Scheme 4**, which will then be coupled with chromophore disperse red 1 (DR1). This polymer structure is now "active" because it contains DR1, a chromophore which responds to the applied electric poling field. Next, a hyper-branched polymer will be synthesized by coupling the polymer with the following ether, resulting in the final structure below. "R" represents alternate places on the ether where there is potential for the polymer to attach.

Scheme 4. Synthesis of the active hyper-branched polymer host

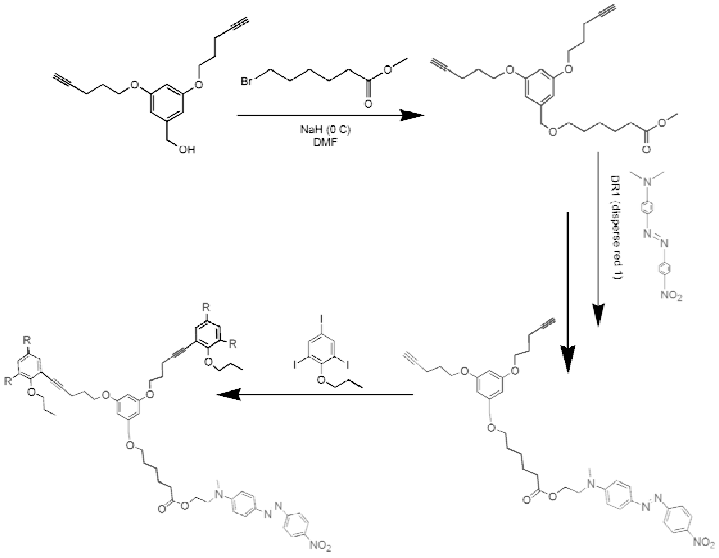

References

1. Sullivan, P.A.; Akelaitis, A.J.P.; K., L.S.; McGrew, G; Lee, S. K.; Choi, D. H.; Dalton, L.R. *Chem. Mater.* **2006**, 18, 344-351.

2. Dalton, L.D. *Advances in Polymer Science* **2002**, 158, (Polymers for Photonics Applications I), 1-86.

3. Ma, H.; Chen, B.; Sassa, T.; Dalton, L.R.; Jen, A. K-Y. *J. Am. Chem. Soc*., **2001**, 123, 986-987.

4. Luo, J.; Ma, H.; Haller, M.; Jen, A. K-Y.; Barto, R. R.; *Chem. Commun*. **2002** 888-889.

5. Chasse, T.L.; Sachdeva, R.; Li., Q. ; Petrie, R.J. ; Gorman, C.B. *J. Am. Chem. Soc.,* **2003**, 125,8250-8254.

6. Furuta, P.; Frechet, J.M.J. *J. Am. Chem. Soc.,* **2003**, 125, 13173-13181.

7. Frechet, J.M.J.; Hawker, C.J.; Gitsov, I.; Leon, J.W. *Journal of Materials Science-Pure Appl. Chem*. **1996**, A33(10), 1399-1425.

8. Cha, S.W.; Choi, D. H.; Jin, J-I. *Adv. Funct. Mater.* **2001**, 11 (5), 355.

9. Bai, Y.; Song, N.; Gao, J.P.; Yu, G.; Sun, X. ; Wang, X. ; Wang, Z.Y. *J. Am. Chem. Soc*., **2005**, 127, 2060-2061.

10. Jorgensen, M.; Krebs, F.C. *J. Org. Chem*. **2005**, 69, 6688.

Acknowledgments

Funds for this research were provided by the Center on Materials and Devices for Information Technology Research (CMDITR), and the NSF Science and Technology Center No. DMR 0120967.

A special thank you to Philip A. Sullivan for his mentorship and guidance. Thank you to Joshua A. Davies and Samy Elangovan for their help. I must acknowledge Larry R. Dalton and the entire Dalton Research group for their support, help and advice.

Personal Statement: Tiffany Mealman will be graduating from Seattle Pacific University in the spring of 2007 with a B.S. in Chemistry. She plans to begin graduate school in the fall of 2007 and get a Ph D. in Chemistry with the intent to eventually teach.

Third Harmonic Generation in Photonic Crystal Fibers Filled with Nonlinear Organic Materials

Katia Shtyrkova, University of Arizona *Robert A. Norwood, University of Arizona*

Introduction

Solid state lasers are being used in a variety of ways, including fiber optics communication systems, optical data storage devices and various electronic products.There are numerous challenges in developing compact solid state lasers that will operate at shorter wavelengths (less than 0.6 microns). One way to solve this problem is to use non-linear optical properties of certain materials to convert low frequency light to higher frequencies. While efficient materials for second harmonic generation have been in commercial use for decades, efficient direct third harmonic generators have been difficult to find.

Several materials have been identified as promising candidates for efficient third harmonic generation (THG) of the incoming wave. By using those materials it is possible to convert conventional 1550 nm wavelength to 517 nm. A thin film made out of those materials can produce green light visible to the naked eye when exposed to 1550 laser beam, and thin films have been used to perform advanced ultrashort pulse diagnostics such as frequency resolved optical gating (FROG). However, for significant applications there must be a method for making this process very efficient, that is, we should be able to find a way of significantly increasing the intensity of the generated green beam.

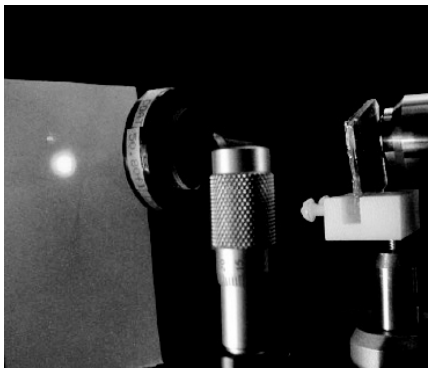

Figure 1. Current STC state-of-the-art THG film (Kippelen, et. al.)

One way of doing it is to use photonic crystal fibers (PCF) filled with highly non-linear materials. Such fibers have internal microstructure that allows for the manipulation of the light to simultaneously achieve low optical loss at the pump (1550nm) and third harmonic (517nm) wavelengths, while also providing enough control over the fiber dispersion to achieve phase matching over long lengths. This way when 1550 beam is coupled into the fiber, it will be largely confined in the non-linear material, which, provided there exists efficient phase matching of the fundamental and THG beams, can generate high intensity third harmonic.

Figure 2. Air core holey fiber (University of Southampton)

The goals of this research are:

- to choose photonic crystal fibers with the appropriate microstructure to be potentially filled with non-linear organic materials;
- to choose materials that can generate efficient third harmonic;
- to optically characterize the above materials in order to determine which ones are suitable for the fiber THG devices.

Methods and Results

Photonic Crystal Fiber

Commercially available photonic crystal fibers are available with a great variety of geometries and properties. Two main categories include high index guiding fibers and low index guiding fibers. High index guiding fibers trap the light in a solid

core by total internal reflection (like conventional fibers). Low index guiding fibers trap the light by the photonic bandgap effect (a property of the microstructure that makes propagation of certain wavelengths impossible in a holey region). Most fibers are made to allow only a particular wavelength to propagate within the fiber with minimal losses, often popular telecommunications wavelengths such as 1550nm or 1310nm. The long term purpose of this research is to fill the fiber holes with certain viscous materials; therefore, the wavelength for which the fiber is designed is at present irrelevant to our criteria of choosing the fiber. Various fiber geometries have been studied and compared in order to find the ones that could be filled most easily.

1. HC19-1550-01 is a hollow core fiber with the largest core diameter available on the market. The hollow core is surrounded by the microstructure of holes that influence the propagation of light within the fiber.

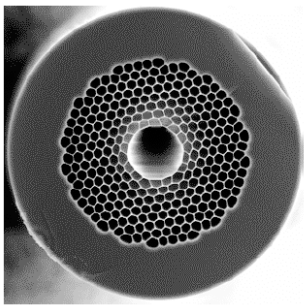

Figure 3. HC19-1550-01 fiber (crystal fiber)

2. NL-2.5-810 is a solid core fiber with a honeycomb holey structure. This fiber is designed to propagate light at 810 nm, however, it was chosen because of the largest diameter of microstructured holes.

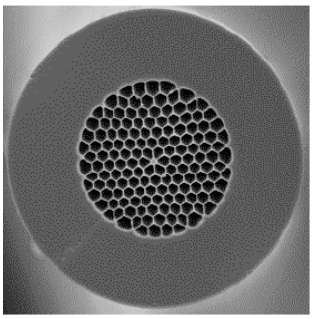

Figure 4. NL-2.5-850 fiber (Crystal Fibre)

Materials

1. Eight different dyes have been chosen initially from screening of the literature because of their potential to having reasonably high [(3)] values, good thermal stability for processing and good optical transparency at the target wavelengths. One aspect of our approach is that we will rely on long propagation lengths in the PCF to achieve efficiency, so very high [(3)] is not required.
2. Thin films with various dye concentrations have been made using the base of PATPD polymer and ECZ plasticizer by both spin coating (0.1-0.2 μm) and melt processing (20-70 μm).
3. Transmission spectra in the range of 200-2000 nm and refractive index measurements of those films have been taken and analyzed. The materials that will later be used to fill the fibers must have at least 75% transmission in both 1550 and 517 nm range in order to have the potential for efficient THG..
4. Concentration of the dye was reduced when appropriate in order to get better transmission at the desired wavelength.

Spin-coated films data (see Figure 5):

- all dyes exhibited good transmission at 1550 nm
- all dyes exhibited good transmission at 517 nm

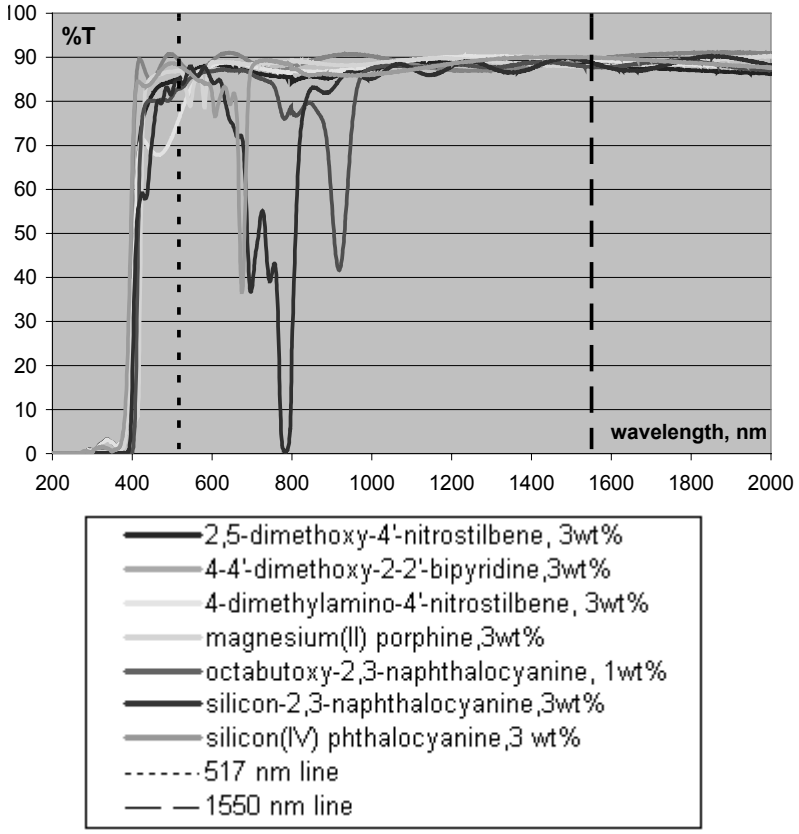

Figure 5. %T data on spin-coated films

Melt-processed films (see Figure 6):

- Most dyes exhibited good transmission at 1550 nm
- Only three out of eight dyes exhibited good transmission at 517 nm

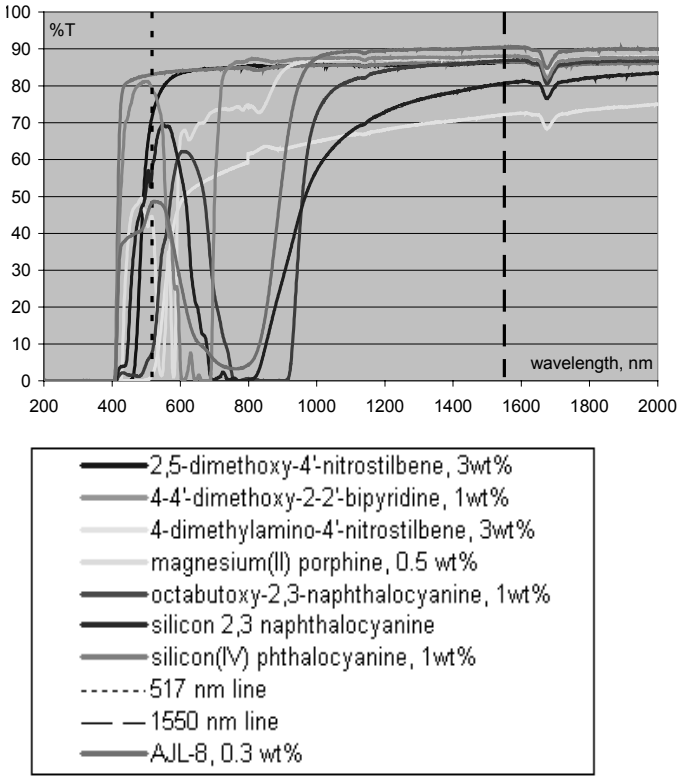

Figure 6. %T data on melt-processed films

It is clear from Figure 6 that there are only three dyes that have transmission above 70% when measured in melt-processed films:

1. 2,5-dimethoxy-4'-nitrostilbene

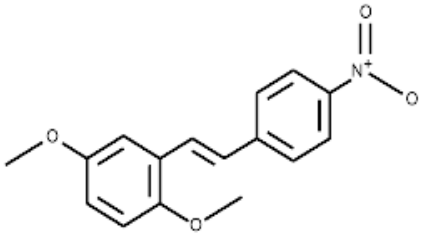

2. 4-4'-dimethoxy-2-2'-bipyridine

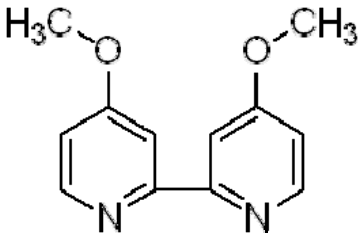

3. solubilized silicon(IV) phthalocyanine

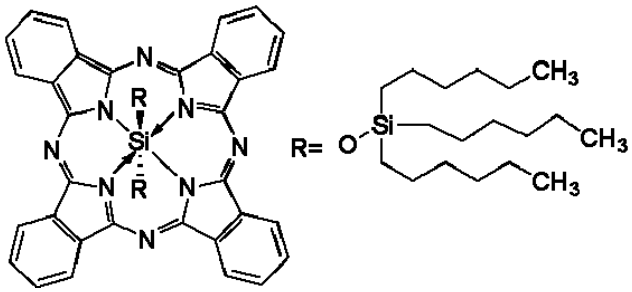

These dyes can be used to fill PCFs chosen for THG. The data from melt-processed films are more significant because such films are significantly thicker. Absorption peaks that do not affect 1550 or 517 nm range in either thin or thicker films mean we can increase either thickness or dye concentration without significantly affecting target wavelength transmission. It is important to be able to do both – increase the thickness of the material and the dye concentration:

- **Dye concentration** – greater dye concentration will most likely increase nonlinear properties of the material.
- **Thickness** - ideally, the materials should allow propagation over at least several millimeters at target wavelengths (filling the fiber).

The next step after choosing the materials is to measure their nonlinear properties.

This is done by shining the high-powered femtosecond laser on the film and measuring the THG intensity. In order to perform this procedure, we need to have free standing films so that there is no interference with the glass substrate signal (it will generate its own third harmonic).

The polymer/plastisizer matrix that was used for melt-processed films does not allow for the fabrication of sturdy free standing films. A different matrix consisting of 70 wt% polystyrene-methylmethacrylate (MMA) and 30% ethyl carbazole (ECZ) have been used to manufacture free-standing films with the dyes chosen. It was experimentaly found that polystyrene could make good free standing films, however, it melts at 280°C, a temperature that would most likely destroy the dyes. Therefore we used ECZ (a plasticizer) in order to bring down the melting temperature. 30% ECZ concentration provided 160°C melting temperature, which is

good enough for the dyes to be stable. Figure 7 gives the transmission and other data on free standing films incorporating the three different candidate dyes. The nearly identical values suggest that the transmission at 517nm is not limited by the dye absorption, but rather by either host absorption or scattering.

Figure 7. Data table for free-standing films.

	2,5 dimethoxy-4'-nitrostilbene	silicon(IV) phthalocyanine	4-4'-dimethoxy-2-2'-bipyridine
Composition	dye 3 wt% PMMA 68 wt % ECZ 39 wt %	dye 1 wt % PMMA 69.3 wt% ECZ 29.7 wt%	dye 3 wt % PMMA 68 wt% ECZ 29 wt%
thickness μm	77.12	69.2	79.2
melting T °C	160	160	160
%T (1550 nm)	88.34	90.67	86.51
%T(517 nm)	82.45	80.55	80.56
Absorption peaks	1675	1677, 634	1675

Conclusions

We have done initial characterization of commercially available PCF and that of various materials that could be used to fill that fiber in order to get efficient THG.

Two fiber types have been chosen that seem to have the best chance for filling with non-linear polymer materials. The initial characterization of the fiber has been done in terms of taking images of the cross-section and sending light of two different wavelengths through that fiber.

Three dyes have been chosen that satisfy the initial conditions for being incorporated in the fiber structure:

1. 2,5-dimethoxy-4'-nitrostilbene
2. 4-4'-dimethoxy-2-2'-bipyridine
3. solubilized silicon(IV) phthalocyanine

All three chosen dyes have good transmission at 1550 nm and 517 nm wavelengths, as well as the possibility to give moderately high ^{3} values. With more time for this project, more materials could have been screened initially and more dyes would have been found to be used in the fiber.

Free-standing films have been manufactured with the chosen dyes in a polystyrene MMA/ECZ polymer host. These films now can be used with the femtosecond laser system in order to measure $^{(3)}$ values. With known $^{(3)}$ values it will be clear which dyes can generate the most efficient third harmonic. Both the refractive indices at the target wavelengths and $^{(3)}$ are needed to allow calculation of fiber structure which will allow for phase matching of fundamental and THG beams within the fiber.

Further challenges of the project are:

- to measure $^{(3)}$ values of the free standing films made with the dyes chosen
- to establish a process to fill the holey fibers chosen
- to find a way to estimate the effective index of the fibers chosen
- to measure refractive indices of chosen materials at 517 nm
- to phasematch fundamental and THG beams within the fiber

Acknowledgments

Funds for this research were provided by the Center on Materials and Devices for Information Technology Research (CMDITR), and the NSF Science and Technology Center No. DMR 0120967.

We thank J.Thomas for help with materials, Yevgeniy A. Merzlyak and Emre I. Araci for help with fiber measurements, Elena Temyanko for help with material measurements and Semra Bekele for help with lab equipment.

Katia Shtyrkova.

I am pursuing my BS in Optical engineering at the University of Arizona, where I plan to go to graduate school to get Ph.D. in Optical Engineering and later work for the industry.

Nanophotonics: Printing Nanoparticles to Create New Diffraction Gratings

Stephanie H. Tolbert, Department of Chemistry/Biochemistry, Georgia Institute of Technology

Alex Veneman, R. Clayton Shallcross, Gulraj Chawla, Neal R. Armstrong, Department of Chemistry, University of Arizona

Introduction

Diffraction gratings function as multiple slit arrangements in which constructive and destructive interference separate white light into its various colors according to wavelength, incident angle, and transmitted angle:

$$m\lambda = d(\sin\alpha \pm \sin\beta)$$

where m is the order of the diffracted beam, λ is the wavelength, d is the distance between the scattering centers, α is the angle of incidence, and β is the angle of diffraction. When the angle of incidence, , is reduced to 0º, the above equation is condensed to the Bragg's equation:

$$m\lambda = d\sin\theta$$

The diffraction efficiency of any dispersive element is strongly dependent upon both the real and imaginary components of the refractive index, as shown below by Fayer[1]:

$$DE_{(\lambda)} = e^{\frac{-2.303OD(\lambda)}{\cos\theta}}\left[\frac{T}{\lambda\cos\theta}\right]\left[\Delta k_{(\lambda)}{}^2 + \Delta n_{(\lambda)}{}^2\right]$$

Diffraction efficiency ultimately depends on the changes in the imaginary component, k, of refractive index (related to absorbance changes) and the real component, n (related to the dielectric properties of the grating material). To provide the greatest diffraction efficiency (DE), materials with high dielectric constants, absorptivity, and in turn refractive index relative to the surrounding medium are predicted to give the best performance. Master gratings are difficult and costly to manufacture, however, so an easy and cheap method for fabrication would be ideal.

Different grating fabrication procedures have been presented in recent literature, namely in the use of patterned, electrochemically grown PANI, PSS, and PEDOT conducting polymer films to create chemical and electrochemical sensing technologies[2,3]. Other researchers have made use of chemically responsive materials such as antibodies, enzymes, or nanoparticles in which the DE is highly sensitive to analyte concentration[4-7].

Cadmium selenide nanoparticles (CdSe NPs) have attracted broad attention from researchers because of their semiconducting capabilities and high refractive index and, if they can be patterned, appear to be ideal for use in diffraction-based sensing technologies. Since their refractive index is much larger than that of air, gratings composed of such a material will have enhanced diffraction efficiency (DE). In addition, these materials are highly tunable, for the wavelength of fluorescence can be controlled by the size of nanoparticles used.

Experiments conducted this summer have sought to utilize micro-contact printing to deposit patterned CdSe nanoparticles onto an optically transparent substrate, providing an easy method for grating fabrication. The photoluminescence of the CdSe gratings was also characterized to determine whether the fluorescence of these nanoparticles would appear at distinct angles relative to the excitation source. Ultimately we wish to use CdSe gratings as coupling elements for waveguide technologies and organic light emitting diodes (OLEDs). Initially, patterning on the sub-micron length scale had to be demonstrated, and this has been the primary focus over the last ten weeks.

Experimental

Patterned CdSe Grating Formation

Using soft lithography techniques, CdSe nanoparticles were deposited onto an optically transparent glass substrate using general micro-contact printing procedures. Atomic Force Microscopy (AFM) was utilized throughout the stamping process to characterize the integrity of the grating fabrication. Initially, a polydimethylsiloxane (PDMS) replica stamp of an 1800 grooves/mm blazed aluminum master grating (Edmund Optics) was prepared by pumping the PDMS solution (Dow Corning Silicone Elastomer Kit #184) into a small Petri dish containing the master grating. The silicone solution was allowed to de-gas for one hour and then harden in an oven at ~110º for 2 hours.

Once hardened, the PDMS was carefully separated from the master grating and cut to the shape of the grating with a razor blade. AFM imaging detailed a grating groove depth of ~112 nm. CdSe grating formation was continued by drop-casting CdSe NPs (50µL, 0.10 wt% in toluene) on the PDMS replica and allowing the toluene to evaporate. AFM was again used to view the alignment of the NPs on the replica stamp. Finally, the PDMS stamp containing the NPs was stamped onto a plasma cleaned microslide for one minute in a clean room using a simple stamping apparatus. Again, AFM imaging detailed the CdSe imprint of the master grating on the microslide as well as the PDMS replica post-stamping, confirming that the grating was in fact fabricated and that most of the NPs were transferred to the slide (Figure I).

Optical Characterization

The photoluminescence of the CdSe NPs was characterized with a simple diffractometer. Setup consisted of an incident transmission source (Ar^+ laser, 488 nm) fitted with a transmission filter to ensure that only light of wavelength 488 nm reached the detector, focusing lens to focus the laser on the detector, and two notch filters to decrease the intensity of laser light (Figure II). The detector, focusing lens, and notch filters were rotated about the sample in two degree increments from the angle of incidence to measure the diffraction of the laser as well as the fluorescence of the NPs.

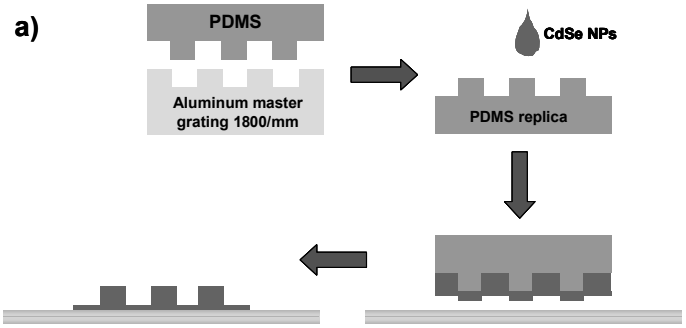

Figure 1. Micro-contact printing process characterized by AFM (a) stamping process (b) AFM of PDMS replica (c) AFM of PDMS containing NPs (d) AFM of microslide containing NPs (e) AFM of PDMS after stamping

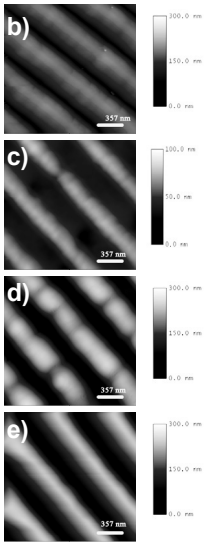

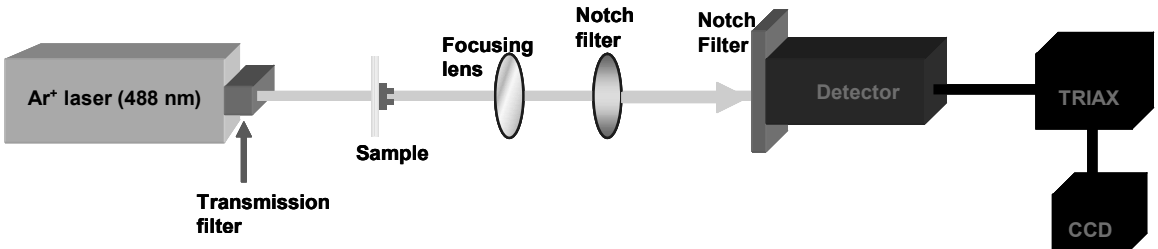

Figure 2. Schematic Diagram of optical apparatus

Results and Discussion

Evaluation of CDSe Grating Formation with Micro-Contact Printing

Micro-contact printing of CdSe NPs provided a reliable method for grating fabrication. Initially, various concentrations (0.04 – 0.10 wt %) and volumes (30 – 50μL) of CdSe NPs stamped were investigated to ensure the best application. From these trials, 0.10 wt% and 50μL were found to be the best concentration and volume, respectively. By performing AFM of the entire stamping process, it was conclusively shown that CdSe NPs were easily aligned on an 1800 groove/mm PDMS replica stamp and then transferred to a glass substrate (Figure 1).

Optical Characterization of CdSe Diffraction Grating

Applying Bragg's Law (equation 2) to the CdSe grating, the incident laser beam should be diffracted into the m = -1,+1 orders at ~50º from incidence while the NPs should fluoresce at ~73º from incidence at ~610 nm. Experimental results confirmed that the laser does diffract into its respective orders at -40º and 60º. Distortion, however, was seen in the diffraction from -60º to the angle of incidence and is more than likely due to the optical setup. When focusing the laser light on the detector, the focusing lens was not perpendicular to the incident beam. Due to this imbalance, the background radiation was slightly higher in the aforementioned region and the detector was overloaded (Figure 3b).

Placing an iris in front of the second notch filter to further hinder the amount of laser light reaching the detector would be a viable solution to this problem.

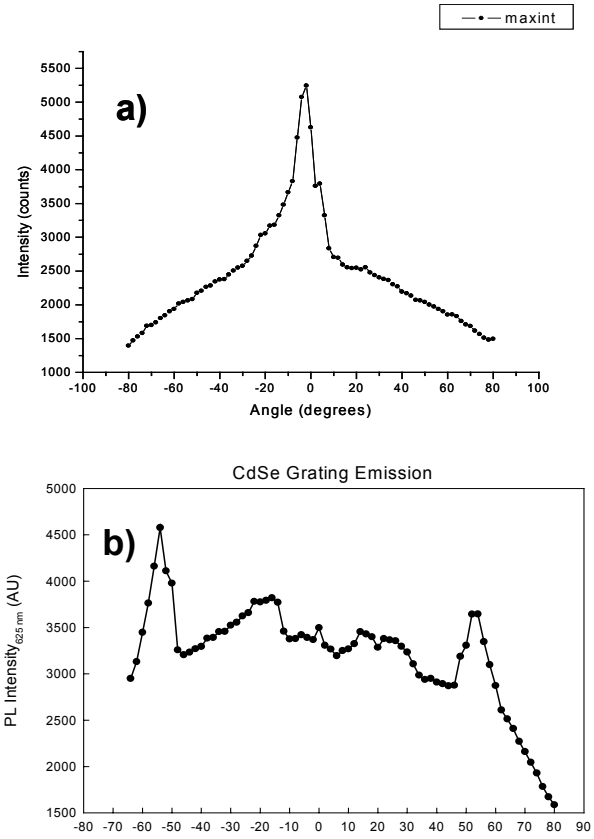

Figure 4. CdSe Fluorescence Data (a) present experimental findings, detailing featureless background fluorescence with no expected spikes of intensity (b) past research showing noticeable diffracted fluorescence at the expected angles of diffraction using 1200/mm grating

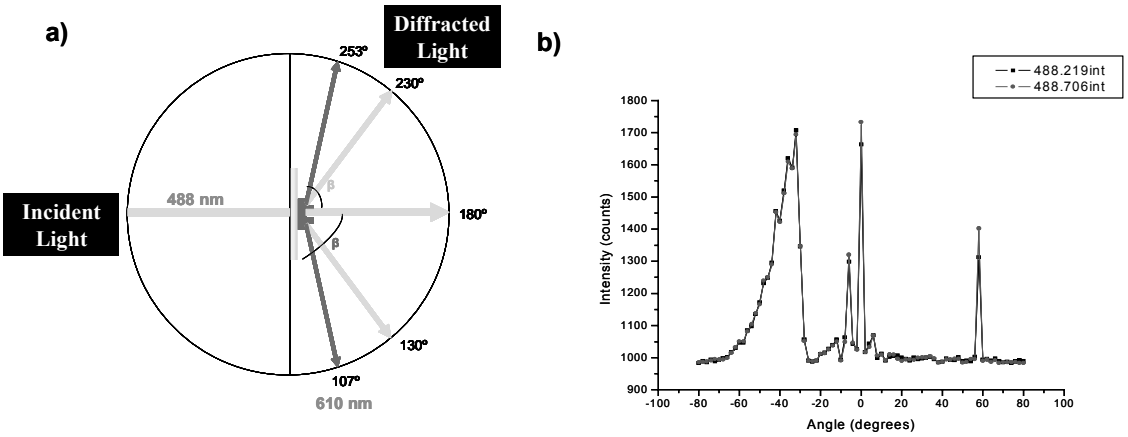

Figure 3. Diffraction of incident laser light into the m=-1,+1 orders (a) theoretical diffraction and fluorescence according to Bragg's Law (b) Ar^+ laser intensity vs. Angle

In the case of the CdSe NPs, the results were surprising. Fluorescence did in fact occur at ~610 nm, but a featureless background of fluorescence was seen at all angles and no spikes of intensity at the expected angles of diffraction. Past research has shown that constructive interference is greatest at the predicted angle of diffraction using master gratings with a lower groove frequency (Figure 5).

The present findings could be attributed to the age of the NPs used, for the chemical makeup may have altered since they were originally synthesized. Another explanation could stem from the density of NPs contained on the PDMS stamps and in turn on the microslide. AFM images of the PDMS containing the NPs show that a marked amount of NPs were drop-cast and could serve to self-quench any fluorescence that might have occurred (Figure Id). More than likely, the light was diffracted into attenuated total reflection (ATR) modes within the glass substrate (Figure VI). If this is the case, then an exciting breakthrough has been achieved. Past research has shown that a small percentage of light from an OLED source is actually internally reflected within a glass/ITO substrate because only a small fraction of angles satisfy the critical angle for total internal reflection according to Snell's Law. Placing a grating composed of nanoparticles underneath an OLED will provide a means for coupling in a larger fraction of angles. In addition, CdSe NPs absorb most of the emitted OLED light and fluoresce at an angle that is still internally reflected within the substrate. By re-emitting the OLED radiation into a narrow emission band and providing a means for the OLED light source to fit within the absorbance profile of the absorbing species, NP diffraction gratings provide promising applications towards self-contained ATR spectrometry.

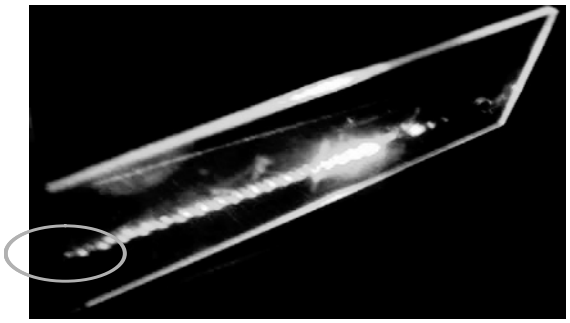

Figure 6. ATR modes of incident beam and NP fluorescence

Conclusions

The pattern of aligned CdSe nanoparticles in the shape of an 1800/mm master aluminum grating was cheaply and easily transferred onto a glass substrate with micro-contact printing. Since the semiconducting properties of CdSe are well known, micro-contact printing of such a substance provides a simpler alternative to electrochemical growth of patterned conducting polymer films. Finally, diffracted fluorescence of the nanoparticles was seen in the form of internal total reflection, providing exciting applications towards coupling of the fluorescence with OLEDs into ATR modes.

References

1. Fayer, M.D. Dynamics of Molecules in Condensed Phases: Picosecond Holographic Grating Experiments. *Ann. Rev. Phys. Chem*. **1982**, 33, 63-87

2. Tian, Shengjun; Armstrong, Neal R.; Knoll, Wolfgang. Electrochemically Tunable Surface-Plasmon-Enhanced Diffraction Gratings and Their (Bio-)sensing Applications. *Langmuir.* **2005**, *21,* 4656-4660

3. Marrikar, Saneeha F.; Carter, Chet; Robertson, Joey; Williamson, Cathie; Simmonds, Adam; Zangmeister, Rebecca; Torsteo, Fritz; Armstrong, Neal R. Conducting polymer diffraction gratings on gold surfaces created by micro-contact printing and electropolymerization at sub-micron length scales. Manuscript in progression

4. St John, P. M.; Davis, R.; Cady, N.; Czajka, J.; Batt, C. A.; Craighead, H. G. Diffraction-based cell detection using a microcontact printed antibody grating *Analytical Chemistry* **1998,** 70, (6), 1108-1111.

5. Loo, R. W.; Tam, P. L.; Goh, J. B.; Goh, M. C. An enzyme-amplified diffraction-based immunoassay *Analytical Biochemistry* **2005,** 337, (2), 338-342.

6. Bailey, R. C.; Nam, J. M.; Mirkin, C. A.; Hupp, J. T. Real-time multicolor DNA detection with chemoresponsive diffraction gratings and nanoparticle probes *Journal of the American Chemical Society* **2003,** 125, (44), 13541-13547.

7. Adleman, J. R.; Eggert, H. A.; Buse, K.; Psaltis, D. Holographic grating formation in a colloidal suspension of silver nanoparticles *Optics Letters* **2006,** 31, (4), 447-449.

Acknowledgements

I would like to thank the Neal R. Armstrong Research Group, particularly Neal Armstrong, Alex Veneman, R. Clayton Shallcross, and Gulraj Chawla at The University of Arizona. This work was made possible by the NSF sponsored Science and Technology Center on Materials and Devices for Information Technology Research, No. DMR-0120967.

Personal Statement

Stephanie Tolbert is currently working on her Bachelor's degree on Chemistry at the Georgia Institute for Technology in Atlanta, GA. She is planning on pursuing a PhD in either synthetic organic or analytical chemistry with the ultimate goal of working in cosmetics designing black hair care and beauty products.

Single-Molecule Microscopy Studies of Chromophore-Polymer Composite Materials at High Loading Density

Kurt D. Truong, University of Washington

Dan R.B. Sluss, Phillip J. Reid, University of Washington

Introduction

There is a growing interest in using organic molecules doped into polymer films in novel electro-optic (EO) materials that have a wide variety of telecommunications applications.[1] To establish bulk EO activity, the molecules in the polymer need to be aligned through a process commonly referred to as "poling."[2] The poling process involves heating the polymer host above its glass-transition temperature so that the molecules are free to rotate; then applying an external electric field across the material. EO molecules generally possess substantial dipole moments, and the molecular dipole moment interacts with the electric field causing the molecules to align with the field. In the final poling step, the polymer is cooled below the glass transition temperature to "lock-in" the molecular orientation created by the poling field.

In the dilute chromophore limit (the molecules which are so far apart they do not interact with one another); EO activity is linearly proportional to the number density of chromophores in the material. However, experimental EO activity reaches maxima at a certain chromophore number density and then decreases at greater number density.[2] This behavior is due to intermolecular forces that provide a potential of interaction that is greater than that caused by the poling field. As the molecules are pact closer together dipole-dipole interactions begin to dominate the poling field. We are interested in studying the molecular details of the poling process. One way to investigate this process is to use polarization sensitive, single molecule fluorescence microscopy to study molecular motions by correlating single molecule fluorescence anisotropy to rotational dynamics.[3]

Single molecule microscopy generally operates in the domain of low concentration to spatially resolve the molecules, but useful EO devices are made in the high loading limit. Therefore we are interested in extending the single molecule microscopy to the high-loading regime by using a non-fluorescent "background" molecule added to a polymer host at a high number density. In this approach, a fluorescent "reporter" molecule is doped into the system at single molecule concentrations. If the background and reporter molecules have similar properties, then the rotational dynamics of the single molecule reporter should be a good indicator of the rotational dynamics in the high loading limit.

Results and Discussion

The first phase of the project was the determination of a suitable background/reporter molecular pairs. A preliminary list of dyes was obtained from a paper by Peter Gunter[4], various dye catalogs[5,6], and by consulting colleagues. Since the dipole moment is an important molecular parameter, the dipole moments of the possible dopant chromophores were calculated using *ab initio* techniques (PC Spartan Pro, Wavefunction, Inc.). The absorption spectra of the potential dopants were experimentally determined to verify that the reporter molecules would have minimum absorbance at the excitation wavelengths employed. Along with recording the spectra, the absorption data was also used to determine the molar extinction coefficient using Beer's law. Fluorescence spectra were recorded using a Fluoromax-2 fluorometer. The fluorescence spectra were evaluated to find a possible background molecule that did not fluoresce in the same spectral region as the reporter molecule.

Of the molecular pairs studied, three pairs were picked for further exploration. The first possible dopant / reporter pair was pNA (4-nitroaniline) as the background molecule and

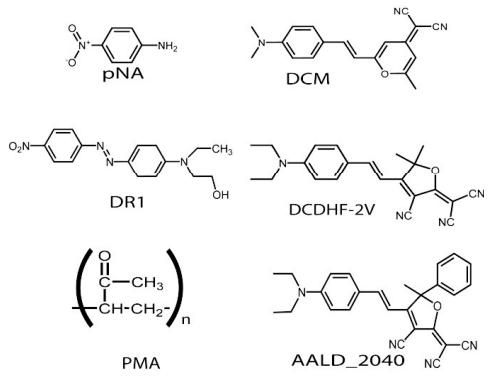

Figure 1. The chemical structures of the chemical species used in this study.

DCM (4-dicyanomethylene-2-methyl-6-p-dimethylaminostyryl-4H-pyran) as the reporter molecule with 532-nm excitation. Two other potential pairs that would work with 633 nm excitation were DR1 / AALD 2040 (2-{3-Cyano-4-[2-(4-diethylamino-phenyl)-vinyl]-5-phenyl-5-trifluoromethyl-5H-furan-2-ylidene}-malononitrile) and DR1 / DCDHF-2V.[7]

pNA / DCM was chosen for the following reasons. First, the calculated values for the dipole moments are similar (7.64 debye and 9.79 debye respectively), and both of the molecules have a similar rod-like geometry (Figure 1). The absorbance spectra shown in Figure 2 illustrates that pNA does not have an appreciable absorbance at 532 nm where as DCM does. The two molecules fluoresce when excited at 532 nm; however, pNA's fluorescence is three orders of magnitude lower and blue shifted from DCM's fluorescence. All of this information indicates that the pNA / DCM molecular system would be most effective using a 532 nm excitation source.

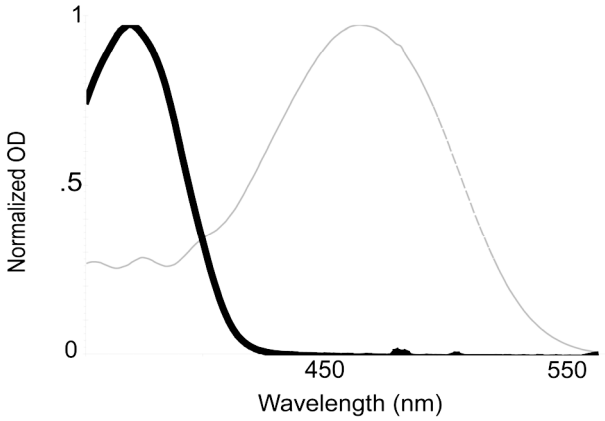

Figure 2. The normalized absorbance spectra of DCM (gray, λ_{max} = 368 nm) and pNA (black, λ_{max} = 468 nm), show little overlap.

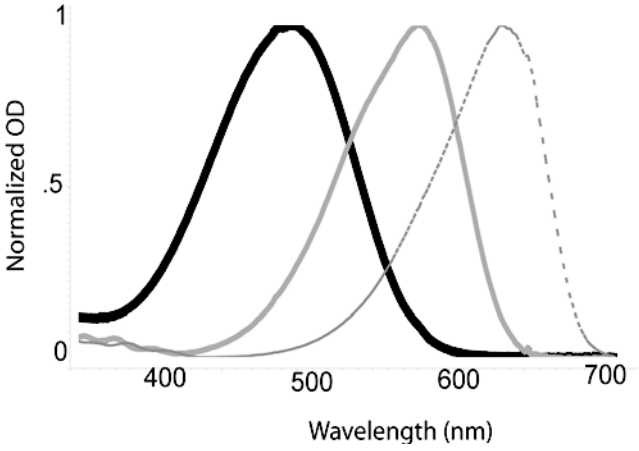

Figure 3. . The normalized absorbance spectra of DR1 (black, λ_{max} = 494 nm), DCDHF-2V (gray λ_{max} = 582 nm), and AALD_2040 (gray dotted λ_{max} = 638 nm) show little overlap between the DR1 / DCDHF-2V or DR1 / AALD_2040 background / reporter pairs.

With 633__nm excitation, two pairs of background/reporter molecules demonstrated substantial promise: DR1 for a background and either AALD 2040 or DCDHF-2V for the reporter molecule. All of these molecules possess comparable dipole moments and geometric aspect ratios (Figure 1). As was the case with the pNA / DCM system, the background molecule, DR1, does not absorb in the same spectral region as the reporter molecules, AALD 2040 and DCDHF-2V, as shown in Figure 3.

The pNA / DCM system was chosen for further study since a 532_nm excitation source was currently available for use. The reporter was doped into the polymer host at nanomolar concentration suitable for single molecule resolution, and the background molecule was doped in at 0.2 M to replicate actual EO material number density. Stock solutions were made at 8 x 10^{-5} and 1.5 M for DCM and pNA respectively by adding a known mass of material to the corresponding mass of solvent, CPN (cyclopentanone). After the stock solutions were made, DCM was diluted from 8 x 10^{-5} M to 8 x 10^{-9} M. The initial samples were made with the reporter and background molecules separate as to more easily find experimental settings. The single molecule DCM sample was prepared by spin coating a solution made of 25 μL of 8 x 10^{-9} M DCM solution,

25 μL of CPN, and to 150 μL of 20 wt% PMA (poly(methyl acrylate)) in CPN on a glass coverslip. The pNA sample was made in the same manner. The final samples were 10^{-9} M and 0.2 M for DCM and PNA respectively in 15 wt% PMA. All samples were held under vacuum overnight prior to use to drive off the solvent.

The samples were interrogated using an inverted scanning fluorescence confocal microscope described in detail elsewhere.[3] Photoexcitation was accomplished using the 532-nm output from a Nd:YVO_4 laser (Spectra Physics Millennia V). The laser output was converted to circular polarization using a λ/4 waveplate. Excitation powers of • 0.6 μW were employed. Images were acquired by scanning the sample with 100-nm resolution in both the *x* and *y* directions over the focal volume of the microscope. The polarization components of the fluorescence were obtained and detected using a polarizing beamsplitter and two avalanche photodiode detectors (PerkinElmer, SPCM-AQR-16). A sample scan image of single DCM molecules can be seen in Figure 4. The depolarized fluorescence from dye-doped polystyrene spheres (Molecular Probes) was measured daily allowing for normalization of the detector outputs.

As evident in Figure 4, fluorescence from single DCM molecules yielded roughly 600 counts per 100 ms with an excitation power of 0.55 μW. At the same excitation power, samples of 0.2 M pNA in PMA yield around 6000 counts per 100 ms. The background molecules fluoresce enough to completely overwhelm the reporter molecules by a factor of 10. At first, it was suspected that the samples were contaminated with a fluorescent species. After the same results were obtained with fresh samples, a 590 nm long pass filter was added to the experimental setup in hopes of spectrally resolving the DCM fluorescence from the pNA. With the extra filter, the same unusable signal to noise ratio was observed. It is speculated that these problems arise from the high concentration of pNA relative to the single molecule concentration of DCM.

In order to start interrogating the DR1 / AALD 2040 or DCDHF-2V systems, a 633-nm excitation source was needed to be incorporated into the existing experimental setup. The proper optical components were obtained and added to the microscope set up. The excitation source was calibrated and is now ready for use.

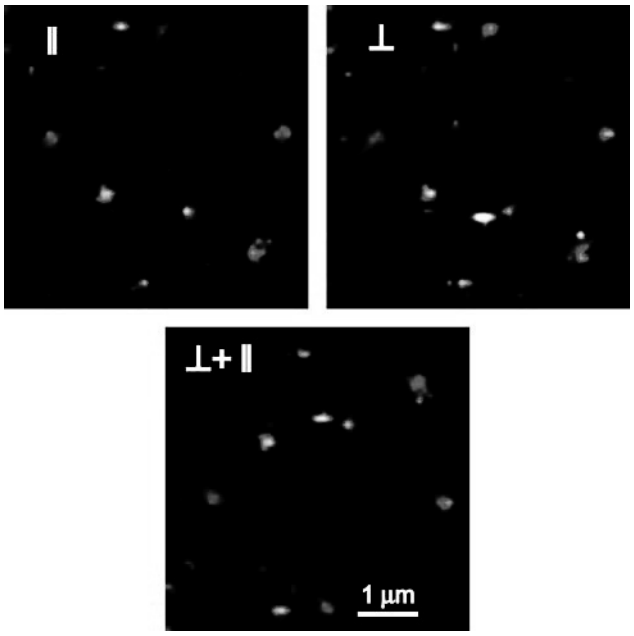

Figure 4. False-color images of the fluorescence of 10^{-9} M DCM in 15 wt% PMA. This figure represents a 5 x 5 μm^2 scan in 0.1 μm steps. The two polarization components of the fluorescence are shown above: parallel with 94-341 counts per 100 ms on the left, and perpendicular with 63-487 counts per 100 ms on the right. Below is the total intensity with 231-648 counts per 100 ms.

Conclusions

There is promise in studying the high loading density regime of chromophores / polymer composite materials by using a fluorescent reporter at single molecule concentrations in the presence of a "non-fluorescent" dopant molecule at high concentrations. Although promising at first, the pNA / DCM system does not seem like a viable system for study. A possible alternative is to study other molecular systems utilizing the newly setup 633-nm excitation source. The application of this experiment will allow fabrication of better EO devices for use in telecommunications applications.

References

1. Kimberly A. Firestone, Philip Reid, Rhys Lawson, Sei-Hum Jang, Larry R. Dalton Inorganica Chimica Acta 2004, 357, 3957-3966.

2. Robinson, B.H.; Dalton, L.R. *Journal of Physical Chemistry* **2000**, *104*, 4785-4795

3. Wallace, P.M..; Sluss, D.R.B.; Dalton, L.R.; Robinson, B.H.; Reid, P.J. *Journal of Physical Chemistry* **2006**, *110*, 75-82.

4. Gunter, Peter. Nonlinear Optical Effects and Materials. Secaucus, New Jersey: Springer, 2000.

5. Green, Floyd J. The Sigma-Aldrich Handbook of Stains, Dyes and Indicators. Milwaukee, Wisconsin: Aldrich Chemical Company, 1990.

6. Brackmann, Ulrich. Lambdachrome Laser Dyes. 2nd ed. Gottingen, Germany: Lambda Physik GmbH, 1994.

7. Willets, A.K.; Ostroverkhova, O; Meng, H; Robert, J.T.; Moerner, W.E. *Journal of the American Chemical Society* **2003,** 125**,** 1174-1175.

Acknowledgments

Funds for this research were provided by the Center on Materials and Devices for Information Technology Research (CMDITR), and the NSF Science and Technology Center No. DMR 0120967. We would like to thank Scott Hammond of the University of Washington for synthesizing the molecule DCDHF-2V.

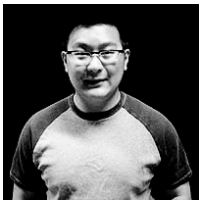

Personal Statement: The author plans on continuing his education, after earning his bachelors degree in biochemistry, by going on to graduate or professional school.

A Dithienopyrrole Derivative as a Possible Electroluminescent Material for OLEDs

Joielisa E. Tyler, Tuskegee University

Dr. Neil Cumpstey and Susan Odom, Dr. Seth Marder, Georgia Institution of Technology

Introduction

Organic Light Emitting Diodes (OLEDs) have the potential to supersede the LCD display as the technology of choice for digital cameras, cell phones, and PDAs, and even large displays such as computer monitors and televisions. OLED displays have already reached the consumer market in mp3 players, digital cameras and camcorders, cell phones and PDAs.

This paper discusses the synthesis of a new compound based on two known light-emitting compounds which are considered to have a good ECL. These compounds are 10-phenyl-3,7-bis(4-phenyl-quinolin-2-yl)-10H-phenoxazine (BPQ-PPO) and 3,7-[bis[4-phenyl-2-quinolyl]]-10-methylphenothiazine (BPQ-PTZ).

BPQ-PPO has been put into a device and has an absorption $_{max}$ of ~426 nm, its emission $_{max}$ of ~515 nm, and its electroluminescence quantum yield of

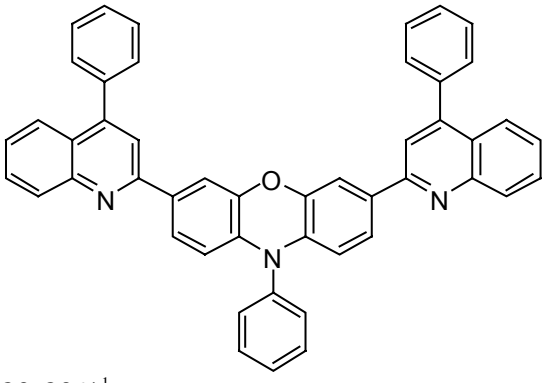

80-83%[1].

Figure 1: BPO-PPO.

BPQ-PTZ is considered a good light emitter due to its absorption $_{max}$ of ~400 nm, its emission $_{max}$ of ~540 nm, and its solid state photoluminescence efficiency of 70%[2]. There are no publications stating BPQ-PTZ has been put into an actual device.

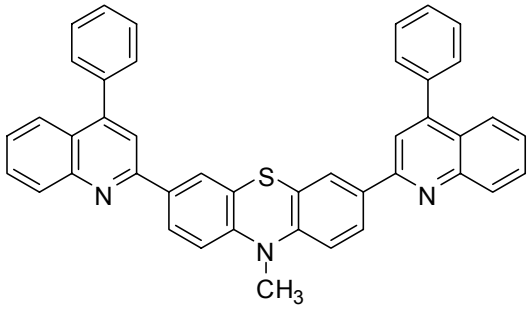

Figure 2: BPQ-PTZ

The compound that will be made is based primarily on BPQ-PTZ and is anticipated to show similar light emission properties.

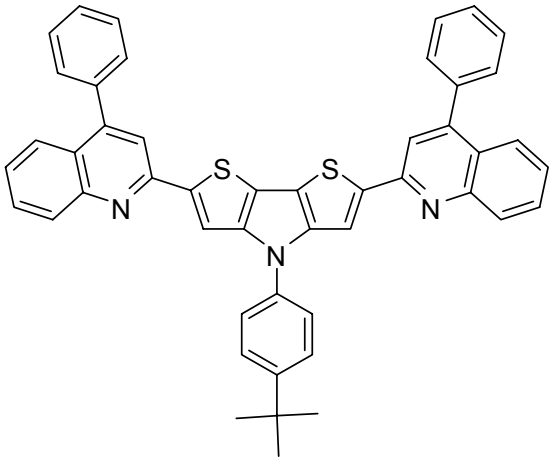

Figure 3: The desired compound is 3,7-[bis[4-phenyl-2-quinolyl]]-10-tertbutyldithienylpyrrole (BPQ-DTP)

Results and Discussion

Bithiophene was donated by Susan Odom. Bromination to the bithiophene was achieved in an 89% yield using bromine in a mixture of chloroform and acetic acid. Monitoring the reaction by GCMS, it was later found to be more accurate to monitor by ^{1}H NMR because the GCMS showed the reaction was at completion while the ^{1}H NMR showed traces of di and tri substituted dithiophene.

Debromination of the tetra-bromobithiophene by heating with zinc in a mixture of acetic acid and isopropanol gave the dibromo material in a 55% yield after recrystallization. Again, the reaction was monitored by GCMS and ^{1}H NMR. In the recrystallization, crystals had to be collected over a span of 5 days, and after each collection, more solvent was removed.

The palladium-catalyzed ring-closing anilation gave the dithieno-pyrrole in a 49% yield.

The subsequent Friedel-Crafts acetylation was carried out using acetyl chloride and aluminum chloride in carbon disulfide. When column chroma-tography was done during the synthesis of N-(4-*tert*-butylphenyl)-3,7-diacetyl-pyrrole, the desired disubstituted material was isolated. Also isolated was a material which showed the aromatic region of the ^{1}H NMR consistent with being the monoacetylated product, but the GCMS is consistent with the disubstituted product. It remains unidentified.

The duration of the program did not permit for the actual reaction to attach the 2 2-phenylquinoline groups, so the final compound that was synthesized was N-(4-*tert*-butylphenyl)-3,7-diacetylpyrrole.

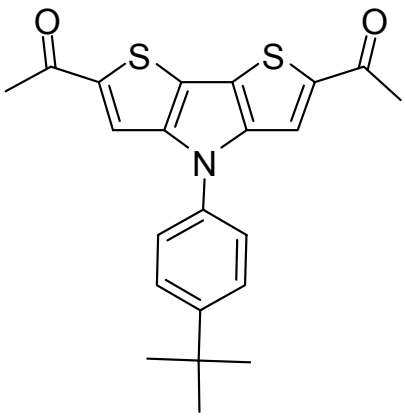

Figure 4: N-(4-*tert*-butylphenyl)-3,7-diacetylpyrrole

This compound was identified through ^{1}H NMR and mass spec. The yield was 36% while the reported literature yields on the methylphenothiazne were ~30%.

Conclusions

Four of the five reactions in scheme were accomplished, and a new compound was synthesized. The compound was N-(4-*tert*-butylphenyl)-3,7-diacetylpyrrole.

Unfortunately due to time constraints, the desired compound, BPQ-DTP, has not yet been reached. It is intended that the synthesis be continued and that the compound be characterized and its optical and electronic properties be investigated with a view to its possible use in an OLED.

Experimental

3,5-dibromo-2-(3,5-dibromothio-phenyl)thiophene 20 g (120 mmol) of dithiophene was combined with 400 mL acetic acid and 800 mL chloroform, and cooled to a temperature of 2 °C. At 2 °C, a solution of 200 mL chloroform and 36 mL (700 mmol) was added drop wise with stirring. Once all of the bromine solution was added, the reaction mixture was slowly warmed to room temperature while stirring. It was monitored by ^{1}H NMR to determine when the reaction was at completion. 2 L of dichloromethane was added. The solution was washed with 2 x 2 L water, 2 x 1 L aqueous sodium bicarbonate, and 2 x 2 L aqueous sodium thiosulfate. The organic layer was dried over anhydrous magnesium sulfate and the solvent was removed to leave a pale brown solid (57.2 g, 89%). ^{1}H NMR was in agreement with that previously measured within the group[3].

3-bromo-2-(3-bromothio-phenyl)thiophene 17.3 g (35.9 mmol) of 3,5-dibromo-2-(3,5-dibromothio-phenyl)thiophene was combined with 400 mL isopropanol, 20 mL acetic acid, and 14 g (210 mmol) zinc dust. This solution was heated to reflux and stirred overnight. The reaction was cooled to room temperature, and filtered using a Buchner funnel to remove the

zinc, and then the solvent was removed. 1.5 L of dichloromethane was added to the residue, and the resulting solution was washed 2 x 1 L aqueous sodium bicarbonate and 2 x 1 L water each. The organic layer was dried over magnesium sulfate and the solvent was removed. The crude product was passed through a silica plug using 1:1 dichloromethane: hexanes and then recrystallized from 1:4 dichloromethane: ethyl acetate to give a large yellow crystal (6.31 g, 55%). ^{1}H NMR was in agreement with that previously measured within the group[3].

N-(4-*tert*-butylphenyl)pyrrole 0.56 g (0.61 mmol) of tris (dibenzyl-ideneacetone) dipalladium, 4 mL (1.0 mmol) of tributyl phosphine 10% in hexanes, and 32 mL of toluene were combined under nitrogen. 2.0g (6.0 mmol) of 3-bromo-2-(3-bromothio-phenyl)thiophene, 1.0g (6.7mmol) *p-tert*-butylaniline, and 1.32g (13.0 mmol) sodium tert-butoxide were added to the toluene solution. The solution was heated to reflux for ~5 hours under nitrogen. The reaction was monitored by TLC to determine when it was at completion. When completed, the solvent was removed and 250 mL dichloromethane was added to the residue. The resulting solution was washed with 2 x 400 mL of water. The solvent was removed from the organic layer. The crude product was passed through a plug of silica using 1% ethyl acetate in hexanes as the solvent, then purified by column chromatography over silica in the same solvent to give a orange solid (0.933 g, 49%). ^{1}H NMR was in agreement with that previously measured within the group[3].

N-(4-*tert*-butylphenyl)-3,7-diacety-lpyrrole 0.1 g (0.3 mmol) N-(4-*tert*-butylphenyl)pyrrole , 2 mL carbon disulfide, and 0.09 g (1.0 mmol) acetyl chloride were combined. 0.48 g (3.6 mmol) aluminum chloride was added to the solution in small portions. The reaction was heated to reflux for 15.5 hours, and monitored by TLC. Ice cold, dilute hydrochloric water was added to the reaction mixture until no further yellow precipitate formed. The precipitate was filtered using a Buchner funnel. It was dissolved in a 1:1 solution of dichloromethane: hexanes and passed through a plug of silica using the same solvent. This recovered 0.056g of starting dithienpyrrole. The plug was then rinsed with 1:1 dichloromethane: ethyl acetate, the resulting material was purified by column chromatography using 4:1 ethyl acetate: hexanes as the eluent, to give a yellow solid. (0.036g, 36%) H (300 MHz, CD_2Cl_2) 1.43 (9H, s, ^{t}Bu), 2.59 (6H, s, $COCH_3$), 7.55 & 7.65 (4H, AA•BB•, Ph), 7.77 (2H, s, thiophene); m/z (GCMS) 395 (M^+, 100%).

References

1.Zhu, Kulkarni, Jenekhe, *Chem. Mater*., 2005**, 17**, 5225-5227

2.Lai, Fabrizio, Samson, Jenekhe, Bard, *J. Am. Chem. Soc.* 2001**, 123**, 9112-9118

3.Susan Odom, unpublished material

Acknowledgments

Funds for this research were provided by the Center on Materials and Devices for Information Technology Research (CMDITR), and the NSF Science and Technology Center No. DMR 0120967.

As you climb. Always reach back.

The Theoretical Study of the Magnetic Properties of Oligothiophenes

LaTonya Waller, Norfolk State University
700 Park Ave. Norfolk, VA 23504

Dr. Suely Black, Dr. Demetrio Filho and Dr. Jean-Luc Bredas, Norfolk State University and Georgia Institute of Technology

Introduction

Efforts to manufacture cheaper, faster and smaller cell phones; digital cameras and other electronics have been hampered by the performance of materials in today's semiconductor devices, traditionally based on inorganic materials. The world of modern electronics and optoelectronics is built around semiconductor materials with countless applications in telecommunications, information technology, entertainment and medical equipment, just to name a few. However, Inorganic materials are not easily modified and are somewhat expensive to fabricate. Organic compounds, on the other hand, can easily be tailored to display the desired properties, and are cost effective. These organic compounds or conjugated polymers have attracted broad interest over the past decade; in particular because in the doped state they represent a new class of light-weight electrically conductive materials which can be applied to new electronic and optoelectronic devices.[1]

Oligothiophenes, the systems of our investigation, are attractive materials for a variety of applications in electronic devices such as light emitting diodes (LED), field effect transistors (FET), electronic newspaper (Figure 1) and e-skin (Figure 2) and are also known for their high stability and non-linear optical properties. Whereas the polymers are obtained as highly amorphous materials, the oligomers can be synthesized as well defined compounds. Moreover, oligothiophenes provide interesting, models for understanding the structural and electronic peculiarities which control the charge transport and optical properties in polythiophenes.[2,3] Theoretical studies of oligomers facilitate the knowledge of polymeric structure.

Figure1.

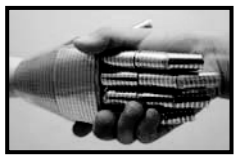

Figure2.

Figures 1 and **2.** DynaSheet by Toshiba is an electronic newspaper that allows readers to select the news they want delivered, gets updated every day. E-skin can sense changes in pressure and temperature and is made using organic transistors that are inexpensive and easy to produce. It might be possible to use the e-skin on human patients like burn victims who have lost their sense of touch, respectively.

Computational chemistry, the method used in this research, is the branch of theoretical chemistry whose major goals are to create efficient computer programs that calculate the properties of molecules (such as total energy, dipole moment, vibration frequencies, charge) and to apply these programs to concrete chemical objects.[4] It is also sometimes used to cover the areas of overlap between computer science and chemistry. One of the most important usages for computational chemistry is to model a molecular system prior to synthesizing the molecule in the laboratory. Computational chemistry uses model systems and since we cannot study the real system, we devise a model instead.

Density Functional theory (DFT) B3LYP functional, the first computational method used in this investigation, is very efficient, and has been used successfully to obtain optimized geometry of various molecules.[4] Molecular geometry is the molecules arrangement of atoms in space and the geometry of a molecule determines many of its physical and chemical characteristics, therefore it is very important to determine the geometry of a molecule when doing computational chemistry calculations.[4] According to Le Chatelier's Principle, the optimum geometry is the geometry that minimizes the strain on a given system. The geometry optimization here is a method of taking rough geometric approximations and making them

as exact as possible. It is a series of iterations performed on the molecule until the energy of the molecule has reached a minimum. Once geometry optimization is complete, energies, frequencies, etc. are obtained to compare with experimental data.[5]

In this research, we used Chem3D Ultra 10.0 and Jaguar 5.5 software packages. Chem3D, the graphical user interface(GUI) acts as a powerful structure-building tool which creates input structures compatible with Schrödinger's computational jobs. Moreover, Chem3D Ultra 10.0 provides convenient setup and submission of computational jobs.[6] Whether DFT calculations are done in gas phase or in solution, Jaguar can use calculated analytical gradients to optimize the molecular geometry to a minimum-energy structure or transition state.[7] Since in general after optimization, the molecules are in a stable condition and the energy is lowest.

The motivation for this study was derived from a recent report that the quinoidal form of oligothiophenes presents magnetic properties, which does not agree with the expected electronic structure of the molecule.[8] In fact, their quinoid structure may allow the existence of diradicals by the stabilization of the relevant aromatic structure. The display of magnetic properties reflects the presence of unpaired electrons and potential for semiconductor use. Unpaired electrons are charge carriers and are useful in electronic devices.

The purpose of this research is to determine the influence of the number of thiophene units in a quinoid oligothiophene on the stabilization of its magnetic form, which displays aromatic structural features, using computational chemistry. The study was performed considering two different oligothiophene structures: aromatic, Figure 3, and quinoidal oligothiophenes, Figure 4.

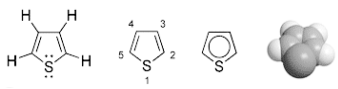

Figure 3. Aromatic thiophene

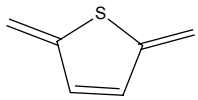

Figure 4. Quinoid thiophene $=CH_2$ terminated

The procedure consisted in obtaining the optimized geometry of the quinoidal form, both closed shell singlet and open shell triplet, and the aromatic form of the oligothiophene. Similar systems, with added cyano end groups, Figure 5, were also studied.

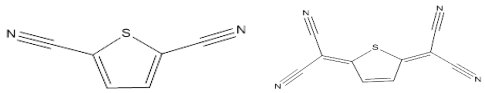

Figure5. Cyano terminated aromatic thiophene and quinoid thiophene respectively

In this study we discuss the energy differences trend, as well as the bond lengths patterns, as we add thiophene units to each of the systems, with and without added cyano end groups.

Experimental/Computational Method

The first step in this investigation was to repeat previous calculations of each system (aromatic and quinoidal singlet and triplet) using tighter conditions of convergence to compare the results with previous data and to confirm the trend in the energy differences. After those calculations were complete, we proceeded in running DFT calculations for the -CN terminated systems (aromatic, and quinoidal singlet, and triplet).

We used Chem3D Ultra 10.0 to build the thiophene monomer. After setting up an input molecular model, we use Jaguar 5.5 to do geometry optimization. Hybrid DFT functional (B3LYP/6-31G*) was used to optimize the geometry of the aromatic, quinoid singlet and quinoid triplet systems with and without –CN terminated groups, and was used to obtain the final energy of the molecule. After obtaining the optimized geometry of the monomer, we built the dimer molecule from the monomer by adding another unit on the monomer's backbone, and repeated the geometry optimization procedure. Oligomers T_3-T_{12} were submitted using the same procedure.

Results and Discussion

Oligomers T_1-T_{12} were optimized using DFT/B3LYP with 6-31G* basis set. The energies were obtained both in gas phase and solution. Running with a basis set of 6-31G*, the program computed the energy and the gradient at that point, decided if it had reached convergence, and then varied the geometry based on the size of the gradient. These steps were repeated until convergence was reached.

Analyzing the bond lengths pattern, it is possible to determine if the triplet oligothiophenes shows an aromatic or quinoid structure.

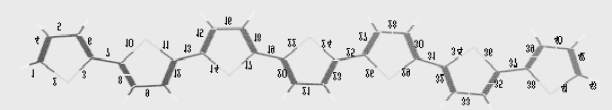

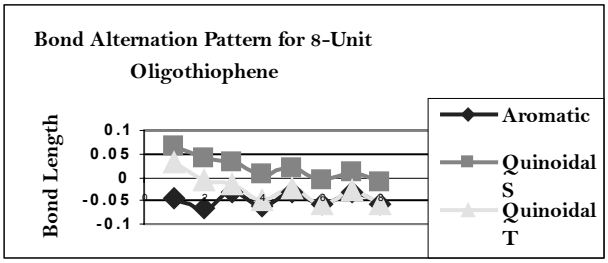

Figure 6. Bond alternation pattern for 8-unit oligothiophene.

The graph in Figure 6 above shows the bond alternation pattern for the 8-unit oligothiophenes without CN end groups. The bond alternation shows the differences in the bond size in each thiophene ring as we move to the middle of the molecule. Point 1 corresponds to b6-b5 (see picture), while point 2 corresponds to b6-b7. Further points show differences of lengths of similarly positioned bonds as we move to the center of the molecule.

With this definition, negative values correspond to aromatic structure, and positive values, to quinoidal one. We see a transition in the triplet system from a quinoidal to an aromatic structure at the second ring, and as we continue into the middle of the polymer, the quinodal triplet converges to pure aromatic form. On the other hand, the singlet's up and down pattern is less pronounced and seems to be converging at a much slower past, but never

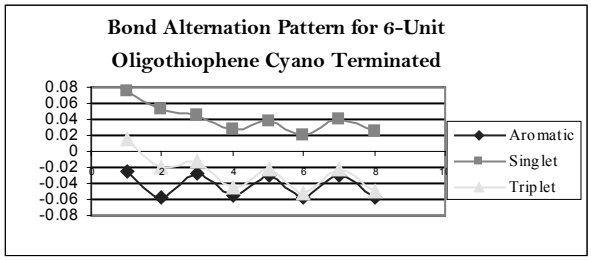

Figure 7. Bond alternation pattern for the 6-unit C-terminated oligothiohene.

The graph depicted in Figure 7 above shows the bond alternation pattern for the 6-unit C-terminated oligothiohene. The bond alternation shows the differences in the bond size with increased units. We see a transition in the triplet system from quinoidal to an aromatic structure a lot sooner than in the bond alternation chart without CN groups. The transition takes place sooner with CN groups because the CN stabilizes the unpaired electrons on the triplet system.

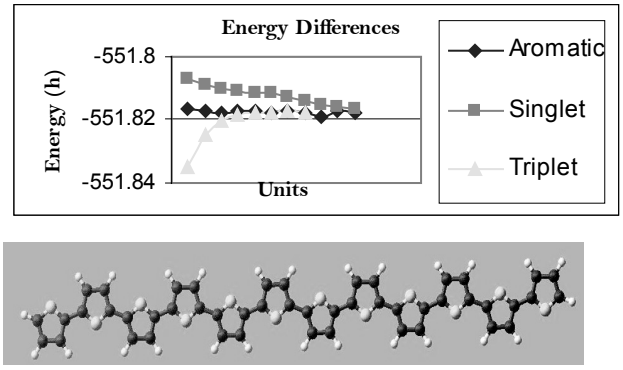

Figure 8. Energy Differences

Figure 8 shows the trends in energies differences as units are added to the polymers. The aromatic structures' energies differences show almost no change with the increase in the number of thiophene rings. For the quinoidal singlet system, there is a linear increase in the stabilization (increase energy differences) with the addition of units. For the quinoidal triplet, there is a large destabilization as new units are added up to three units, and finally, convergence to aromatic values is seen. The similarity in energy differences probably reflects the similarity in structure.

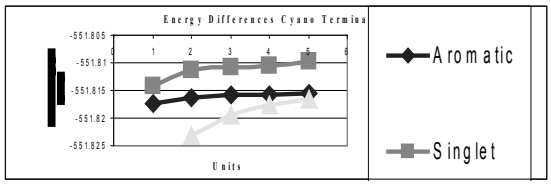

Figure 9. Trends in energy differences with increase in number of units CN terminated [Energy (n+1) – Energy(n)]

Figure 9 shows the trends in energies differences for the CN terminated polymers as units are added to the chain. The aromatic structures' energies differences show almost no change with the increase in the number of thiophene rings. For the quinoidal singlet system, there is a linear decrease in the stabilization (increase energy differences) with the addition of units and it doesn't seem to be converging to the aromatic structure at all. For the quinoidal triplet, there is a large destabilization as new units are added up to three units, and finally, convergence to aromatic values is seen. It seems as though the addition of a CN group increases the rate at which the triplet system converges to aromatic values. The similarity in energy differences probably reflects the similarity in structure.

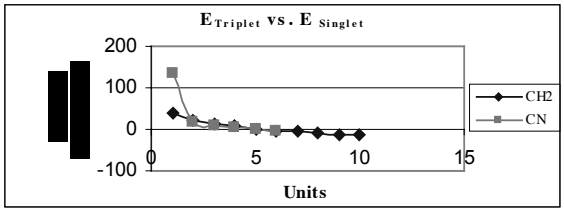

Figure10. Energy Differences

Figure 10 shows the differences in the energies between the singlet and triplet states of =CH2 terminated oligothiophenes. Positive differences correspond to structures more stable at the singlet state. This graph clearly identifies the hexamer as the shortest polymer which will be more stable in the triplet state. For the =CN terminated molecules, after the addition of one unit, the singlet and triplet state have the same value and then the triplet becomes the most stable at six units.

Conclusions

We determined the structure of the triplet state of the =CH2 terminated oligothiophenes is a hybrid of aromatic and quinoidal structures, the middle of the structure completely reproducing that of the aromatic system. For 5 repeat units and above, the triplet oligothiophene resembles the aromatic form energetically. The addition of CN groups to the end of the polymer increases the rate at which the triplet converges to an aromatic structure due to the CN group's stabilizing effect on the unpaired electrons. At six units of chain length, the =CH2 and -CN terminated quinoidal oligothiophene become more stable in the triplet state, according to our B3LYP 6-31G* calculations.

References

1. Low-Bandgap Conjugated Polymers. A joint Experimental and Theoretical Study of the Structure of Poltisothianaphthene. By I. Hoogmartens, P. Adriansens, D. Vanderzande, and J. Gelan C. Quattrocchi, R. Lazzaroni, and J.L. Bredas*

2. S. M. Bouzzine, S. Bouzakraoui, M Hamidi, M. Bouachrine, Asian J. Chem. In press.

3. J. Cornil, D. Beljonne, J. L. Bredas, in: G. W. Mullen (Ed.), Electronic Materials: The oligomer Approach, Wiley-VCH, Weinheim, NY, 1998, pp. 432-447.

4. David C. Young, Computational Chemistry: A practical guide for applying techniques to real world, John Wiley & Sons, Inc. 2001, p3.

5. http://www.schodor.org/chemviz/optimization /students/introduction.html

6. Chem3D Ultra 10.0 Copyright 1986-2006 CambridgeSoft.

7. Jaguar' User Guide, Version 4.2, Julie R. Wright, Schrödinger, Inc. p7

8. Magnetic Properties of Quinoidal Oligothiophenes: More Than Good Candidates for Ambipolar Organic Semiconductors? ** By Rocío Ponce Ortiz, Juan Casado, Víctor Hernández, Juan T. López Navarrete,* Enrique Ortí,*Pedro M. Viruela, Begoña Milián, Shu Hotta, Gianni Zotti,* Sandro Zecchin, and Barbara Vercelli.

Acknowledgments

Latonya Waller would like to acknowledge the CMR and MDITR Staff, Dr. Demetrio Filho, Dr. Suely M. Black, Dr. Jean-Luc Bredas, Ms. Jennifer West; The authors would like to acknowledge the support of grants: CMR NASA CREAM Project NCC3-1035, CMR NSF-CREST Project HRD-0317722, and CMR NSF-CMDITR Project.

My educational goals include earning a bachelor's degree in chemistry, a master's in materials science, and exploring career opportunities in these fields.

Photophysical Properties of a Non-Linear Optical Dye in Salt Crystals

Susanna M. Wong
Simmons College

Kristin L. Wustholz, Bart E. Kahr,
Philip J. Reid
University of Washington

Introduction

Electrooptic (EO) switches based on polymers doped with non-linear optic (NLO) chromophores are of particular interest because they are made with low cost materials and provide a faster switching rate compared to the technology currently available. However, at this time, the translation of molecular systems with large hyperpolarizabilities to devices with large EO activity is not completely understood. Specifically, the alignment of dyes in polymers, generated by the application of an electric poling field, is not well established. A better understanding of chromophore alignment and photophysics in dye-doped materials at the single-molecule level is required to extend the performance of polymer-based EO switches. To determine the photophysical properties of a typical NLO chromophore, crystals of potassium acid phthalate (KAP) dyed with the fluorophore 4-(dicyanomethylene)-2-methyl-6-(4-dimeth ylaminostyryl)-4*H*-pyran (DCM), were grown and studied by confocal fluorescence microscopy; where the transparent host provides an intrinsically aligned and stabilized environment. Our goal was to interrogate the role of innersystem crossing (ISC) in the photophysics of DCM molecules. Therefore, DCM was doped into isomorphous crystals[1] of rubidium acid phthalate (RAP), in order to explore the role ISC to the triplet state (T_3), enhanced by the presence of rubidium, in the emission dynamics.

By quantifying the photophysics in KAP as compared to RAP, we aim to generate an understanding of the nature of the "dark state" in DCM. The dark state refers to the "off" time in the blinking trace, corresponding to no emission. In a prototypical three level energy system, when a molecule is cycling from absorbance and fluorescence we call that the "bright state," because light is continuously emitted. We explored the hypothesis of the infrequent ISC of a molecule to the T_3 which then relaxes back down to the ground state by taking advantage of the "heavy atom effect", which is known to enhance ISC from a singlet (S_1) excited to T_3 by studying DCM doped RAP crystals. KAP and RAP are isomorphous, which is important in our study of the photophysical effects solely caused by a heavier atom.[2] We compare the energetics and photophysics of the NLO dye DCM in KAP and RAP salt crystals.

Results and Discussion

In dyed single crystals of KAP, chromophores are overgrown and oriented into specific subvolumes of the crystal during growth from solution which demonstrated stabilized alignment of molecules.[3] Crystals of potassium acid phthalate (KAP) dyed with DCM were grown by solvent evaporation at 30 ± 0.1° C in aqueous solution. To obtain heavily-dyed crystals, solutions containing 10^{-4} to 10^{-5} M DCM dissolved in ethanol were added to supersaturated KAP growth solution. Different concentrations of dye and KAP growth solutions were used to optimize crystal growth. From attempts to grow heavily dyed crystals, the results show that DCM easily crashes out of solution. We determined the best growth conditions included a supersaturated KAP growth solution, 5 x 10^{-5} M DCM in ethanol in a 250-mL dish, evaporated for 5 days with no seed in a 30°C water bath.

To dope DCM into RAP crystals, rubidium acid phthalate was made by adding stoichiometric amounts of rubidium hydroxide and phthalic acid in an aqueous acid-base reaction. Dyed RAP crystals were grown under the same conditions that worked for KAP but except in 10-mL dishes. DCM is incorporated in both the {110} and {11-1} growth sectors of RAP, as compared to just the {11-1} sector in KAP as shown in Figure 1.

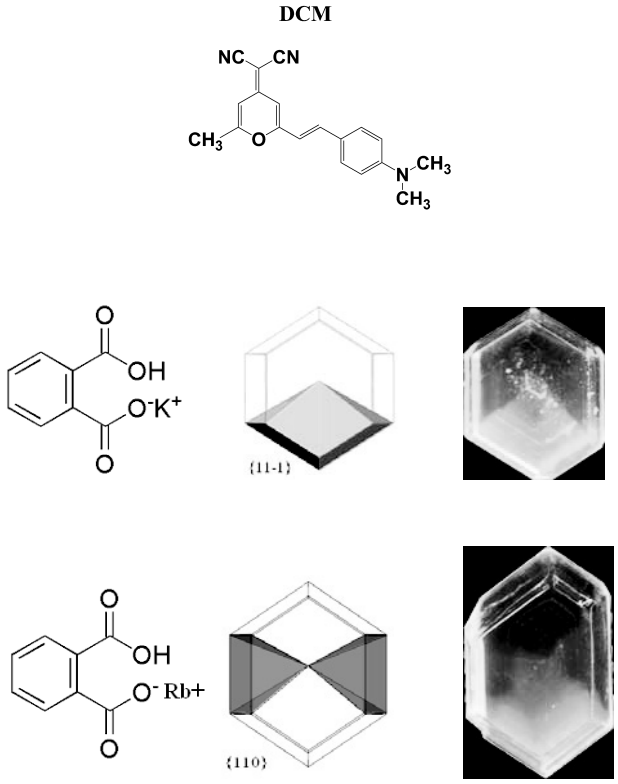

Figure 1. Dye-inclusion crystals of DCM in KAP and RAP. DCM (structure shown) is incorporated in the {11-1} growth sector of KAP and in both the {110} and {11-1} growth sectors of RAP.

Once DCM was doped into KAP and RAP, we intended to characterize the orientational and photophysical properties of this dye using several microscopy techniques. Characterization of heavily-dyed crystals was performed by absorbance and fluorescence microscopy. Average orientations ( ) for many molecules were determined by measuring the polarized absorbance and excitation along orthogonal eigenmodes. These values are then used in:

$$\theta = \tan^{-1} \cdot \sqrt{\frac{I_{//}}{I_{\perp}}} .$$

Bulk dichroism was measured on crystals of DCM dyed KAP and RAP. Figure 2 presents the polarized absorbance of DCM in KAP crystals along a- and c- direction respectively, showing absorbance at 408 nm, 433 nm, and 461 nm. The average orientations from [100] for the three peaks of DCM in KAP are 25.6 º, 25.3 º, and 29.3 º, respectively. Figure 3 shows the polarized absorbance of DCM in RAP crystals which were obtained in the same way as KAP. These absorbance spectra show structure at 404 nm, 428 nm, and 459 nm. The average orientations for the three peaks of DCM in RAP were found to be 23.4 º, 20.6 º, and 21.4 º from [100]. The absorbance spectra of DCM in KAP and RAP are nearly identical. However, the orientations of dye molecules in these two crystals are slightly different. For DCM in RAP, the absorption transition dipole moment is oriented at 21.8 ± 1.4° from [100], as compared to 26.7 ± 2.2° from [100] for DCM in KAP.

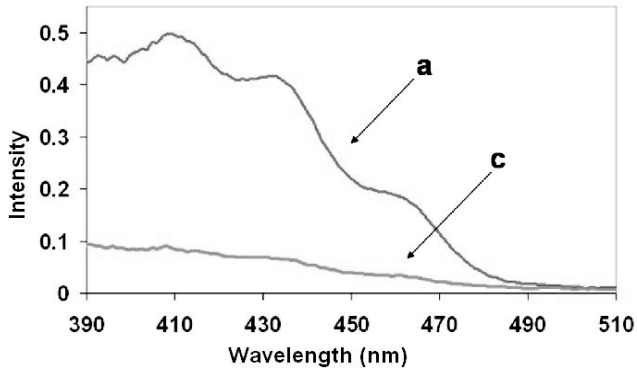

Figure 2. Polarized absorbance of DCM in KAP.

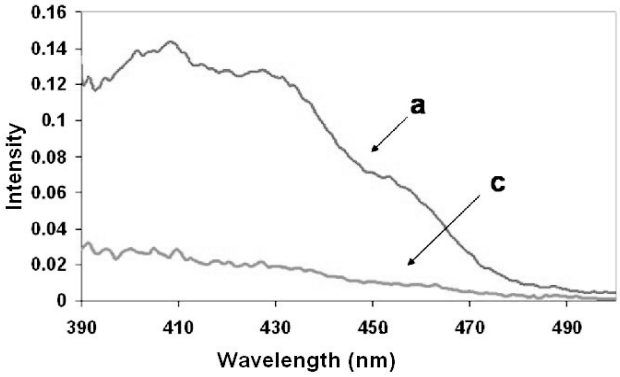

Figure 3. Polarized absorbance of DCM in RAP.

The polarized excitation spectra of DCM in KAP and RAP crystals were obtained using 430-nm excitation from a fluorimeter that was coupled to a polarizing microscope. Figure 4 presents our results. DCM in KAP emits at 481 nm, 511 nm and 543 nm, in agreement with prior measurements.[2] The average orientations for the three emission peaks of DCM in KAP are 21.7 º, 19.4 º, and 18.8 º from [100], in agreement with prior results.[2]

Figure 5 shows that by substituting a rubidium ion for a potassium ion, a fourth emission peak appears in the emission spectrum of DCM at 419 nm, in addition to structure at 460 nm, 474 nm and 493 nm. The average orientations for at

these wavelengths are 37.2 º, 35.2 º, 31.5 º, and 29.8 º from [100]. Comparison of Figures 4 and 5 show that the emission spectra of DCM in and KAP and RAP are very different; DCM in RAP is hypsochromatically shifted relative to KAP. Furthermore, the orientations of dye molecules in these two crystals are very different. For DCM in RAP, the transition dipole moment is oriented at 33.4 ± 3.4° from [100], as compared to 20.0 ± 1.5° from [100] for DCM in KAP. These results demonstrate the subtle differences imposed by the host on dye incorporation into salt crystals.

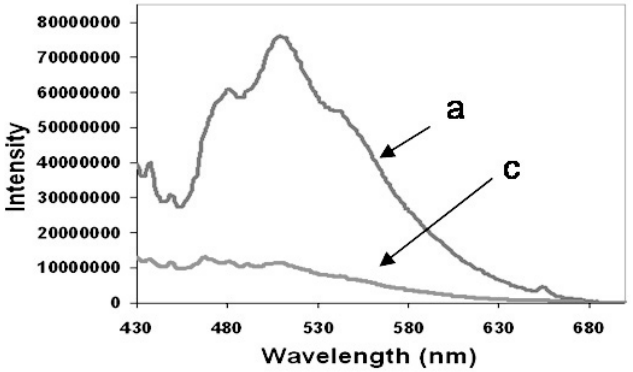

Figure 4. Polarized excitation dichroism of DCM in KAP.

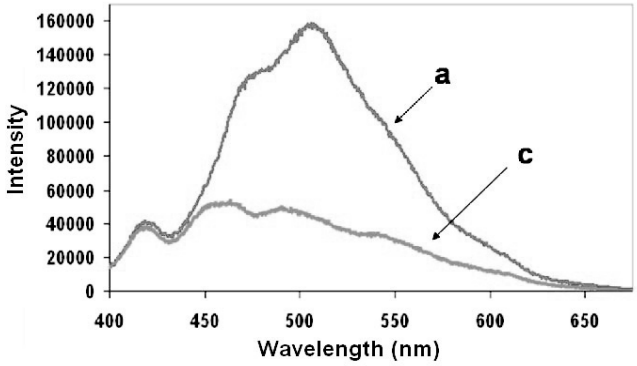

Figure 5. Polarized excitation dichroism of DCM in RAP.

Bulk absorbance and fluorescence microscopy revealed differences in the bulk spectral properties of DCM doped KAP and RAP. The absorbance spectra for DCM in these crystal hosts were nearly identical, but the absorption transition dipole moment of DCM in RAP was more closely oriented to [100]. The emission spectrum of DCM in RAP is blue shifted with respect to KAP, by approximately 30 nm. Characterizations on these heavily dyed crystals reveal that the average orientation of DCM differs in KAP as compared to RAP. Polarized absorption measurements suggest that the absorption transition dipole moment is oriented closer to [100] for DCM in KAP, however polarized excitation measurements reveal that the average orientation of DCM is approximately 10° farther from [100] in RAP than KAP. Although these results appear to contradict, we believe that the low absorbance signal from DCM dyed RAP crystals may introduce some error into this measurement. Efforts to grow more heavily-dyed crystals are underway.

While absorbance and fluorescence microscopy generates polarized spectra, our confocal microscope measures polarized excitation intensity versus distance. Confocal experiments were performed using an inverted microscope (Nikon, TE2000). Excitation from a 405-nm solid-state laser was filtered (Chroma) and the excitation polarization was manipulated using a half-waveplate. Crystal samples were mounted on a closed loop x-y piezo scanning stage (Queensgate). The laser was focused on a diffraction-limited spot with a 100 X objective (Nikon, 1.3 NA), employing an epi geometry. Emission was spectrally filtered by a dichroic mirror and emission filters (Chroma) and spatially filtered with a confocal pinhole (ThorLabs: 100 μm). The fluorescence was imaged onto a counting avalanche photodiode (PerkinElmer) and data was collected with a custom Labview (National Instruments) program.

Figure 6 shows a depiction of the DCM dyed RAP crystal that was illuminated with a 405-nm laser. The resulting fluorescence intensity maps along linearly polarized directions, [100] and [001] are shown for area 1 and 2, in Figure 6a and 6b. Images of the excitation dichroism for the two areas are shown in Figure 6c. From this data, the average orientations of DCM molecules in area #1 were determined to be 40° from [100], while an adjacent section, area #2 gave 29° from [100]. These observations suggest some environmental heterogeneity within the dye inclusion on the length scale of our measurements. These results motivate the use of single-molecule techniques to further explore this phenomenon.

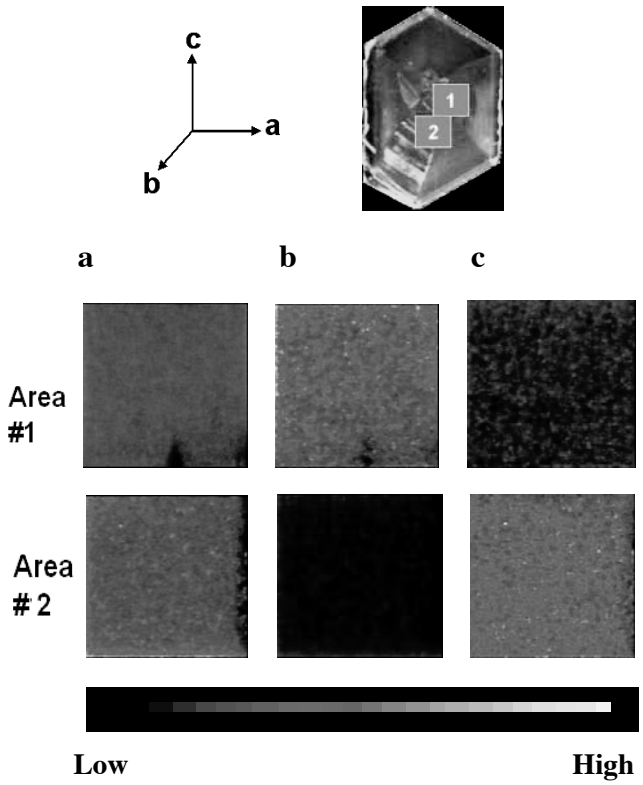

Figure 6. Polarized excitation dichroism in adjacent 20x20 μm^2 areas (labeled #1 and #2) in DCM dyed RAP.

Conclusions

In order to understand the photophysical properties of a typical NLO dye, we doped crystals with DCM measured bulk polarized spectra. DCM was successfully doped into KAP and RAP crystals. Overall, the absorbance spectra of DCM in KAP and RAP are nearly identical. The orientations the transition dipole moment, interrogated by absorbance measurements, of dye molecules in these two crystals are just slightly different. However, the emission spectra of DCM in KAP and RAP are very different. According to polarized excitation measurements following excitation at 430 nm, DCM in RAP is oriented at 33.4 ± 3.4° from [100], as compared to 20.0 ± 1.5° from [100] for DCM in KAP. Furthermore, the wavelengths in the excitation spectra of RAP are blue shifted as compared to KAP. From these bulk absorbance and fluorescence microscopy studies, several differences in the bulk spectral properties of DCM doped KAP and RAP crystals were observed.

Confocal microscopy measurements were performed to measure the fluorescence intensity maps on dyed crystals. These results showed that a wide range of orientations is observed, even in adjacent areas of the crystal. Bulk excitation measurements showed dyes in one area are oriented at 40° from [100], while an adjacent section gave 29° from [100]. These results motivate the use of single-molecule techniques to investigate chromophore alignment as it relates to crystal environment. The results presented here provide an insight to the extent to which dye inclusion into a crystal lattice results in chromophore alignment. Future work will involve measuring blinking dynamics and orientations of single molecule in KAP as compared to RAP. Comparing these crystals to identify what is responsible for the "dark state" observed in blinking. As well as doping more NLO-active dyes into crystals to study their orientational and photophysical properties.

References

1. Shi, Z.; Liang, G. *Chin. J. Infrared Res.* **1988**, *7*, 39-46
2. Wustholz, K.L.; Kahr, B.; Reid, J.P. *J. Phys. Chem. B.* **2005**, *109*, 16357-16362
3. Logan, R. World of Chemistry: The homepage of Ralph Logan 8/14/06 http://members.aol.com/profchem/unitcell.html
4. Benedict, J.B.; Wallace, P.M.; Reid, P.J.; Jang, S.-H.; Kahr, B. *Adv. Mat.* **2003**, *15*, 1068.; Barbon, A.; Bellinazzi, M; Benedict, J.B.; Brustolon, M.; Fleming, S.D.; Jang, S.-H.; Kahr, B.; Rohl, A.L. *Angew. Chem., Int. Ed. Engl.* **2004**, *43,* 5328.

Acknowledgments

Funds for this research were provided by the Center on Materials and Devices for Information Technology Research (CMDITR), and the NSF Science and Technology Center No. DMR 0120967. The authors wish to thank Jason Benedict and John Freudenthal for solving a RAP hydrate crystal structure.

Susanna Wong will complete her undergraduate study at Simmons College. In May 2007 she will receive her B.S. in chemistry. Her career plans are to go on to graduate school and to pursue a doctoral degree in chemistry.